Single-Molecule Nanoelectronic Biosensors Fabricated via Electrical Breakdown

Jasper Paul Fried

University of Oxford, St Anne's College

Department of Materials

This dissertation is presented in partial fulfillment of the requirements for the degree of DPhil in Materials Science at the University of Oxford.



Declaration

I declare that this thesis was composed by myself and that this work has not been submitted for any other degree or professional qualification. The work contained herein is my own expect where explicitly outlined below. Fabrication of the suspended SiN_x membranes was performed by Jacob Swett and James Yates. Fabrication of the electrodes for devices used in Chapter 4 and some of the devices used in Chapter 3 were performed by Jacob Swett. Fluorescence imaging of nanopores was performed by Binoy Paulose Nadappuram and Aleksandra Fedosyuk. TEM imaging of nanopores was performed by Ondrej Dyck.

Acknowledgements

I would firstly like to thank my supervisors Jan Mol and Andrew Briggs for giving me the opportunity to work in their lab and providing the facilities to perform the research presented in this thesis.

I would also like to thank all of the members of our research group over the past few years. I would like to thank Bart Limburg for all of the help he gave me early in my PhD in setting up experiments, particularly for developing code and electronics. I would like to thank James Thomas for always having my best interests within the research group at heart. I would like Xinya Bian for always being willing to help with my experiments, particular for the countless times I called him to find the source of noise in my setup. I would particularly like to thank Jake Swett for the huge amount of help he gave me during my PhD whether it be teaching me nanofabrication or having detailed discussion about my project direction. Jake always went above and beyond what can be expected of a labmate and I am sure much of the research in this thesis would not have been possible without his guidance. I would like to thank Alex Gee for the helping me with nanofabrication and always being willing to discuss science with me. I would also like to thank John Cully, Achim Harzheim, Alessandro Lodi, Charalambos Evangeli and many other over the years for making our building a more enjoyable atmosphere to work in.

I would like to thank my collaborators at Imperial College London. Particularly, I would like to thank Binoy Paulose Nadappuram and Aleksandra Fedosyuk for often prioritising my research and spending many hours imaging nanopores for my benefit. I would also like to thank Joshua Edel and Alex Ivanov for being very welcoming to accept me as a collaborator, and more recently to perform a short post-doc within their group.

I would like to thank James Yates for sharing many of his research ideas and projects with me and always being willing to help me troubleshoot problems or discuss data. I would also like to thank James and his father Rob Yates for their help in designing a fluidic cell which I used to perform many of the experiments shown in this thesis.

I would like to thank my collaborators at Oak Ridge National Laboratory. Namely, I would like to thank Ondrej Dyck for TEM imaging of nanopores. I would like to thank Daryl Briggs and Kevin Lester for helping to prepare the wafers used in this thesis. I would like to thank Ivan Kravchenko for sending many photomasks and wafers to Oxford and his help during my time in Oak Ridge. Finally I would like to thank the rest of the CNMS cleanroom staff for their assistance during my time in Oak Ridge.

I would like to thank the solid-state nanopore team at Oxford Nanopore Technologies. Particularly, I would like to thank Marion Crawford, Ken Healy, and Ping Xie for always being an email away to answer any nanopore questions I had.

I would like to thank Peter Metaxas for introducing me to the world of academia. The guidance he gave me during my Masters project held me in good stead for completing my PhD.

I would like to thank John White and the rest of the Oxford-Australia Scholarship committee for showing faith in me by selecting me for a James Fairfax scholarship to help fund my studies at Oxford.

I would like to thank all of my family and friends, in Oxford, Australia, or elsewhere for always providing me with an escape from work.

Lastly, I would like to thank my parents for all of the support they have given me over the years.

Abstract

In the past several decades, there has been significant interest in the development of nanoelectronic devices capable of detecting and characterising analytes at the single-molecule level. Applications for such devices are diverse and range from fundamental biological studies to clinical diagnostics. Unfortunately, due to the nanoscale dimensions required, the fabrication of these devices has often relied on time consuming processes that require specialised equipment. This has limited the availability of these devices to the wider research community and in turn slowed their development. This thesis focuses on the fabrication of single-molecule nanoelectronic biosensors via electrical breakdown techniques. These fabrication techniques are rapid, don't require specialised equipment, and can be fully automated. As such, they have the potential to significantly accelerate research into nanoelectronic single-molecule biosensors.

The first part of this thesis is focused on further developing the controlled breakdown (CBD) technique to fabricate nanopores. This technique relies on applying a large electric field across a thin dielectric membrane to induce breakdown and subsequent nanopore formation. Firstly, the mechanism of electrical conduction and nanopore formation during CBD is explored. It is demonstrated that, depending on the membrane stoichiometry, conduction is limited by either oxidation reactions that must occur at the electrolyte-membrane interface (Si-rich SiN_x) or charge transport across the dielectric (stoichiometric Si_3N_4). Next, these results are built upon to introduce a new CBD protocol that enables the independent fabrication of multiple nanopores in a single membrane. This technique relies on applying the breakdown voltage between an on-chip electrode and an electrolyte solution in contact with the other side of the membrane. In this CBD protocol, electrolyte is only present on one side of the membrane which ensures that previously created nanopores are not affected by each new breakdown event. Lastly, this technique

is extended to enable the integration of nanopores with on-chip nanostructures. Here, a large current density is passed through an on-chip metal nanoconstriction simultaneous to CBD. This leads to localised Joule heating at the center of the constriction which confines nanopore formation to this region.

In the second part of this thesis, a feedback controlled electroburning technique is utilised to fabricate graphene nanoelectronic devices with a view towards their use in single-molecule biosensing applications. It is demonstrated that these devices display extremely large noise amplitudes. The observed noise can be explained by a charge noise model by incorporating fluctuations in the source-drain and gate voltages. Interestingly, in some cases, this charge noise results in two-level fluctuations in the current level. The implications of the observed noise for single-molecule biosensing applications are discussed.

The results demonstrated in this thesis will hopefully provide a path towards the accessible fabrication of complex nanostructures often required for single-molecule nanoelectronic biosensing applications. The development of such fabrication techniques would significantly accelerate research in this field.

Contents

1 Introduction **1**

1.1 Motivation 1

1.2 Basics of Nanopore Sensing 3

1.3 Advanced Solid-State Nanopores 6

1.4 Fabrication of Solid-State Nanopores 11

1.5 Thesis Outline 16

2 The Basics of Controlled Breakdown **19**

2.1 Basic CBD Protocol 19

2.2 Advantages of CBD 22

2.3 Challenges of CBD 23

2.4 Advanced CBD Methods 27

2.5 Laser Assisted Controlled Breakdown 29

2.6 Electrochemical Reactions 31

2.7 Experimental Setup 33

2.8 Nanopore Fabrication and Translocation Experiments 35

3 Understanding Electrical Conduction and Nanopore Formation During Controlled Breakdown **41**

3.1 Motivation 42

3.2 Device Geometry and Experimental Setup 42

3.3 Electron Transport in Silicon Nitride 44

3.4 Redox Reactions at the Membrane-Electrolyte Interface 48

3.5 CBD with Microelectrodes on the Membrane Surface 51
3.6 Varying the Membrane Stoichiometry 56
3.7 Charge Accumulation in the Membrane 58
3.8 Conclusion and Outlook 60

4 Independent Fabrication of Multiple Nanopores via Controlled Breakdown Using On-Chip Electrodes 63

4.1 Motivation 64
4.2 On-Chip Biasing Fluidic Cell Design 65
4.3 Device Geometry and Experimental Setup 67
4.4 Independent Fabrication of Multiple Nanopores 69
4.5 Resulting Nanopore Diameters 74
4.6 Reverse Biased Configuration 75
4.7 Biomolecular Translocation 77
4.8 Conclusion and Outlook 79

5 Self-Aligning Nanopores with Complementary Nanostructures using Controlled Breakdown 81

5.1 Motivation 82
5.2 Device geometry and Experimental Setup 83
5.3 CBD Temperature Dependence 84
5.4 Electromigration of Metal Nanoconstrictions 86
5.5 Localised Breakdown via Joule Heating 89
5.6 Other Potential Device Geometries 91
5.7 Conclusion and Outlook 95

6 Noise in Graphene Nanoelectronic Devices 97

6.1 Motivation 98
6.2 Electron Transport in Nanostructures 99
6.3 Electroburning 101
6.4 Device Geometry and Measurement Setup 103

6.5 Liquid Gated Graphene Quantum Dots 105
6.6 Charge Noise in Graphene Quantum Dots 107
6.7 Random Telegraph Noise 110
6.8 Noise in Different Environments 112
6.9 Outlook For Single Molecule Biosensing Applications 113
6.10 Conclusion and Outlook 117

7 Summary **119**

A Device Fabrication **156**
A.1 Suspended SiN_x Membranes 156
A.2 Electrodes on Suspended SiN_x Membranes 157
A.3 Graphene Nanodevices 159

B Fluidic Cell Designs **161**

C Device Discharge **165**

D The Simmons Model **167**

E Rate Equation Model for Electron Transport **168**

Chapter 1

Introduction

1.1 Motivation

Biomolecular sensors, or biosensors, are devices that are capable of detecting analytes of interest within a biological sample [1]. Given the nanoscale dimensions of many biomolecules, nanotechnology provides an ideal platform to probe these molecules with high sensitivity [2]. Indeed, over the past several decades, there has been a significant effort to develop biosensors that are capable of detecting analytes at the single-molecule level [3–5]. By avoiding the averaging effects present in ensemble measurements, such sensors can provide a wealth of information about the chemical and physical properties of analytes. Outside of fundamental biological studies, single-molecule biosensors are also being developed for commercial applications such as DNA sequencing [6–8], protein analysis [9, 10], and ultra-sensitive analyte detection [11, 12]. As such, these devices hold significant promise for future applications in early stage disease diagnostics and personalised medicine.

Parts of this chapter have been published as a review article in Chemical Society Reviews [13]

Nanopores have emerged as highly promising biosensors that are capable of analyte detection at the single-molecule level [14–16]. These devices consist of a nanometre sized hole in an impermeable membrane that separates two chambers of electrolyte solution. When an electric field is applied across the nanopore, ions flow through the pore resulting in a measurable ionic current. Biosensing is then usually accomplished by detecting changes in the ionic current as a biomolecule translocates through the pore [17]. That said, nanopore sensors are not limited to ionic current based detection. In particular, nanopore sensors based on optical detection [18–20], field-effect sensing [21] and tunnelling spectroscopy [22], have attracted growing interest in recent years with each technique providing its own unique advantages.

Interest in nanopore sensors has often focused on DNA sequencing applications [23]. This can be accomplished in nanopore devices as the unique size, shape, and electronic properties of each nucleobase result in base specific changes in the measured signal as DNA traverses the pore [6, 7]. However, applications for nanopore sensors extend far beyond DNA sequencing. In particular, these devices are being developed for protein fingerprinting [9, 24, 25], polymer data storage [26, 27], biomarker detection [28–30], enzymology [31], ultra-sensitive ion sensors [32], and nanoscale chemical reactors [33, 34] to name only some. For such a wide range of applications to be achieved, it is important to be able to fabricate nanopores of variable diameters that operate in a wide range of environmental conditions. This can be achieved by fabricating nanopores in thin solid-state membranes [35]. Unfortunately, the fabrication of such pores has often relied on expensive, time consuming processes [36]. This has limited the availability of these devices amongst the research community and restricted their commercial viability.

This thesis focuses on the fabrication of solid-state nanopores and complementary nanostructures via electric field induced breakdown methods. These methods are low cost, rapid, and can be automated, thus removing the need for trained personnel. As such, it is hoped that the development of these fabrication techniques will help democratise

solid-state nanopore research and open up routes for these devices to be used in commercial applications. Before introducing these results, I will first provide a background on nanopore based biosensing with a particular focus on the use of nanopores in solid-state membranes.

1.2 Basics of Nanopore Sensing

Nanopore devices can be classified as either biological, solid-state, or a combination of the two. Biological nanopores typically consist of pore forming proteins that self-assemble and insert into lipid or synthetic membranes [37]. On the other hand, solid-state nanopores are formed in thin (<50 nm) solid-state membranes, commonly made of dielectric materials such as SiN_x [35]. In general, biological and solid-state nanopores possess their own unique advantages which makes them suited to different applications. Namely, biological nanopores can be reproducibly fabricated with atomistic precision. These devices can also be easily integrated with other biological systems (such as enzymes) which can enhance the detection capabilities of these sensors. Solid-state nanopores have the advantage that: (i) their pore diameter can be easily tuned to match the size of different analytes, (ii) they can operate in a wide range of environmental conditions, (iii) they can incorporate additional nanostructures, and (iv) they can make use of existing semiconductor fabrication processes. This thesis will focus on solid-state nanopores.

Solid-state nanopores are typically fabricated in thin SiN_x membranes suspended above a silicon handle. Silicon is generally used for the substrate since fabrication processes for this material have been well developed by the semiconductor community (although glass substrates have also been employed to reduce the device capacitance [38, 39]). Low-stress SiN_x is often used as the membrane material given its high mechanical stability, high resistivity, and dielectric strength [40, 41]. However, several other dielectrics have also been used. For example, Al_2O_3 [42, 43], TiO_2 [44], and HfO_2 [45] have been used

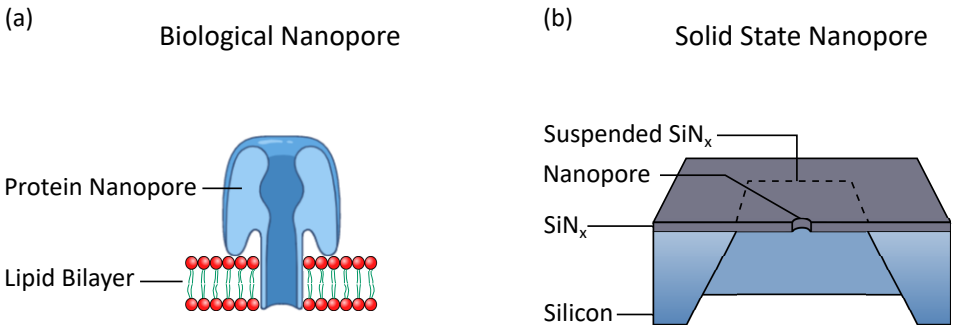


FIGURE 1.1: Schematic of different types of nanopore sensors. (a) A protein nanopore inserted into a lipid bilayer. This is a typical example of a biological nanopore. Other types of biological nanopores include peptide and DNA nanopores. (b) Schematic of a nanopore in a SiN_x membrane suspended above a Si handle. This is a typical example of a solid-state nanopore. Solid-state nanopores can also be fabricated in other dielectrics, polymers, two-dimensional materials, and glass capillaries.

to improve the pore surface charge, membrane photoluminescence, and pore stability respectively. Two-dimensional membranes such as graphene [46, 47], MoS_2 [48], hBN [49], WS_2 [50], and MXenes [51] have also been used as membranes for solid-state nanopores. Here, a micron sized aperture is typically fabricated in a SiN_x membrane and the two-dimensional film is suspended across the aperture. Solid-state nanopores have also been fabricated in quartz capillaries [52]. However, these devices have the drawback that they cannot be easily integrated with semiconductor fabrication processes for an upscaling in production.

As discussed above, nanopore devices typically work by detecting changes in the ionic current through the nanopore due to the translocation of a biomolecule [Fig. 1.2]. Here, a voltage is applied across the membrane which results in a measurable ionic current through the pore. When a biomolecule is drawn into and through the pore (typically via electrophoretic forces), if affects the passage of ions resulting in a change in the ionic current [Fig. 1.2 (a-b)]. The duration and amplitude of the change in the ionic current can be used to infer properties of the molecule such as the size, charge, and interactions with the pore surface [Fig. 1.2 (c)]. In some cases, changes in the current level during a translocation event can also be used to infer the shape [53], dipole moment [53], and sequence of the translocating entity [6]. Matching the size of the nanopore to be close to,

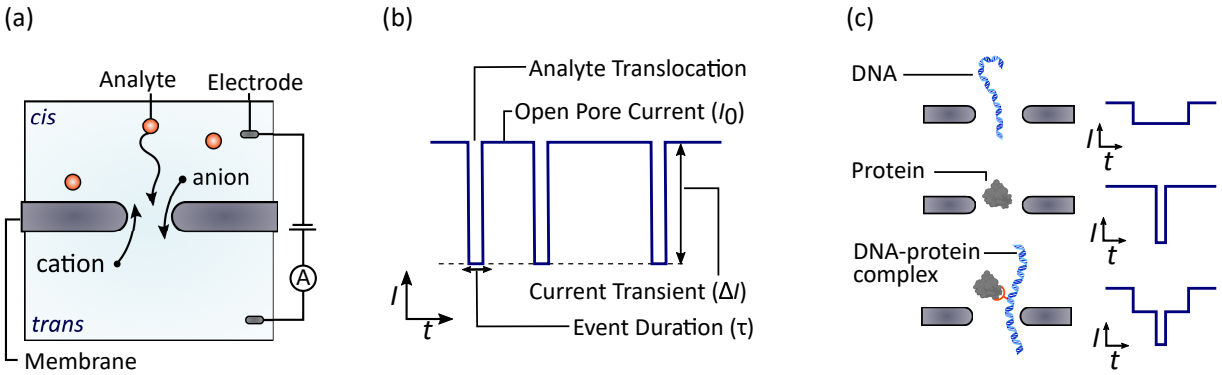


FIGURE 1.2: The basic principle of nanopore sensing. (a) Schematic of the experimental setup for ionic current based nanopore sensing. A nanopore in an insulating membrane separates two chambers of electrolyte solution. When a voltage is applied across the membrane, ions flow through the pore resulting in a measurable ionic current. When a molecule translocates through the pore it affects the passage of ions resulting in a measurable change in the ionic current. (b) Schematic of an ionic current measurement trace. The magnitude and duration of the current transient can be used to infer properties such as size, charge, and shape of the biomolecule. (c) Examples of the translocation of various biomolecules through a nanopore and schematics of the corresponding change in ionic current. These are only three examples of the vast array of biomolecules that have been detected using nanopore sensing.

but slightly larger than, the size of the analyte generally maximises the measured signal. This sensing modality has had significant success in detecting a wide range of analytes including DNA [54], RNA [55], proteins [56], and nanoparticles [57].

Despite the significant success of ionic current based sensing, this technique suffers from several limitations. Firstly, the maximum bandwidth obtainable with this sensing modality is typically limited to <1 MHz. This results from the increased capacitive noise at high frequencies which reduces the signal-to-noise ratio to a point where translocation events can no longer be detected [58–60]. Some impressive works have recently been done on reducing the system capacitance by integrating the current amplifier in close proximity to the nanopore device [61] or reducing the device capacitance [39, 62]. This has enabled the measurement of DNA translocation events at frequencies up to 10 MHz [63]. However, such measurements require significant optimisation and further increases in the obtainable bandwidth appear to be challenging. Another significant issue with ionic current based sensing is that this technique has a limited device density. This results from the fact that,

for nanopores to be read out independently, each pore must be fluidically isolated [21, 64]. This requires complex microfluidics and limits the obtainable device density [65]. To overcome these issues, several advanced nanopore sensing techniques have been developed as discussed below.

1.3 Advanced Solid-State Nanopores

To overcome the challenges associated with ionic current based sensing, there have been several efforts to incorporate additional sensing modalities with nanopore devices to enhance their capabilities. This includes the use of field-effect sensors, tunnelling nanogaps and optical sensing strategies [Fig. 1.3]. Some interesting preliminary results have also been obtained by integrating nanopores with radiofrequency antennas [66], and dielectrophoretic electrodes [67, 68], however these won't be discussed in detail here.

Field Effect Sensors

A field-effect sensor, or field-effect transistor (FET), is a device whose conductance is sensitive to the local electric potential. Integrating a FET with a nanopore provides an alternative sensing modality to ionic current based sensing. This is because the translocation of biomolecules through a nanopore modifies the local electric potential and can therefore be detected by changes in the conductance of the FET.

This technique was first demonstrated by integrating a silicon nanowire with a nanopore [Fig. 1.3(a)] [21]. Since then, several studies have integrated two-dimensional FETs made of graphene [64, 69, 70] and MoS_2 [71] with a nanopore. All of these studies have demonstrated that it is possible to detect the translocation of biomolecules through a nanopore by measuring changes in the current of a nearby FET. It has also been shown that such changes in the current can result from either capacitive coupling or electrostatic gating of the FET [64, 70]. These studies have also highlighted the difficulties in fabricating

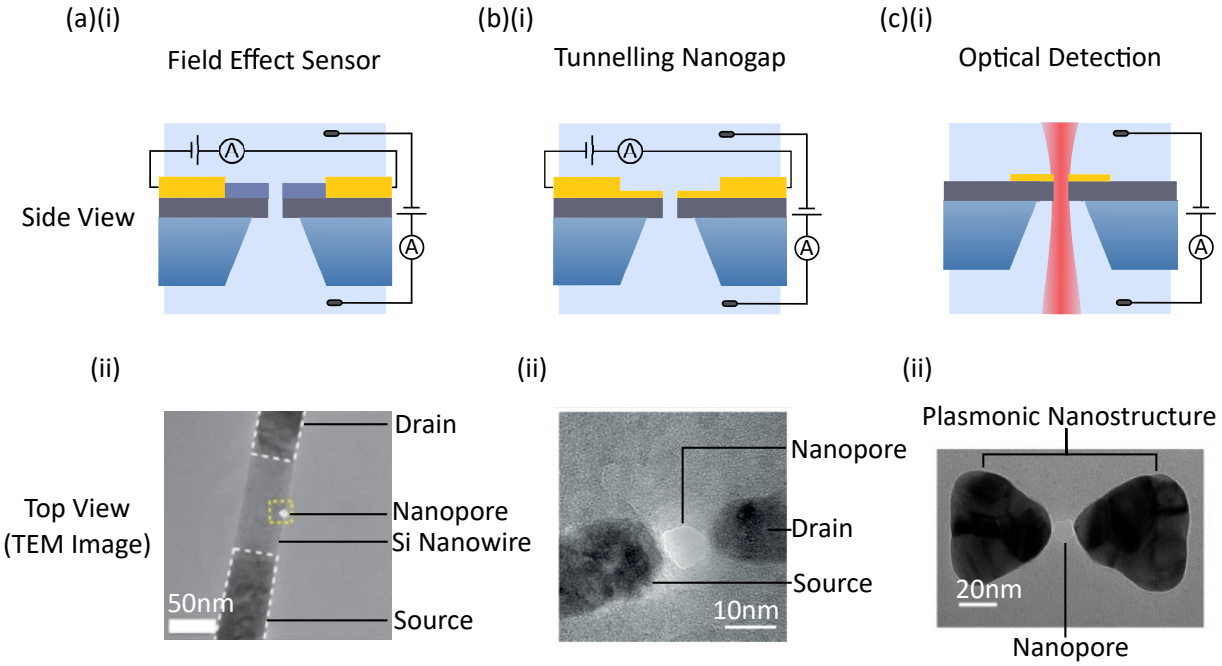


FIGURE 1.3: Examples of several advanced nanopore sensing techniques. (a) Field-effect sensor integrated with a nanopore. (b) Electron tunnelling nanogap electrodes integrated with a nanopore. (c) Plasmonic nanostructures integrated with a nanopore. For each technique a schematic of the device geometry is shown in (i) and a TEM image of the top view of the device is shown in (ii). TEM images were taken with permission from (a)(ii) [21], (b)(ii) [72], and (c)(ii) [73]

nanopores integrated with a FET. Such difficulties result from the relatively low yield and time-consuming nature of several of the fabrication steps (e.g. drilling of nanopores and sculpting of the FET in a transmission electron microscope). Indeed, one study reported that only one out of 180 devices that begun the fabrication process was successfully used for sensing [64].

Integrating a nanopore with a FET has two major advantages over ionic current based sensing. Firstly, these devices can be fabricated with high density and the signal from each FET read out independently [21]. This is in contrast to ionic current based sensing where each pore must be fluidically isolated thus placing a limit on the device density that can be obtained. Secondly, these devices typically have a high conductance and therefore don't require sensitive amplifiers to measure the current through the device. The result of this is that capacitive noise no longer dominates the signal at high frequencies (>10 kHz) [60].

As such, these devices can easily operate in the megahertz regime with high signal-to-noise ratios, thus overcoming the bandwidth limitation of ionic current based sensing.

Tunnelling Nanogaps

Tunnelling nanogap devices consist of a small nanogap ($\leq$5 nm) between two conductive electrodes. When an electric potential is applied between the electrodes, electrons can tunnel through the potential barrier resulting in a small (picoamps-nanoamps) measurable current. Placing a molecule of interest within the gap results in a change in the measured current as electrons now tunnel through the molecule [74].

The first study demonstrating the integration of tunnelling electrodes with a nanopore was reported in 2011 [22]. In this study, a nanopore was fabricated between microelectrodes via focused ion beam milling. Electron beam induced deposition was then used to create a tunnelling nanogap at the tip of the microelectrodes. Unfortunately, when passing DNA through the nanopore, the majority of translocation events were only observed in the ionic current channel. However, some long-lived events were observed simultaneously in the tunnelling and ionic current, potentially as a result of DNA sticking to the electrodes. Subsequent studies on metal [72, 75] and carbon [76] nanogaps aligned with nanopores [Fig. 1.3(b)] have also reported great difficulty in reproducibly observing simultaneous DNA translocation events in the ionic current and tunnelling current signals. Unfortunately, due to the difficult and time-consuming nature of the fabrication of such devices, these issues have largely remained unsolved [75].

To attempt to overcome some of the difficulties involved in the fabrication of these devices, several innovative techniques to integrate tunnelling nanogaps with a nanopore have been suggested. Layered tunnelling electrodes have been fabricated by defining a nanogap between two electrodes via atomic layer deposition [77]. A pore was then fabricated in this layered structure via electron beam lithography followed by reactive ion etching. By functionalising the electrodes with 'reader' molecules, the authors were able to detect

and identify individual nucleotides as they diffused into the nanogap based on changes in the tunnelling current. However, these devices possess their own challenges as nanopore fabrication often resulted in electrode damage. Another technique to fabricate nanogaps aligned with nanopores relied on the electromigration of gold electrodes sandwiched between SiO_2 layers [78]. This technique resulted in the fabrication of a nanogap self-aligned with a nanopore. Using these devices the authors were able to detect short DNA strands diffusing into the nanogap.

The main advantage of tunnelling nanopore devices is their sensitivity to the electronic structure of the translocating analyte. Studies on tunnelling nanogaps not integrated with a nanopore have demonstrated the ability to detect and distinguish between different nucleobases [79–82], amino acids [83] and carbohydrates [84] as well as chemical modifications of these biomolecules [85]. Tunnelling nanogaps have also provided interesting results on the fundamental electronic properties of proteins [82, 86–88]. Tunnelling nanopore devices would also enable high device densities as each nanogap can be measured independently without the need for fluidic isolation.

Optical Nanopores

Several optical sensing strategies have been integrated with nanopore devices. This includes using fluorescently labelled molecules, the detection of Ca^{2+} indicator dyes, and the use of plasmonic nanostructures. I will introduce the basics of some of these detection strategies below. For a more detailed discussion the reader is referred to Refs. [18–20].

One such optical based sensing modality relies on labeling the analyte of interest with a fluorophore and detecting changes in the optical signal as the analyte translocates through the pore. However, the detection of single fluorophores with sub-millisecond resolution is typically challenging due to background noise. To overcome this, total internal fluorescence has been used to suppress the signal from the bulk solution [89]. Using this technique, synchronised optical and electrical translocation of DNA through a solid-state

nanopore has been detected [89]. Building on this result, a DNA strand was labelled with molecular beacons using two types of fluorophores. When the DNA translocated through a small nanopore (<2 nm) the beacons were cleaved from the DNA leading to sequential fluorescence bursts corresponding to the sequence of DNA [90]. The background signal in such measurements has also been reduced by decreasing the photoluminescence from the membrane. For example, TiO_2 membranes have been used rather than SiN_x as this dielectric demonstrates a reduced photoluminescence at the wavelength of interest [91, 92]. Irradiation of SiN_x with He^+ ions [93] or electrons [94] has also been used to reduce the photoluminescence of SiN_x.

Another optical based nanopore sensing technique relies on the detection of Ca^{2+} ions using an indicator dye [95, 96]. In this technique, Ca^{2+} ions are added to the electrolyte on one side of the membrane, while a Ca^{2+} indicator dye such as Fluo-4 is added to the electrolyte on the other side of the membrane. Applying an appropriate voltage to drive Ca^{2+} ions through the nanopore therefore results in a localised fluorescence signal at the nanopore opening. Monitoring changes in the fluorescence signal enables the detection of biomolecular translocation events. The main advantage of this technique is that the signal from each nanopore can be read out independently, thus enabling highly multiplexed sensing via the use of nanopore arrays. A droplet interface bilayer can also be used to extend this approach to biological nanopores [97].

Plasmonic nanostructures have also been integrated with nanopore devices to enable optical based sensing. These nanostructures can produce strong, localised optical fields resulting from the oscillation of free electrons in a metal (i.e. the plasmon effect). Various plasmonic nanostructures have already been integrated with nanopores including bow-tie nanoantennas [73], plasmonic nanowells [98], plasmonic bullseyes [99], and gold nanoparticles [100]. The highly localised optical signal created by a plasmonic nanostructure can be used to significantly increase the fluorescence intensity of labeled molecules thus providing a higher signal-to-noise ratio in these devices [98]. The focused optical field

of these sensors also allows for the localised measurement of scattered/transmitted light which has enabled label-free optoelectrical measurements of biomolecular translocations [101, 102]. Plasmonic nanopores can also enable localised heating of the electrolyte [73] or the creation of optical traps [103, 104] which provides additional control over the capture and translocation of biomolecules through the nanopore.

1.4 Fabrication of Solid-State Nanopores

Given the above discussion, it is perhaps already clear that a major challenge in developing solid-state nanopore sensors is the ability to fabricate these devices in a scalable and accurate fashion. This is particularly true for the advanced nanopore devices discussed above which often require pores to be integrated with additional nanostructures. A major focus of this thesis is to develop accessible techniques to fabricate nanopores and complementary nanostructures. As such, it is worth reviewing some of the techniques that have been used to fabricate solid-state nanopores to date. Given the significant interest in solid-state nanopore devices, a large number of fabrication techniques have been developed [36]. As such, it is not practical to discuss all of these methods. Rather, I will focus on some of the most commonly used techniques. A timeline of the development of these techniques is shown in Fig. 1.4 along with the approximate minimum pore diameter that has been obtained using each method. Each of the techniques shown in Fig. 1.4 is discussed below, with the exception of controlled breakdown and electrochemical reaction that are discussed in more detail in Chapter 2.

Ion Beam Sculpting

Solid-state nanopores with dimensions on the order of a few nanometres were first reported in 2001 using an ion beam sculpting technique [105]. Here, a bowl-shaped cavity was fabricated in a SiN_x membrane using reactive ion etching. Following this, energetic Ar^+ ions were used to thin the membrane on the opposite side to the cavity. When the planar

surface intercepted the bowl-shaped cavity, a nanopore was created in the membrane. Nanopore formation was detected by monitoring the transmission of Ar^+ ions through the membrane, enabling the controlled fabrication of pores with diameters down to 1.5 nm.

TEM Drilling

Shortly after this, nanopores were fabricated using a transmission electron microscope (TEM) [106]. In the initial demonstration of this, relatively large pores (∼20 nm) were first created in the membrane using electron beam lithography and anisotropic etching [106]. The pore was then exposed to the electron beam from a TEM which fluidises the membrane. Depending on the pore size and the membrane thickness, this can lead to shrinking of the nanopore diameter due to a decrease in the surface tension. The nanopore diameter can be monitored in real time using the TEM. Moreover, when the electron beam is removed, the pore retains its shape thus enabling controlled fabrication of nanopores with diameters down to a single nanometre. Nowadays, it is more common to directly drill nanopores in a solid-state membrane using a TEM [107–109]. Here, the membrane is subjected to a tightly focused electron beam with a spot size typically less than a few nanometres. When the high energy electrons (typically accelerated at ∼200 kV) interact with the membrane they cause sputtering of the material resulting in the formation of a nanopore.

FIB Milling

Direct drilling of nanopores using charged particles can also be performed using a focused ion beam (FIB). This can be done using a range of different ions, however, Ga^+ [110, 111] and He^+ [112, 113] are currently the most common. Due to the heavier mass of ions compared to electrons (and differences in the way they interact with the sample), the nanopore diameter obtainable using a FIB is typically larger than what is possible using a TEM. However, nanopores with diameters down to approximately 5 nm [110] and 1.3 nm [113] have been fabricated with Ga^+ and He^+ ions respectively. Reproducibly obtaining

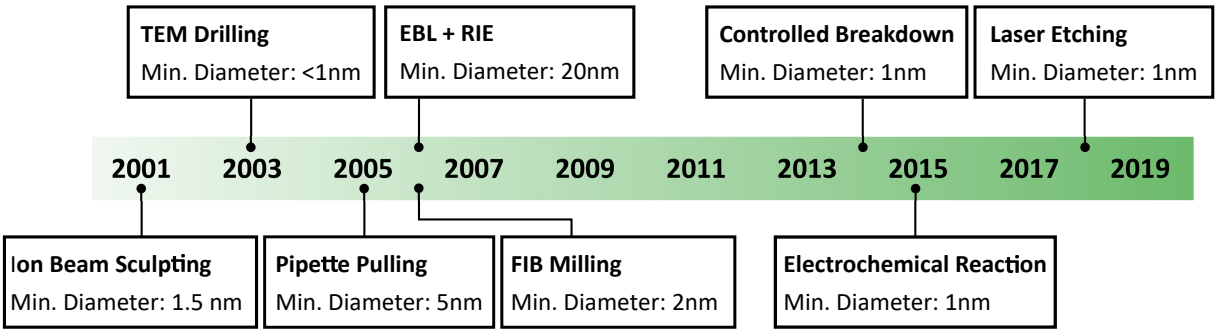


FIGURE 1.4: Timeline showing the development of different solid-state nanopore fabrication techniques. The approximate minimum nanopore diameter that has been reported in the literature to date is also shown.

such small pore sizes can be difficult and requires an experienced operator. Fabricating nanopores using a FIB has the advantage that (unlike in a TEM) multiple devices can be loaded into the microscope, thus enabling drilling of nanopores over relatively large areas [114]. Drilling of nanopores in a FIB can also be largely automated (whereas a TEM is typically manually operated) making the production of nanopore arrays easier. Note that direct drilling of nanopores using charged particles can result in damage to surrounding nanostructures, making these techniques incompatible with some nanopore devices [77, 115, 116]. Drilling nanopores using charged particles can also lead to changes in the fundamental membrane composition which may decrease the pore stability [109, 117].

Electron Beam Lithography

Another method used to fabricate solid-state nanopores relies on the well-developed nanofabrication techniques of electron beam lithography (EBL) and reactive ion etching (RIE) [30, 115, 118, 119]. Here, nanopores are patterned into an electron sensitive resist using EBL and this pattern is transferred to the membrane via RIE. Similar to FIB milling, this technique can be used to create high density arrays of nanopores over large areas [120]. However, it is challenging to reproducibly fabricate pores with diameters less than 20 nm using this technique. The obtainable pore diameter can be reduced

by performing atomic-layer deposition following nanopore fabrication [121] or by using anisotropic etching rather than RIE to create the pore [122].

Pipette Pulling

The techniques discussed above rely on specialised equipment which require highly trained personnel to operate. This initially limited the availability of solid-state nanopores to a relatively small community. Recently, there has been significant progress in developing accessible techniques to fabricate solid-state nanopores. One such technique is the laser-assisted pulling of pipettes. These nanopores are typically fabricated from glass or quartz capillaries by the application of heat simultaneous to a pulling force from each end of the capillary [123–127]. By adjusting the fabrication parameters (e.g. applied heat and pulling force), it is possible to produce nanopipettes with opening diameters of several nanometres [128]. While the simplest nanopipettes contain just a single nanopore at their tip, nanopipettes with two [129] and four barrels [130], each containing a nanopore, have also been demonstrated. In these multi-barrelled nanopipettes, each nanopore is independently addressable and can be used for sensing and trapping with multiple pores. Barrels can also be selectively filled with conductive materials that can be used for field-effect gated molecular transport or to enable additional detection modalities [15, 82, 131]. The surface of nanopipettes can be functionalised via salinisation chemistry with antibodies for the selective capturing and detection of analyte molecules [132–135]. Nevertheless, the wider deployment of these nanopores is limited by difficulties in the production of pore arrays as well as nanopipettes with reproducible pore sizes.

Laser Etching

The last solid-state nanopore fabrication technique that will be discussed here is laser etching. This technique relies on focusing a low power ($\sim$10 mW), blue-green laser on a Si-rich SiN_x membrane to induce localised etching and nanopore formation [136, 137]. A small transmembrane voltage ($\sim$200 mV) is applied during laser etching to provide

feedback on the creation of a nanopore. Laser induced etching of a SiN_x membrane is assumed to result from the photochemical destabilisation of Si-Si bonds in the membrane material [138]. In particular, blue-green light activates charge separation between Si bonds leading to its destabilisation. The photoactivated Si then forms transient compounds with the anions (e.g. Cl^-) in solution. These transient compounds are then oxidised to form SiO_2 which solubilises in water resulting in etching of the membrane.

Laser etching is a particularly promising pore fabrication technique for optical based nanopore sensing strategies as discussed in Sec. 1.3. The need for precise alignment of the nanopore with the optical path can be a bottleneck for this detection modality. Nanopores fabricated via laser etching partially overcome this issue by creating pores that are self-aligned with the optical path (although stage drift can be problematic and result in misalignment). Moreover, laser etching can be used to create high density arrays of nanopores [137]. This is useful for optical nanopore sensing strategies whereby the signal from each nanopore can be read out independently without the need for electronic and fluidic isolation [90]. Additionally, laser etching can be used to create ultrathin nanopores (<5 nm) since pores are formed from a thinning process. Ultra-thin nanopores are generally preferred in biosensing applications as they maximise the ionic current signal [46, 63]. Continued research into this nanopore fabrication technique should further extend its capabilities. In particular, while this technique has been demonstrated on Si-rich SiN_x films, it is yet to be seen whether it can be extended to other dielectric membranes. Laser etching can also be susceptible to forming multiple undesired nanopores. In particular, it was demonstrated that multiple nanopores form in close proximity if laser etching is not terminated shortly after pore formation (within a matter of seconds) [137]. As such, the experimental protocols to perform laser etching may require further optimisation to enable the creation of single nanopores with diameters larger than 10 nm.

1.5 Thesis Outline

Hopefully a few salient points are clear to the reader from this introduction.

1. Nanopores are highly promising sensors capable of label-free detection down to the single-molecule level for a diverse range of applications.

2. Fabricating nanopores in solid-state membrane provides advantages over biological nanopores for several applications. This includes the ability to tune the pore size, diverse operating conditions, and the potential to leverage existing semiconductor fabrication techniques.

3. Integrating complementary nanostructures with solid-state nanopores provides several advantages over traditional ionic current nanopore sensors. These advantages include the ability to operate at high bandwidth, high device density, as well as sensitivity to molecular properties not possible using ionic current based detection.

4. The fabrication of solid-state nanopores has traditionally been a time-consuming process with limited throughput. This is especially true for nanopores that require alignment with complementary nanostructures. To date, this has limited the development of these devices.

This thesis addresses some of these issues by focusing on electric field breakdown techniques to fabricate nanopores and complementary electrodes (and integrate these two structures). The electrical breakdown techniques discussed in this thesis are fast, relatively inexpensive and fully automatable. This thesis is set out as follows.

Chapter 2 introduces the controlled breakdown technique to fabricate solid-state nanopores. Here, I review the basics of this technique and highlight the advantages and challenges of this nanopore fabrication method. The controlled breakdown setup that I have built during my studies is also introduced. I demonstrate the basic capabilities of this setup

to fabricate solid-state nanopores and detect the translocation of double stranded DNA through these pores.

Chapter 3 discusses the mechanism of electrical conduction and nanopore formation during controlled breakdown. Here, I demonstrate that, depending on the membrane stoichiometry electrical conduction is limited by either oxidation reactions that occur at the membrane-electrolyte interface (Si-rich SiN_x), or charge transport through the dielectric (stoichiometric SiN_x). I provide details of several important implications that result from understanding this process that will aid in further developing controlled breakdown, particularly for extending this technique to fabricate nanopores integrated with on-chip nanostructures.

Chapter 4 discusses the development of a new controlled breakdown protocol to fabricate solid-state nanopores. In this method, the voltage is applied between an on-chip electrode and an electrolyte solution in contact with the other side of the membrane. Using this method, I demonstrate the ability to fabricate multiple nanopores in a single membrane without affecting the previously created pores. I also demonstrate that nanopores created via this method are suitable for single-molecule biosensing applications. This controlled breakdown method is a step towards the development of an accessible, rapid, and scalable technique to fabricate arrays of solid-state nanopores aligned with complementary on-chip nanostructures.

Chapter 5 introduces a technique to fabricate solid-state nanopores self-aligned with complementary nanoelectrodes on the membrane surface. This technique relies on passing a large current density through an on-chip metal nanoconstriction to locally heat the membrane. By performing controlled breakdown simultaneous to heating, I demonstrate that nanopore formation is localised to the hottest part of the substrate. This is a versatile, accessible, and high throughput method to fabricate solid-state nanopores self-aligned with on-chip nanostructures, thus making this a promising technique to overcome existing challenges in the fabrication of these devices.

Chapter 6 discusses the fabrication of graphene nanoelectronic devices for single-molecule biosensing applications. These devices are fabricated via Joule heating of graphene nanoconstrictions to the point where carbon atoms are oxidised/sublimated. The noise in these devices is studied with a view towards using them for single-molecule biosensing applications. I report on the observation of large amplitude charge noise in these devices and provide details of practical implications resulting from this noise for the use of these devices as single-molecule biosensors.

Chapter 7 provides a summary of the main results of this thesis.

Chapter 2

The Basics of Controlled Breakdown

In this chapter I will discuss the fabrication of solid-state nanopores using controlled breakdown (CBD). In particular, I will review the use of CBD and discuss the advantages and challenges of this nanopore fabrication technique. The experimental setup that I have developed to perform CBD in our laboratory will then be introduced. It is demonstrated that, using this setup, I am able to create nanopores in SiN_x membranes and measure the translocation of DNA molecules through these pores.

2.1 Basic CBD Protocol

Controlled breakdown is an appealing solid-state nanopore fabrication technique that can be fully automated and performed using relatively accessible equipment [139]. This technique was first reported in 2014 [140] and has gained popularity in recent years [29, 141–144]. This nanopore fabrication method relies on applying a large electric field (∼0.6-1 V/nm) across the membrane to induce dielectric breakdown and nanopore formation.

The basic experimental setup of CBD is shown in Fig. 2.1(a). The setup consists of a suspended membrane (typically SiN_x) separating two chambers of electrolyte solution

Parts of this chapter have been published as a review article in Chemical Society Reviews [13]

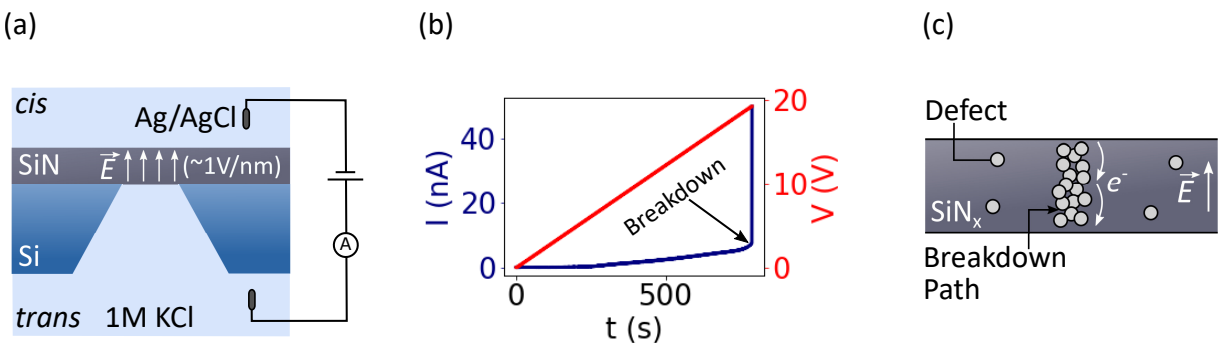


FIGURE 2.1: (a) Schematic of the experimental setup used for CBD. (b) A typical experimental trace of CBD. In this example, a voltage ramp was applied, however, a constant voltage, voltage pulses, and a constant current can also be used for CBD. (c) Simplified schematic of the assumed process of dielectric breakdown. As discussed in Chapter 3 the process is more complex for CBD since the electric field is applied via an electrolyte solution.

(typically 1 M KCl). Electrodes (typically Ag/AgCl) are placed in each chamber enabling a voltage to be applied across the membrane. The two chambers of electrolyte solution are referred to as *cis* and *trans* corresponding to the chamber that the negative and positive voltage is applied to respectively. A typical experimental trace of CBD is shown in Fig. 2.1(b). The application of a large voltage across the membrane results in the small leakage current. After a period of time, a jump in the current is observed signifying dielectric breakdown and nanopore formation. When this occurs, the voltage is quickly reduced to zero (typically within 1-100 ms [139, 140]) to avoid catastrophic failure of the membrane. Note, although a voltage ramp is shown in Fig. 2.1(b), CBD has also been performed using a constant voltage [140], voltage pulses [145], and a constant current [146]. In general, CBD can be achieved using any protocol whereby a sufficiently large electric field is applied across the membrane. This technique can be performed using largely the same experimental setup required for nanopore sensing, with the addition of a voltage source capable of applying potentials up to approximately 30 V (the specific voltage required will depend on the membrane being used). A current amplifier capable of measuring large currents and applying high voltages may also be required since most commercial amplifiers used for nanopore sensing are limited to apply 1 V and measure up to 200 nA.

The mechanism of nanopore formation during CBD is generally assumed to result from the same process as the well-studied case of dielectric breakdown in semiconductor and microelectronic devices [147, 148]. A schematic of this process is shown in Fig. 2.1(c). The process is generally understood as follows. When a large electric field is applied across a dielectric, a leakage current flows through the material due to electric field assisted electron transport through charge traps (defects) in the dielectric [149, 150]. At some point, these charge traps form a percolation path leading to a spike in the current across the membrane. This increase in current results in physical damage to the dielectric, potentially as a result of Joule heating. However, as discussed in Chapter 3, the breakdown process is more complex for CBD since the electric field is applied via an electrolyte solution. As a result, electron transfer (redox) reactions must occur at the membrane-electrolyte interface for a current to flow across the membrane. As will be discussed later, such redox reactions can limit the current flowing across the membrane and therefore affect the breakdown dynamics.

Following CBD, the diameter of the nanopore can be enlarged thus enabling tailoring of the pore size to the dimensions of the target analyte [151]. Nanopore expansion is achieved by applying voltage pulses and measuring the pore conductance at low bias between each pulse to enable feedback on the nanopore size [139, 151]. The pore expansion pulses should have reduced amplitude compared to the breakdown voltage (typically 0.3-0.5 V/nm) to enable widening of pre-existing nanopores while reducing the probability of creating additional pores [139]. It should also be noted that nanopore enlargement proceeds via a fundamentally different mechanism to nanopore formation via CBD. Although not well understood, it is thought that nanopore enlargement occurs via the electrochemical dissolution of membrane material along the pore walls driven by the flow of ionic current [152].

2.2 Advantages of CBD

In addition to the accessibility of CBD, this technique possesses some additional unique advantages over other nanopore fabrication techniques. Firstly, this technique does not require direct line of sight to the membrane. Rather, nanopores can be created using CBD as long as there is a fluidic connection between the electrodes and the membrane. This opens up the possibility to fabricate nanopores integrated with complex geometries not possible using other pore fabrication methods. Utilising this advantage, nanopores were fabricated in a SiN_x membrane which was separated from a nanoporous membrane by a sub-micron sized distance [142, 153, 154]. Using this device structure, it was demonstrated that the conformation of DNA could be controlled by passing the molecules through the nanoporous membrane prior to translocation. This resulted in a narrower distribution of dwell times, and in some cases, a reduction in the number of folded translocation events. The ability to create nanopores via CBD without line-of-sight also enables the integration of nanopores with microfluidic structures which can be used for multiplexing [65, 155]. Microfluidic structures have also been integrated with a nanopore to enable isotachophoretic [144] and convection based [156] focusing of analytes at the nanopore.

Another advantage of CBD is that the breakdown process is a general phenomena and can be used to create nanopores in a range of membrane materials. This is in contrast to methods such as laser etching, which rely on specific photochemical reactions to create nanopores. While most studies have created nanopores in SiN_x membranes [140, 145, 147, 157–160], CBD has also been used to create nanopores in other dielectrics such as SiO_2 [140], TiO_2 [92], and HfO_2 [161]. Nanopores have also been fabricated in membranes where a gold layer was deposited on top of the SiN_x [162]. As will be discussed in detail in this thesis, this is an important result for the fabrication of nanopores integrated with on-chip electrodes. Given the generalisability of this technique, one might anticipate seeing CBD extended to different dielectric materials such as Al_2O_3 [42, 43] in the coming years.

Studies have also demonstrated the ability to control the surface properties of SiN_x nanopores fabricated via CBD. Controlling the surface properties of solid-state nanopores is important to reduce pore clogging resulting from analyte-membrane interactions [143]. Moreover, it offers a route towards selective biomolecular detection [163–165]. It has been demonstrated that adding NaClO to the solution during CBD resulted in a significant change in the surface charge of the nanopore, even after the electrolyte was replaced [143]. For DNA translocation experiments, this change in surface charge resulted in an increase in the event frequency and less pore clogging due to reduced electrostatic interactions between the pore walls and the translocating molecule. The mechanism by which the addition of NaClO during CBD affects the nanopore surface charge is not well understood and may be an interesting area of future research. CBD has also enabled functionalisation of the pore walls with a number of molecules via photohydrosilylation [166]. Such functionalisation of SiN_x films generally requires the removal of a native oxide layer via hydroflouric acid etching [167, 168]. However, this is not suitable for nanopore functionalisation since it results in unacceptable widening of the nanopore. Rather, the *in situ* nature of CBD means that photohydrosilylation can be performed without exposing the pore to the atmosphere, thus preventing the formation of a native oxide layer.

2.3 Challenges of CBD

Despite the promise of CBD, there are also some challenges in using this technique to fabricate solid-state nanopores. Several of these issues are highlighted in Fig. 2.2. One such challenge is that CBD can result in the formation of multiple pores [169–171]. The formation of multiple pores is typically an issue when the desired pore diameter is large (>20 nm). This is because during the pore expansion phase the membrane will be subject to large electric fields for time periods comparable to those required to induce new breakdown events. It has recently been shown that increasing the conductivity of the solution during the pore expansion phase decreases the probability of forming multiple pores [152].

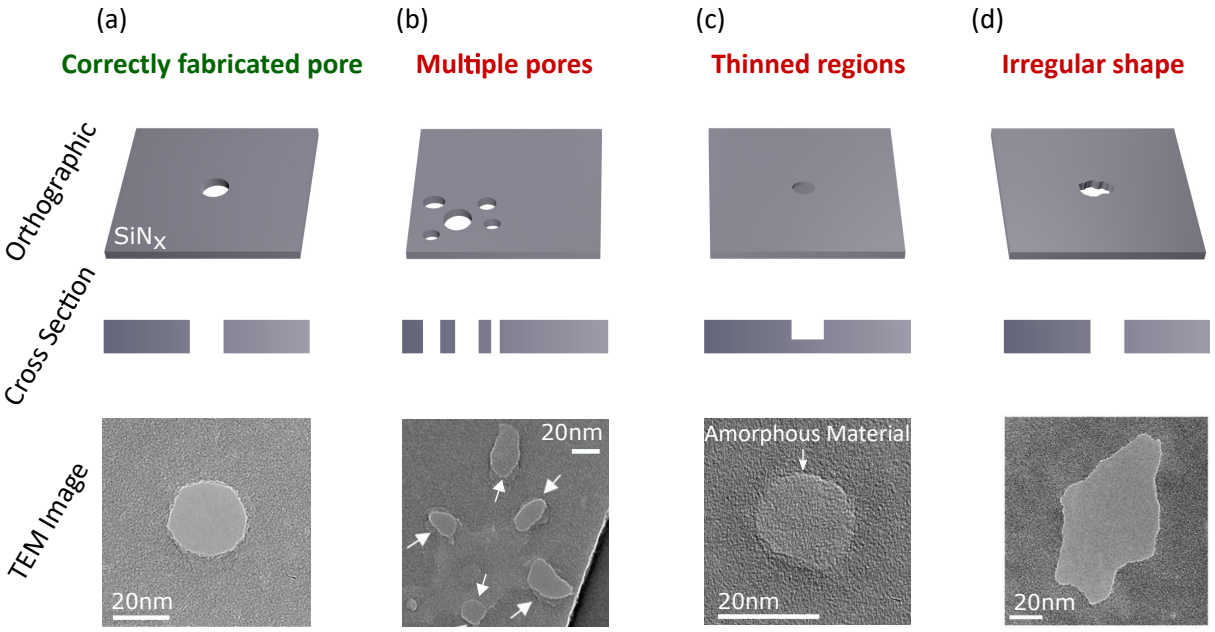


FIGURE 2.2: Orthographic schematic (top), cross section schematic (middle), and TEM image of several issues encountered during CBD. (a) A correctly fabricated pore. (b) The formation of multiple nanopores. (c) The formation of a thinned region in the membrane rather than a nanopore. (d) Fabrication of irregularly shaped nanopores. TEM images were taken with permission from [172] and [173].

This is because nanopore expansion is driven by electrochemical reactions resulting from ionic current flow through the pore. As such, increasing the conductivity of the solution allows for high ionic currents at lower voltages, thus enabling nanopore expansion with a decreased risk of new breakdown events.

Despite these advances, it may still be useful for researchers developing CBD techniques to test if the protocol/experimental conditions being used result in the formation of multiple nanopores. Unfortunately, multiple pores can not be easily distinguished from a single pore using conductance measurements (although more information can be obtained by performing analyte translocation [152, 174]). As a result, several techniques have been developed to detect the presence of multiple pores created via CBD. One method is to measure the change in pore conductance resulting from coating the pore in a self-assembled monolayer [24, 53, 169, 174]. The basis of this technique is that coating multiple small nanopores will result in a larger change in the conductance than coating a single pore of equivalent area. Unfortunately, it is difficult to obtain conclusive results using this method

since incomplete coating of the pore leads to significant uncertainties in the change in conductance [169].

Fluorescence microscopy has also been used to detect the presence of multiple pores created during CBD. In this technique Ca^{2+} ions are added to the electrolyte on one side of the membrane and a Ca^{2+} indicator dye such as Fluo-4 is added to the other side [95, 96, 171]. When a voltage is applied across the membrane to drive Ca^{2+} ions through the nanopore, a localised fluorescence signal is created at the pore. This enables the detection of multiple nanopores, as well as the position of each pore. Indeed, using this technique it was demonstrated that for one batch of devices, a disproportionate number of nanopores created via CBD form at the membrane edge (for another batch of devices the pores formed at random locations) [171]. Although the reason for this remains unclear, the fact that this phenomenon is batch dependent suggests that it results from variations in the fabrication process. Spatial constraints may alter the translocation dynamics of long biomolecules with a radius of gyration comparable to the distance between the pore and the membrane edge. Laser-enhanced ionic current mapping can also be used to detect multiple nanopores and determine the position of each pore [175]. Here, a laser is scanned across the membrane while simultaneously monitoring the ionic current through the pore. When the laser position is aligned with the nanopore, an increase in the ionic current is observed due to localised photothermal heating resulting in a decreased electrolyte viscosity [176].

It has generally been assumed that the formation of multiple nanopores during CBD occur as independent processes, with each pore forming at a random location in the membrane. However, TEM imaging of nanopores formed by CBD demonstrated that without adequate feedback conditions on membranes that require large voltages to undergo breakdown (>20 V), multiple pores may be formed in close proximity to each other [Fig. 2.2(b)] [172]. The presence of multiple pores could not be explained by the statistics governing independent breakdown events. Instead, it was suggested that Joule heating resulting

from the large ionic current through the initial nanopore can lead to localised heating of the substrate that promotes subsequent adjacent breakdown events [172]. Unfortunately, due to limits in resolution, the fluorescence microscopy and laser enhanced ionic current mapping techniques cannot easily distinguish pores in close proximity.

Another interesting result obtained from TEM imaging of nanopores fabricated via CBD is that this process can result in the formation of a thinned region in the membrane rather than a nanopore [Fig. 2.2(c)] [172, 173]. Interestingly, these thinned regions demonstrated non-negligible transmembrane conductance (tens of nanosiemens), but could be distinguished from nanopores due to the significant rectification in the measured current [172, 173]. Unfortunately, it is not clear whether such thinned regions are a widespread phenomenon that have remained undetected in other studies or are specific to the experimental conditions used in these works. It is noted that for SiN_x membranes thicker than 10 nm, the effective length of nanopores fabricated via CBD has been reported to be approximately one third of the membrane thickness [145, 158, 159, 171]. This suggests that membrane thinning may be present in these studies as a precursor step to pore formation. Further to this point, it was shown that such thinned regions can be penetrated to form nanopores by applying voltage pulses of opposite polarity to the initial breakdown voltage [172]. Such pulses are routinely applied during what is assumed to be a pore expansion phase. However, following the above study, it may be the case that in some works these voltage pulses are penetrating a thinned region rather than expanding the nanopore. Performing CBD in a high pH solution (pH>12) can also create nanopores rather than thinned regions in the membrane [173].

Lastly, CBD can result in irregularly shaped nanopores [Fig. 2.2(d)]. This is particularly apparent for large pore areas (conductance equivalent to diameters greater than ∼20 nm). Such irregularly shaped pores may result in a misinterpretation of the ionic current changes resulting from the translocation of an analyte through the nanopore. While I have highlighted some of the challenges of CBD above, it should be emphasised that this remains

a powerful technique to create nanopores with diameters down to a single nanometre. Indeed, many of the challenges described above can be avoided by optimising the fabrication procedure for a given membrane composition/geometry and electrolyte environment. It has been shown that using optimised procedures, CBD creates nanopores with acceptable properties for sensing applications in approximately 85% of cases [139]. It is hoped that this value will increase even higher with further studies into the fundamental mechanism of CBD.

2.4 Advanced CBD Methods

One of the limitations of CBD is that the stochastic nature of this process results in nanopores forming at random locations in the membrane. This is a particular problem if pores are to be integrated with complementary on-chip nanostructures required to enable sensing modalities in addition to ionic current based sensing (as discussed in Sec. 1.3). Positioning of the nanopores is also required for dual nanopore devices which have been used to control the translocation dynamics of biomolecules [177–179].

To overcome this issue, various techniques have been demonstrated that enable positioning of nanopores fabricated via CBD. Techniques that have been demonstrated in the literature to date, along with a schematic representation of how each method is achieved, are shown in Fig. 2.3. The first of these methods relies on selectively thinning a portion of the membrane [Fig. 2.3(a)]. Given the breakdown voltage depends approximately linearly on the membrane thickness [158], this will result in nanopores forming at the thinnest part of the membrane. This technique has been demonstrated using a He^+ FIB [180] as well as EBL followed by RIE [29, 171] to locally thin regions of the membrane. However, the large capital cost of these instruments limits the availability of this method for many researchers. Rather than thinning the membrane, a dielectric could also be patterned on the membrane surface to localise nanopore formation [140].

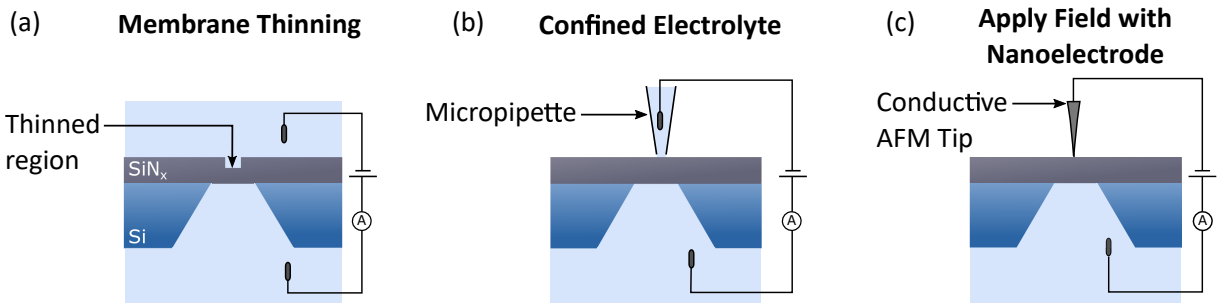


FIGURE 2.3: Three advanced CBD methods that have been demonstrated to date to localise the nanopore position. (a) Localising breakdown by thinning a region of the membrane. This has previously been demonstrated using a He-FIB or EBL+RIE to thin the membrane. (b) Controlling the nanopore position by confining the electrolyte on one side of the membrane. This has been demonstrated by using a micropipette in contact with the membrane (as shown in the schematic) or microfluidic structures on the membrane surface. (c) Controlling the nanopore position by applying the field via a nanoelectrode. This has been demonstrated using a conductive AFM tip to apply the electric field.

Another technique to control the position of CBD created nanopores is to confine the electrolyte on one side of the membrane. This has previously been done using a micropipette filled with electrolyte to contact the top of the membrane [Fig. 2.3(b)] [146, 181]. Performing CBD by applying the breakdown voltage between the electrolyte in the pipette and a backside reservoir resulted in pore formation localised to the area where the meniscus contacts the membrane (approximately 1μm in diameter). Controlling the pipette position using a micromanipulator enabled the creation of high density arrays of nanopores, thus significantly increasing the number of biosensing experiments that can be performed using a single membrane [146]. The nanopore position can also be controlled by confining the electrolyte using microfluidic structures fabricated on top of the membrane [65].

The last advanced CBD method that has been demonstrated to date relies on localising the electric field by applying the voltage via a nanoelectrode. This has been achieved by applying a large voltage between a conductive atomic force microscope (AFM) tip and a backside electrolyte reservoir [182]. The small diameter of the AFM tip ($\sim$10 nm) enables highly localised positioning of the nanopore. As a result, large electric fields can be applied with a reduced probability of forming multiple pores, thus enabling rapid nanopore fabrication. However, unlike typical CBD which is an *in situ* technique, devices must be

transferred to a setup whereby electrolyte is present on both sides of the membrane to perform sensing experiments.

To date, these techniques have demonstrated limited ability to integrate nanopores with complementary on-chip nanostructures. Methods discussed above that rely on confining the electrolyte on one side of the membrane demonstrate insufficient localisation for this to be possible. In the case of breakdown using an AFM tip or thinning of the membrane using a FIB or EBL+RIE, integration with complementary nanostructures is likely possible. However, this would necessitate time consuming alignment processes that would require significant user input. As discussed in the next section, laser-assisted CBD has been used to self-align nanopores with plasmonic nanostructures. In Chapter 5, I present another promising method to self-align nanopores fabricated via CBD with complementary nanostructures. This technique relies on applying voltages to on-chip electrodes to locally heat the membrane and thereby localise nanopore formation.

2.5 Laser Assisted Controlled Breakdown

Similar to the most commonly used CBD protocol discussed above, laser-assisted controlled breakdown (la-CBD) relies on applying a large electric field across a membrane to induce dielectric breakdown. However, here a laser with power of approximately 5-50 mW is also focused on the membrane resulting in breakdown occurring at the focal point of the laser. As shown in Fig. 2.4, to date there have been three mechanisms that have been suggested by which this can occur. These are: (i) localised thinning due to photochemical etching, (ii) localised heating, and (iii) enhanced electromagnetic field. In general, all of these mechanisms may contribute to breakdown when a laser is focused on the membrane. However, as discussed below, the relative contribution of each mechanism will depend on the experimental conditions such as membrane material, electrolyte composition, laser wavelength, and the presence of any plasmonic nanostructures.

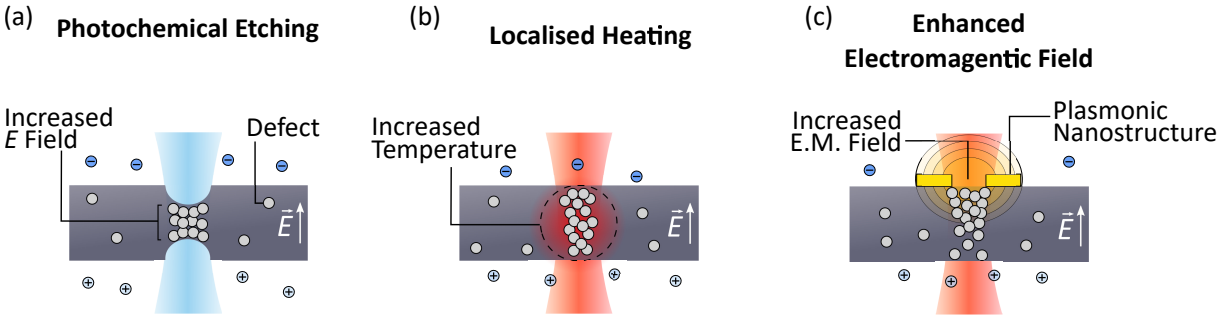


FIGURE 2.4: The three mechanisms that have been proposed by which laser illumination can assist in controlled breakdown. These are: (a) laser etching, (b) localised heating, and (c) enhanced electromagnetic field. Each of these mechanisms may be present in a given la-CBD experiment. However, their relative contributions will depend on the experimental conditions such as laser wavelength, membrane material, electrolyte composition, and the presence of plasmonic nanostructures.

The first of these la-CBD techniques relies on localised thinning of the membrane due to laser induced etching [Fig. 2.4(a)] [138]. Such photochemical etching was described when discussing the laser etching nanopore fabrication technique in Sec. 1.4. This technique relies on illuminating a Si-rich SiN_x membrane with a highly focused blue/green laser to destabilise Si-Si bonds [137]. Performing CBD simultaneous to laser illumination results in breakdown occurring at the focal point of the laser given the membrane is thinnest there. Moreover, by varying the laser power and the applied voltage, it is possible to control the length of the created pore. This is typically challenging to do using other nanopore fabrication techniques and may be desirable depending on the chosen application. For example, ultra-thin membranes are advantageous for polymer sequencing application [183–185]. On the other hand, longer pores may be preferable when analysing the signal from larger, non-linear molecules such as proteins, as changes in the current transient during a translocation event can unveil information on the shape, rotational properties and dipole moment of the molecule [24].

The second la-CBD mechanism relies on localised heating of the membrane [Fig. 2.4(b)]. Here, an infrared laser was used which induces negligible etching of the membrane [169]. It was shown that performing CBD simultaneous to laser illumination results in pore formation at the focal point of the laser. This was attributed to a local increase in the

temperature of the membrane, which lowers the electric field strength required to cause breakdown in SiN_x [148, 186]. Based on the change in nanopore conductance during laser-illumination, the local increase in temperature was estimated to be ∼8°C [169]. The authors also studied the formation of multiple pores by measuring the change in conductance resulting from a self-assembled monolayer. Here, it was demonstrated that continuing to focus the laser on the nanopore during pore expansion significantly decreased the probability of forming multiple pores when the desired diameter is 20-50 nm. It has also been suggested that a local increase in the leakage current through the dielectric resulting from the photoconductivity of SiN_x under laser illumination may lead to localised breakdown [187]. However, in practise, it may be hard to distinguish this effect from la-CBD resulting from localised heating.

The last la-CBD mechanism that has been demonstrated in the literature relies on enhancing the local electromagnetic field to induce breakdown [Fig. 2.4(c)]. This method was demonstrated by fabricating a plasmonic bowtie on a SiN_x membrane [188]. When the plasmonic nanostructure is illuminated by a laser, it creates a highly localised optical hotspot at the centre of the bowtie. By performing CBD simultaneous to laser illumination, it was shown that nanopores form at the centre of the bowtie. This was attributed to an increase in the local electromagnetic field in this region. This method is highly appealing as it creates nanopores that are self-aligned with a plasmonic nanostructure. Indeed, prior to this thesis, this is the only CBD method that has been demonstrated that enables the self-alignment of nanopores with a complementary nanostructure.

2.6 Electrochemical Reactions

Before discussing the results of this thesis, I will lastly introduce the electrochemical reaction (ECR) technique to create nanopores. This technique relies on the same experimental procedure as CBD. In particular, an electric field is applied across the membrane to induce

nanopore formation while the resulting current is monitored as a feedback mechanism. However, ECR is performed on suspended two-dimensional films such as graphene and MoS_2, which is assumed to alter the pore formation mechanism.

The term ECR was first coined is 2015 when using electric fields to create nanopores in a MoS_2 film suspended above an aperture in a SiN_x membrane [189]. Here, the trans-membrane voltage was increased in steps of 100 mV while simultaneously monitoring the resulting current. When the voltage reached 800 mV, an increase in the current was observed indicating nanopore formation. The voltage was then maintained at 800 mV to expand the nanopore until the measured current exceeded a predefined threshold, at which point the voltage was reduced to zero. In this process, nanopore formation was assumed to initiate at a defect in the film and then widen via electrochemical removal of exposed atoms. Removal of atoms was thought to result from the oxidation of MoS_2 to MoO_3 which detaches into solution, however the oxidation of MoS_2 into other valence states was not discounted. Interestingly, step-like increases in the current are observed during ECR suggesting the electrochemical removal of single atoms from the lattice. Studies have demonstrated that the threshold voltage at which pore formation occurs can range between 800-2500 mV and depends on the number of MoS_2 layers, the presence of contamination, and the film quality [190].

Nanopores have also been created in suspended graphene films via ECR [174, 189, 191]. The first demonstration of this [174] utilised voltage pulses with an amplitude of 7 V and a duration of 250 ns to create nanopores. Following pore formation, the pulse amplitude was decreased to 5 V to reduce the probability of forming multiple pores. To better understand the mechanism of pore formation, a recent study used *in situ* atomic force microscopy to image supported graphene films when a large voltage is applied between the graphene and an electrolyte solution [191]. Here, etching of the graphene originating at grain boundaries (which contain defects) was observed. This study also utilised the voltage pulse protocol

described above (albeit with a longer duration of 50 ms) to create nanopores in graphene films suspended across an aperture in a glass chip.

Given the above discussion, it is likely clear that ECR and CBD rely on the same experimental protocol and similar mechanisms. Based on the current descriptions of these two processes, their difference can be understood as follows. As previously discussed, the leakage current during CBD (which drives nanopore formation) is determined by two processes: (i) electrochemical reactions that occur at the membrane interface to inject electrons into the dielectric and, (ii) charge transport across the membrane through defects in the dielectric. For the case of two-dimensional, conductive materials such as graphene and MoS_2, charge transport across the membrane does not limit the pore formation process. Rather, nanopore formation is assumed to proceed as a result of electrochemical reactions that occur at a defect in the membrane. Based on this understanding, it is perhaps useful to think of ECR as a unique case of CBD that arises when scaling down to a two-dimensional membrane whereby charge transport across the dielectric no longer limits nanopore formation. It should be stressed however, that this understanding is based on current descriptions of these processes in the literature. Indeed, there have been few studies on the mechanism of pore formation via ECR to date. Simple studies, such as varying the electrolyte composition during ECR will likely provide more insight into the pore formation process.

2.7 Experimental Setup

I will now introduce the experimental setup used to perform basic CBD and nanopore sensing experiments that I have developed in our laboratory. Variations on this setup will be described in later sections for more advanced CBD experiments. A description of the fabrication of the devices is provided in Appendix A (the steps that were performed by myself are also highlighted here). The device geometry used is shown in Fig. 2.5(a)

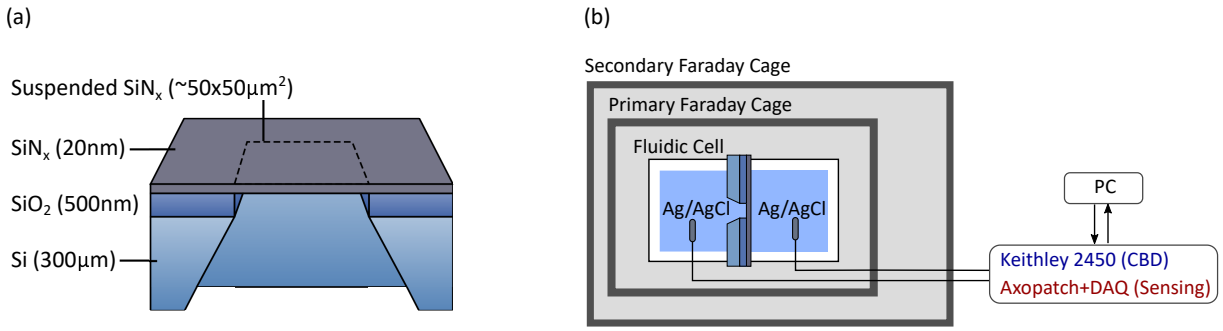


FIGURE 2.5: (a) Schematic of the device geometry used for CBD experiments. (b) Schematic of the experimental setup used for CBD and nanopore sensing experiments. Alterations on the device geometry and experimental setup will be discussed in later chapters when developing new CBD protocols.

and consists of a ∼20 nm thick Si-rich SiN_x membrane suspended on 500 nm of SiO_2 on a 300 μm thick Si substrate.

A schematic of the setup used for standard CBD and nanopore sensing experiments is shown in Fig. 2.5(b). To perform a CBD experiment, devices were first cleaned in warm acetone followed by isopropanol alcohol and dried with N_2 gas. Following this, devices were cleaned in warm (∼80°C) Piranha solution (3:1 ratio of H_2SO_4:H_2O_2) for approximately 10 minutes. Devices were then loaded into a fluidic cell purchased from Nanopore Solutions (more information on this fluidic cell and how to use it can be found here). A drop of ethanol was then placed on either side of the membrane to assist in wetting of the device. The reservoirs on either side of the membrane were flushed with deionised water twice, flushed with the desired buffer once, and then filled with the desired buffer. For CBD experiments, the buffer used was an aqueous solution of 1M KCl, 10 mM Tris and 0.1 mM EDTA at pH 8. Ag/AgCl electrodes (fabricated via electroplating Ag wire from Sigma Aldrich) were inserted into each reservoir and connected to either a Keithley 2450 source meter (for CBD experiments) or an Axopatch 200B (for nanopore sensing experiments). For nanopore sensing experiments, the fluidic cell should be placed inside at least one Faraday cage to reduce electromagnetic noise (this can also be done to reduce the noise in CBD experiments although isn't strictly necessary).

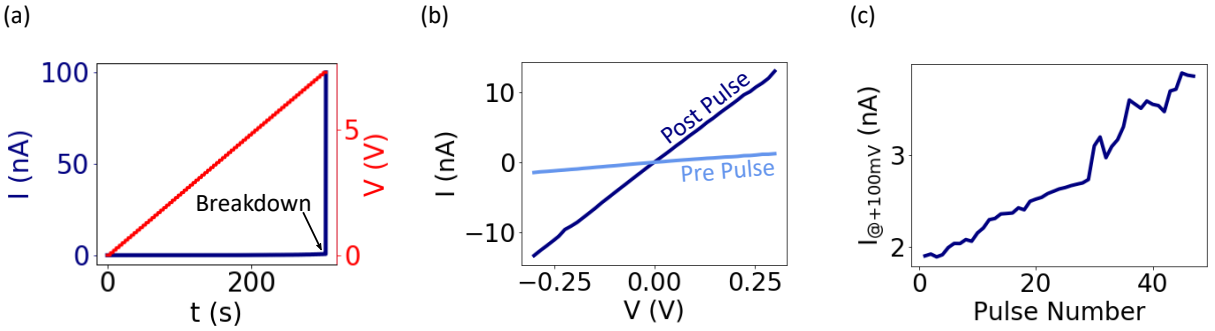


FIGURE 2.6: (a) Example of a typical CBD measurement. (b) Ionic current through a nanopore created via CBD before and after pulsing which was used to increase the pore diameter. (c) Measurement of the ionic current at low bias (100 mV) between voltage pulses that were used to widen a pre-existing nanopore.

2.8 Nanopore Fabrication and Translocation Experiments

To perform a CBD experiment, the applied voltage was ramped up in steps of 100 mV every 4 s while simultaneously recording the resulting current. While ramping the voltage, a small leakage current can be measured due to charge transport through the dielectric (the mechanism of such conduction is discussed in more detail in Chapter 3). The magnitude of the leakage current will depend on the exact device geometry (i.e. SiN_x thickness, area of the suspended membrane, and the presence of dielectric layers to reduce the device capacitance), however, for our devices it is typically a few nanoamps. At some point, a spike in the current will be observed signifying breakdown in the dielectric and nanopore formation. When this occurs, the voltage was quickly reduced to zero to ensure the creation of a small nanopore [Fig. 2.6(a)]. To ensure the voltage was reduced sufficiently fast, the current compliance of the Keithley 2450 is set to 100 nA.

Using these breakdown conditions generally results in the formation of a small nanopore [Fig. 2.6(b)]. To expand the nanopore to the desired size, the buffer solution was first replaced with an aqueous 3.6 M LiCl, 10 mM Tris, 0.1 mM EDTA solution at pH 8. Alternating polarity voltage pulses were then applied across the membrane with a duration of 0.5 s and an amplitude equal to one third of the voltage at which breakdown occurred at

during CBD. The ionic current through the pore at 100 mV was measured between each pulse to enable feedback on the pore size according to Eq. 2.1 [192].

$$d = \frac{1}{2\sigma R}\left(1 + \sqrt{1 + \frac{16\sigma t R}{\pi}}\right) \tag{2.1}$$

where R is the measured resistance, σ is the conductivity of the electrolyte, d is the nanopore diameter, and t is the membrane thickness. When the pore size reaches a predefined threshold the process was stopped [Fig. 2.6(c)]. If the nanopore hasn't expanded to the predefined threshold after 100 pulses, the pulse amplitude can be increased. However, the pulse amplitude should not exceed one half of the voltage at which breakdown occurred at during CBD to avoid the unintentional fabrication of multiple pores.

Pores created in this manner were then used for nanopore sensing experiments. Firstly, the Ag/AgCl electrodes were removed from the Keithley 2450 and connected to an Axopatch 200B. Data from the Axopatch was digitised using a National Instrument data acquisition card (NI PCIe 6321). To begin with, it is necessary to check if the noise characteristics of the fabricated nanopore is suitable for sensing. To do this, a 10 s long current-time (I-t) trace was measured at 200 mV with a sampling frequency of 10 kHz. The noise spectrum between 1-100 Hz was then integrated and normalised by the mean current according according to Eq. 2.2 [139]

$$L = \sqrt{\frac{1}{\overline{I}^2}\int_1^{100} S(f)df} \tag{2.2}$$

where L is a parameter that quantifies the low-frequency noise of the device, $\overline{I}$ is the mean current, and $S(f)$ is the noise spectrum. If L is below $1\text{x}10^{-2}$, the nanopore should be usable for single-molecule biosensing experiments. If this is not the case, it may be necessary to return to the pore expansion phase to widen the pore. Alternatively, the

pore can be left in 3.6 M LiCl overnight to help it stabilise. In some cases, the noise may not be sufficiently reduced and another nanopore may need to be fabricated.

To demonstrate the utility of these nanopores for single-molecule biosensing applications, I have performed translocation of 1 kbp double-stranded DNA (dsDNA) through a pore (NoLimits 1000 bp DNA from ThermoFisher). The diameter of the nanopore used was ∼12.3 nm as estimated from Eq. 2.1. To perform translocation experiments, the solution in the *cis* chamber was 'spiked' with a small, concentrated volume of DNA. The solution was then mixed by pipetting (being careful not to introduce any air bubbles) resulting in a final DNA concentration of ∼5 nM. When a positive voltage was applied to the *trans* chamber, transient drops in the current (typically referred to as blockades) are observed consistent with DNA being electrophoretically drawn into and through the pore

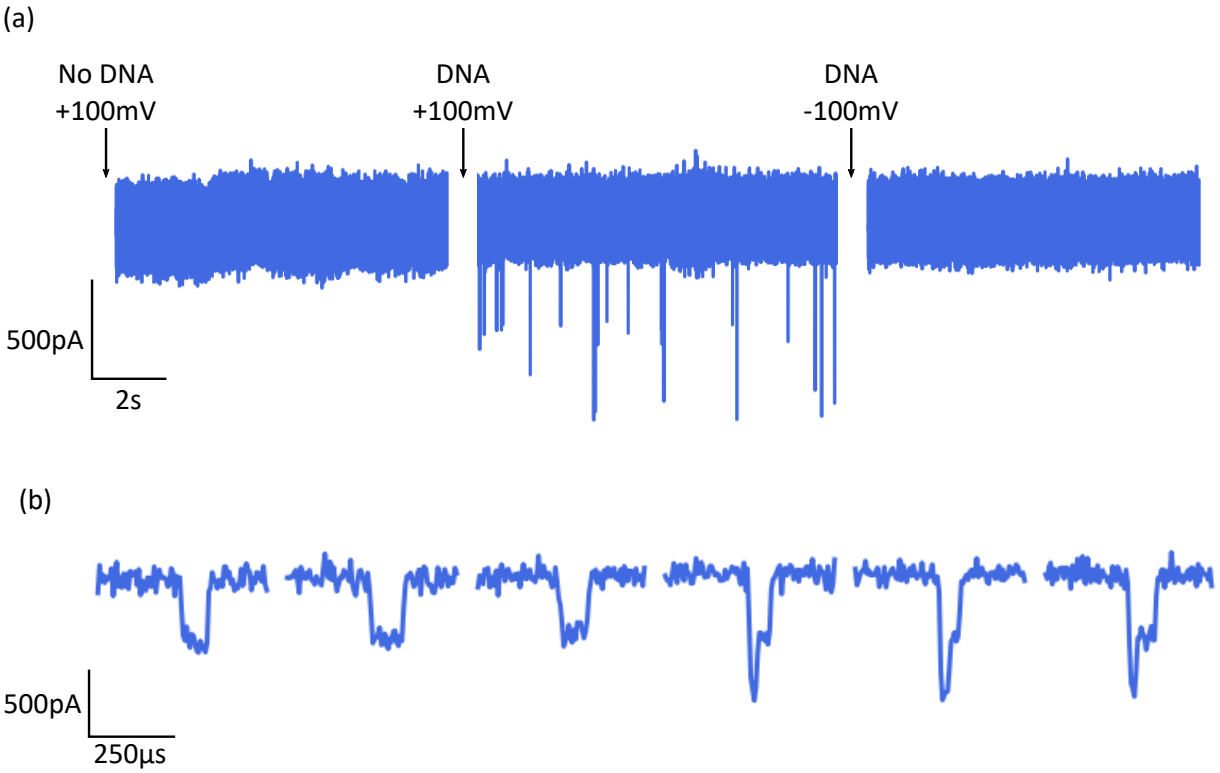


FIGURE 2.7: (a) Example of translocation of 1000 bp dsDNA through a nanopore. Measurements were taken in 3.6 M LiCl with a DNA concentration of 5 nM. The measurement taken at -100 mV has been offset to align with the other traces. (b) Zoom of several translocation events showing the translocation of DNA in an unfolded (left) and folded manner (right).

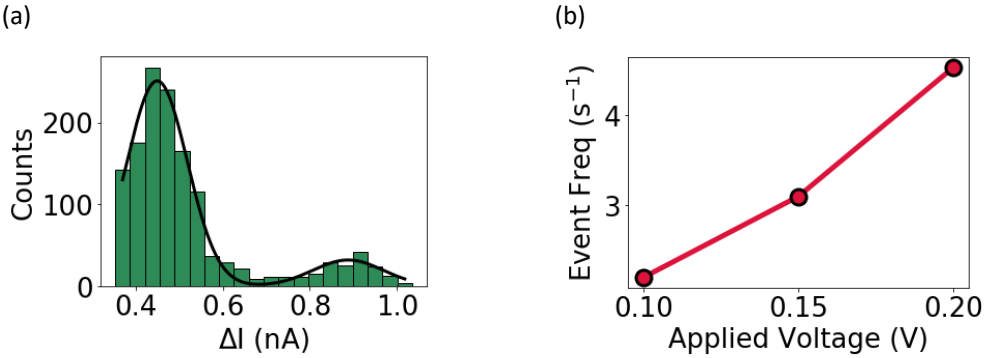


FIGURE 2.8: (a) Histogram of the current blockade during DNA translocation. (b) Frequency of translocation events as a function of applied voltage. Measurements were performed using a 12.3 nm pore in 3.6 M LiCl to detect 1000 bp dsDNA.

[Fig. 2.7(a)]. Such current transients were not observed before DNA was injected into the *cis* chamber, or when a negative voltage was applied to the *trans* chamber [Fig. 2.7(a)].

Upon closer inspection, the current transients can be categorised into two cases. These are: (i) single-level current blockades, and (ii) two-level current blockades [Fig. 2.7(b)]. This is typical of dsDNA translocation through nanopores with a diameter at least twice as large as the cross section of dsDNA (approximately 2.3 nm). Single-level and two-level current blockades correspond to the translocation of DNA in an unfolded and folded manner respectively [193]. The presence of two distinct current blockade levels can also be seen in Fig. 2.8(a) which shows a histogram of the current blockade during the translocation events. Two peaks in the histogram are observed. Fitting a bimodal Gaussian distribution to the histogram (black curve) gives a current blockade of 0.45 nA for the peak corresponding to the translocation of unfolded DNA and 0.89 nA for the peak corresponding to the translocation of folded DNA. The current blockade for folded DNA translocation is approximately twice that of unfolded DNA since the area of the pore which is blocked is doubled.

Figure 2.8(b) shows the frequency of DNA translocation events as a function of the applied voltage. The event frequency increases approximately linearly with the applied voltage. This implies that the rate of DNA translocation is limited by diffusion of the analyte to within the capture volume of the nanopore [193, 194]. Inside the capture volume,

electrophoretic forces act to draw DNA through the nanopore. This is consistent with previous studies for solid-state nanopores of similar geometry [195]. The above results confirm the ability to fabricate solid-state nanopores that can be used for single-molecule biosensing applications using the CBD setup that I have built in our laboratory.

Chapter 3

Understanding Electrical Conduction and Nanopore Formation During Controlled Breakdown

In this chapter I will discuss the mechanism by which electrical conduction and nanopore formation occurs during CBD. It will be shown that depending on the SiN_x stoichiometry, conduction is limited by either oxidation reactions that must occur at the membrane-electrolyte interface (Si-rich SiN_x) or charge transport across the dielectric (stoichiometric Si_3N_4). I will discuss several important practical implications resulting from understanding this process, particularly when performing CBD on devices with electrodes on the membrane surface. I also demonstrate results consistent with charge accumulation in the dielectric during CBD. It is proposed that this charge accumulation may explain the rectification in ionic current often observed in nanopores directly after CBD.

A paper containing the results shown in this chapter has been submitted to Small and uploaded to arXiv [196].

3.1 Motivation

As described in Chapter 2, CBD is a highly appealing technique to create solid-state nanopores. However, despite the success of this method, the mechanism by which nanopores are formed during this process has remained largely unexplored. Nanopore formation is generally assumed to proceed via a similar mechanism to dielectric breakdown in metal-insulator and semiconductor microelectronic devices [147]. In particular, electric fields on the order of (0.1-1 V/nm) activate conduction through charge traps in the dielectric. At some point, these charge traps form a percolation path which results in an abrupt increase in the current and dielectric breakdown, likely due to Joule heating [147]. However, for the case of CBD where the electric field is applied via an electrolyte solution, the process is more complex. In this case, electrochemical (redox) reactions must occur at the membrane-electrolyte interface to inject/remove electrons from the dielectric. The importance of such redox reactions has been raised in previous studies where it was shown that the pH of the electrolyte solution affects the voltage at which breakdown occurs [140, 147, 173, 197]. Gas formation at the membrane interface resulting from redox reactions has also been observed during CBD [175]. However, to date, a detailed description of electrical conduction across a dielectric during CBD has not been provided. Understanding this process will be an important step in further developing CBD in the coming years, for example to fabricate nanopores in different membrane materials or integrated with on-chip nanostructures.

3.2 Device Geometry and Experimental Setup

The same suspended SiN_x device geometry shown in Sec. 2.7 is used here [Fig. 2.5(a)]. Namely, the devices consist of a SiN_x membrane suspended above 500 nm of SiO_2 on a 300 μm thick Si substrate. The SiO_2 layer is typically present in nanopore devices to reduce the capacitance and therefore the high frequency noise [58, 63]. For the experiments

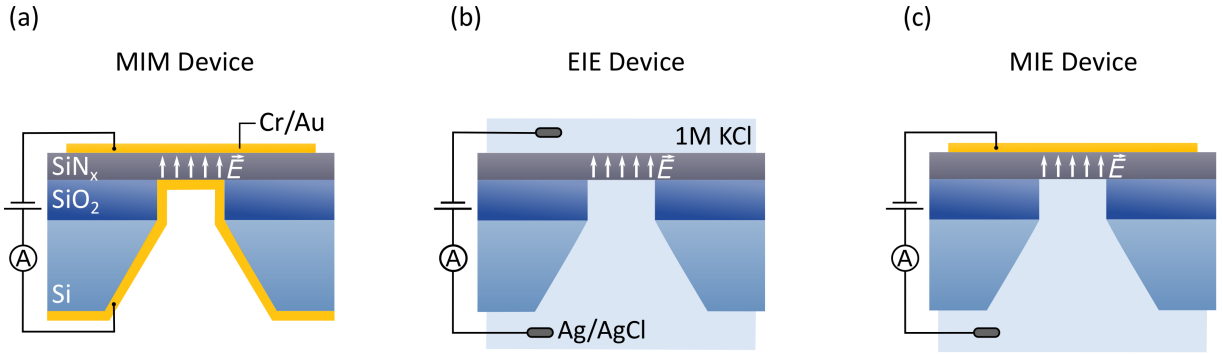


FIGURE 3.1: Schematics of the three device geometries predominately considered in this chapter. (a) Metal-insulator-metal (MIM) devices where the voltage is applied via Cr/Au electrodes deposited on either side of the membrane. (b) Electrolyte-insulator-electrolyte (EIE) devices where the voltage is applied via electrolyte solutions on either side of the membrane. (c) Metal-insulator-electrolyte (MIE) devices where the voltage is applied via a metal electrode on one side of the membrane and an electrolyte solution on the other side of the membrane.

discussed in this chapter, this layer also has the advantage that it ensures the leakage current is only through the suspended region of SiN_x. Without this layer, charge could be transported from the electrolyte solution, to the Si substrate, and through the SiN_x [147, 197]. Unless noted otherwise, the results discussed in this chapter are for a 25 nm thick Si-rich SiN_x membrane with a nitrogen to silicon ratio of N:Si$\equiv x\equiv$1.14. The stoichiometry was estimated from the measured refractive index of the film [137]. The thickness of the film was estimated from ellipsometry. A detailed description of the fabrication of these devices is given in Appendix A.

To understand the mechanism of electrical conduction and nanopore formation during CBD, I have studied three device geometries. These are shown in Fig. 3.1. In the first geometry, the voltage was applied via metal electrodes (5/45 nm Cr/Au) deposited on either side of the membrane [Fig. 3.1(a)]. Similar device geometries have been studied by the microelectronics community for several decades [149]. These devices will be referred to as metal-insulator-metal (MIM). Next, the voltage was applied via electrolyte solutions (1 M KCl with 10 mM Tris and 0.1 mM EDTA at pH 8) on either side of the membrane using Ag/AgCl electrodes [Fig. 3.1(b)]. This is the typical measurement setup for CBD [139, 140]. These devices will be referred to as electrolyte-insulator-electrolyte (EIE).

Lastly, the voltage was applied between a metal electrode on the membrane surface and an electrolyte solution on the other side of the membrane [Fig. 3.1(c)]. These devices will be referred to as metal-insulator-electrolyte (MIE). Devices from the same wafer were used when comparing between the three cases to reduce variability resulting from the fabrication process. Namely, electrodes were deposited on a subset of devices from a given wafer to make the MIM and MIE devices.

To perform measurements on the EIE devices, the same procedure as discussed in Sec. 2.8 to perform CBD was used. To perform the MIM experiments, one side of the device was glued to a contact pad on a homemade printed circuit board (PCB) using silver paste. The electrode on the other side of the membrane was then wire-bonded to another contact pad on the PCB. For measurements on the MIE devices, the metal electrode was wire-bonded to a contact pad on a PCB. The PCB was then loaded into a custom-made fluidic cell (more details on this fluidic cell are given in Sec. 4.2) and the reservoir filled with 1 M KCl, 10 mM Tris, 0.1 mM EDTA buffer solution at pH 8. A Ag/AgCl electrode was then inserted into this reservoir. The same voltage ramp protocol was used to measure electrical conduction and breakdown in all device geometries. Namely, a voltage ramp increasing in steps of 100 mV every 4 s was applied across the membrane while simultaneously measuring the resulting current.

3.3 Electron Transport in Silicon Nitride

It is first useful to discuss the case of conduction across SiN_x when the electric field is applied via metal electrodes on the membrane surface [Fig. 3.1(a)]. For such a device geometry, the measured current is limited by electron transport processes across the dielectric. Such electron transport processes across thin SiN_x films have been well studied and are often attributed to Poole-Frenkel (PF) emission [148–150, 186]. This electron transport process results from lowering of the barrier height between trapped electrons

and the conduction band when applying electric fields across the dielectric. Lowering of this barrier height increases the probability of trapped electrons being thermally excited to the conduction band, where they briefly transit the membrane before being returned to a localised state. The current density resulting from PF emission can be calculated as [149]:

$$J(E,T) = C_1 E e^{-q(\Phi_B - \sqrt{qE/\pi\epsilon_D})/k_B T} \tag{3.1}$$

where q is the electron charge, k_B is Boltzmann's constant, T is the temperature in Kelvin, E is the electric field, ϵ_D is the optical (dynamic) dielectric constant, Φ_B is the charge trap depth, and C_1 is a constant that is determined by the charge trap density and the carrier mobility. The optical dielectric constant can be estimated by $\epsilon_D \sim n^2$ where n is the refractive index of the film [198]. Following Eq. 3.1, if PF emission is the dominant conduction mechanism a plot of $\ln(J/E)$ vs $E^{1/2}$ should be linear. Such a plot is commonly used to study conduction in dielectric films and is referred to as a PF plot.

Figure 3.2(a) shows a typical plot of current as a function of applied voltage for a MIM device. An exponential increase in the current is observed followed by an abrupt spike that indicates dielectric breakdown of the SiN_x. Figure 3.2(b) shows the same data plotted as a PF plot. The PF plot shows a linear behaviour. Moreover, consistent with Eq. 3.1 an increase in conduction is also observed with increasing temperature [Fig. 3.2(c)-(d)]. Note that, each measurement comparing conduction at a different temperature was performed on a new device (i.e. one that hadn't been previously exposed to electric fields). This is necessary to avoid discrepancies resulting from space charge effects as discussed below.

The above results point towards PF emission as the dominant electron transport mechanism. However, it is emphasised that the above results do not guarantee that conduction can be explained solely as a result of PF emission as given by Eq. 3.1. For this to be confirmed, it is necessary to extract ϵ_D from the slope of the PF plot and confirm that this

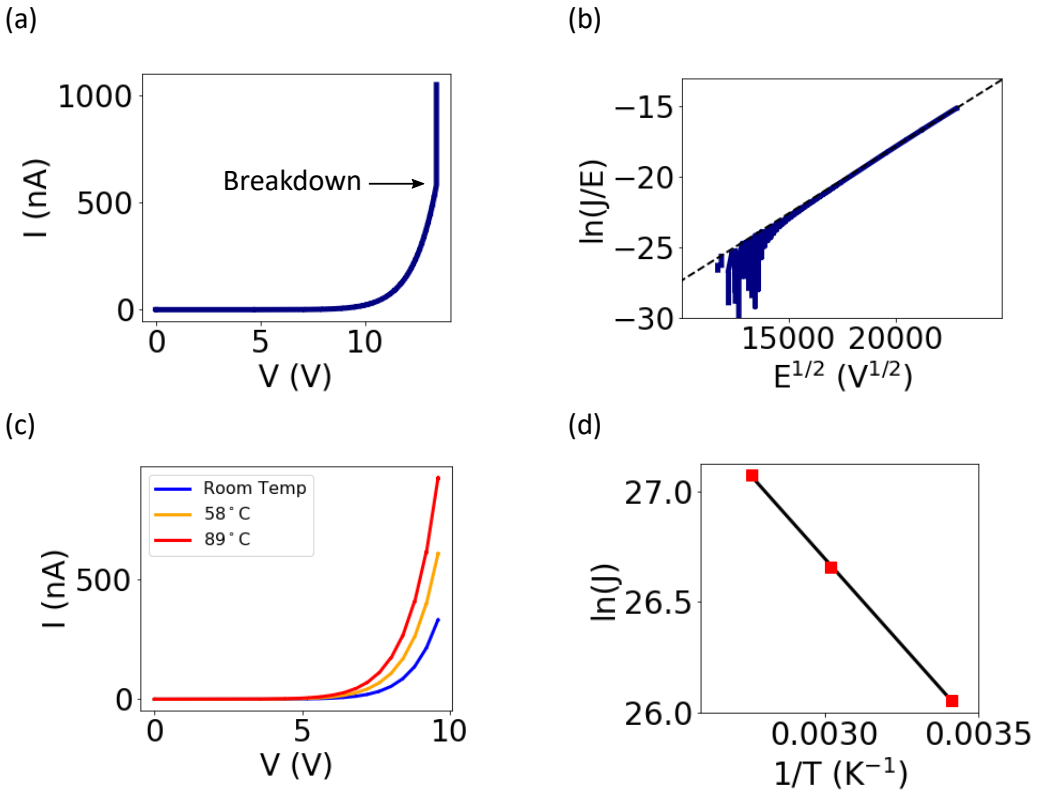


FIGURE 3.2: (a) Measured current as a function of voltage for a MIM device. (b) Shows the same data as (a), however it is plotted as a Poole-Frenkel (PF) plot. (c) Current as a function of voltage for three different membrane temperatures. (d) Current density shown in (c) extracted at an applied voltage of 9.6 V as a function of the inverse of temperature.

is comparable to the value expected from the refractive index of the film [149, 199, 200]. I have extracted ϵ_D from Fig. 3.2(b) (black dashed line) and obtained a value of 10.26. This is significantly higher than the expected value based on the refractive index of the film ($\epsilon_D \approx n^2 = 4.57$).

Previous studies have often reported that despite conduction showing a linear trend on a PF plot, the extracted value of ϵ_D does not match the expected value [200–203]. In many of these studies, it was demonstrated that space charge effects resulting from the trapping of injected charge can significantly alter the conduction characteristics [201–203]. Such trapping results in a non-uniform charge distribution across the membrane which modifies the electric field. This generally results in slow changes in the measured current as a function of time as the trapped charges accumulate in the dielectric. Consistent with

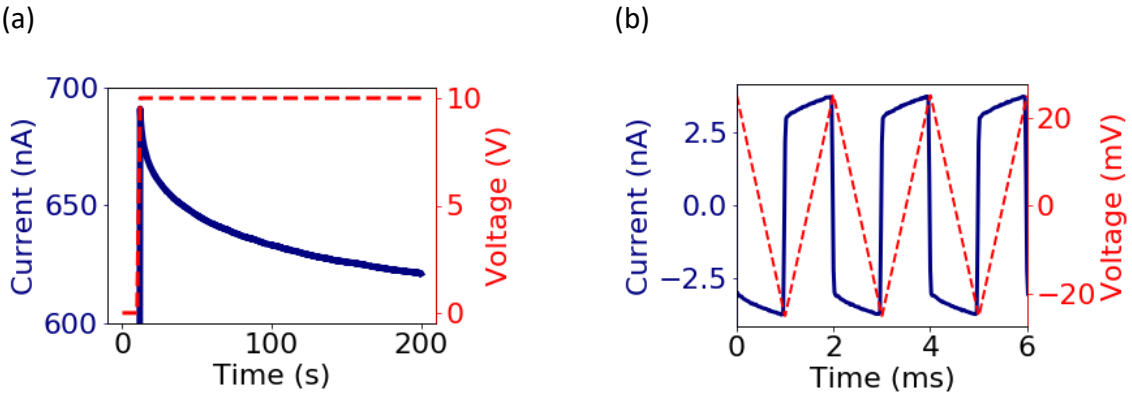


FIGURE 3.3: (a) Measured current across a MIM device as a function of time after changing the applied voltage from 0 V to 10 V. The decay constant is τ ~43.2 s. (b) Measured current when applying a triangular wave voltage (f=500 Hz V_{PP}=50 mV). The extracted capacitance from these measurements is ~70 pF.

this, I have observed slow changes in the current upon changing the applied voltage (time constant of $\tau \approx 43.2$ s) in these devices [Fig. 3.3(a)].

To compare these slow changes in current to the expected RC time constant, I have measured the capacitance of these devices. This was done by applying a triangular wave voltage across the membrane (f=500 Hz V_{PP}=50 mV) and measuring the resulting current [Fig. 3.3(b)]. The capacitance can then be calculated as $C = I(dV/dt)^{-1}$. By doing this, a capacitance of 70 pF was obtained. Assuming a resistance of the leads of 100 Ω, the estimated RC time constant is ~70 ns. This is much smaller than the observed decay constant in the measured current. This result suggests that significant space-charge effects are present in these devices when a large voltage is applied across the membrane. Electron transport in SiN_x films is clearly a complex phenomenon that is determined by several processes as well as the details of the film being studied (e.g. thickness and stoichiometry). A detailed study of this is beyond the scope of this work, however the above results indicate that PF emission and space charge effects play an important role in determining the conduction in these SiN_x membranes.

3.4 Redox Reactions at the Membrane-Electrolyte Interface

I will now discuss conduction and breakdown in SiN_x membranes when the electric field is applied via electrolyte solutions on either side of the membrane. For this device geometry, in addition to electron transport across the dielectric, electron transfer (redox) reactions must also occur at the membrane-electrolyte interface for a current to be measured. Previous studies have postulated that the oxidation of Cl^- and OH^- and the reduction of H^+ are the dominant redox reactions that occur at the membrane-electrolyte interface for CBD in an aqueous KCl solution [175, 197].

Figure 3.4 shows a typical measurement for electrical conduction and breakdown in an EIE device (i.e. a CBD experiment). The current through a MIM device [as shown in Fig. 3.2(a)] is also shown for comparison. Note that due to the reduced y-scale, the breakdown event in the MIM device cannot be observed in Fig. 3.4. Instead, the voltage at which breakdown occurs in the MIM device is shown by the vertical dashed line. There is a significant reduction in the measured current for the EIE device. Moreover, a larger voltage must be applied to induce breakdown in the EIE device. These results highlight the importance of redox reactions that must occur at the membrane-electrolyte interface for current to flow in the EIE device. In particular, these redox reactions limit the amount of current transported across the membrane resulting in a larger voltage being required to induce breakdown. Previous studies have pointed out that such redox reactions must be present for a current to flow during CBD [140, 175, 197]. However, until now, it has not been demonstrated that these reactions are the limiting process for conduction during CBD.

To better understand these redox reactions, I have measured conduction and breakdown in devices when the electric field is applied between a metal electrode on one side of the membrane and an electrolyte solution on the other side [i.e. MIE device in Fig. 3.1(c)].

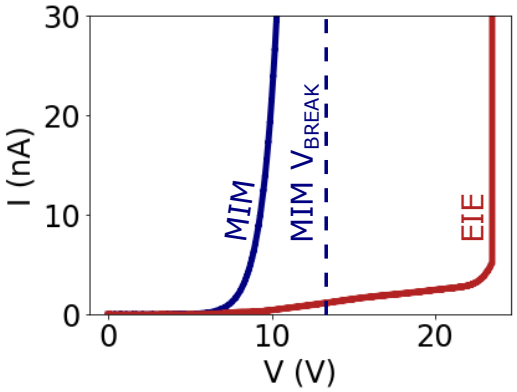


FIGURE 3.4: Conduction and breakdown in an EIE device (maroon curve). Conduction in a MIM device [from Fig. 3.2(a)] is also shown for comparison (navy curve). The voltage at which the MIM device undergoes breakdown is shown by the vertical dashed line.

The asymmetry of this device geometry allows contributions from oxidation and reduction reactions occurring on either side of the membrane to be isolated by changing the direction of the applied field. Grounding the metal electrode and applying a positive bias to the electrolyte solution results in the electric field direction shown in Fig. 3.5(a)(i). I will refer to this as the forward-biased configuration. Reversing the electric field direction by applying a positive voltage to the metal electrode and grounding the electrolyte solution will be referred to as the reverse-biased configuration [Fig. 3.5(b)(i)].

Figure 3.5(a)(ii) shows a PF plot comparing conduction in MIM, EIE, and MIE devices for the forward-biased configuration. Conduction in the MIE device shows a similar behaviour to the MIM device with a linear trend on the PF plot. However, when the direction of the electric field is reversed, the opposite behaviour is observed [Fig. 3.5(b)(ii)]. In particular, conduction in the MIE device now follows a similar behaviour to the EIE device showing a distinctly non-linear trend on the PF plot. As expected, the conduction behaviour of the MIM and EIE devices do not change significantly depending on the direction of the applied electric field given their symmetry.

The change in conduction behaviour of the MIE device depending on the direction of the applied field provides insight into which redox reaction limits the conduction. For

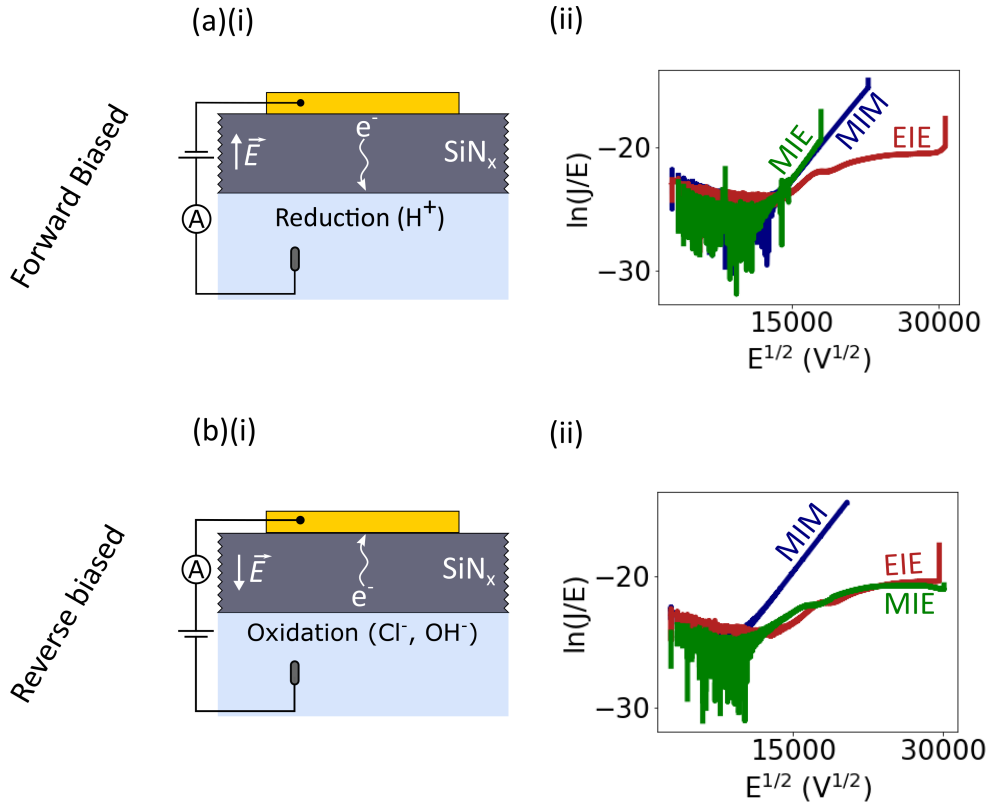


FIGURE 3.5: Conduction and breakdown characteristics in asymmetric MIE devices. (a)(i) Schematic of the forward-biased configuration and (ii) PF plot showing conductance and breakdown in MIM, EIE, and MIE devices in the forward-biased configuration. (b)(i) Schematic of the reversed biased configuration and (ii) PF plot showing conductance and breakdown in MIM, EIE, and MIE devices in the reverse-biased configuration.

the forward-biased case, an oxidation reaction does not need to occur as electrons can be injected into the SiN_x from the metal electrode. However, a reduction reaction must still occur to remove electrons from the membrane [Fig. 3.5(a)(i)]. This results in a relatively large conduction through the membrane. For the reverse-biased case, an oxidation reaction must occur to inject electrons into the SiN_x. However, a reduction reaction does not need to occur as electrons can be removed via the metal electrode [Fig. 3.5(b)(i)]. This results in a reduced conduction through the membrane. As such, it is concluded that oxidation reactions limit the conduction across the membrane.

It is also highlighted that, for the forward-biased configuration, MIE devices breakdown at a much lower voltage (and therefore current) than MIM devices [Fig. 3.5(a)(ii)]. For instance, for the devices shown in Fig. 3.5(a)(ii), the MIE device undergoes breakdown at

8.1 V (30 nA) compared to 13 V (613 nA) for the MIM device. Although the reason for this is currently not clear, it suggests that for membranes exposed to an electrolyte, breakdown is not solely driven by the leakage current across the membrane as is typically assumed to be the case. Measuring conduction and breakdown in MIE devices as a function of electrolyte composition (e.g. pH) may provide further insight into the mechanism of nanopore formation during CBD. This would be an interesting area to explore in future studies.

3.5 CBD with Microelectrodes on the Membrane Surface

To further highlight how oxidation reactions affect nanopore formation during CBD, I have performed breakdown on devices with metal microelectrodes on the membrane surface. In contrast to the MIE devices considered in the previous section, for these experiments a typical CBD configuration was used (i.e. electrolyte present on both sides of the membrane and the voltage is applied via Ag/AgCl electrodes immersed in each reservoir). A schematic of this experimental setup is shown in Fig. 3.6(a). A false-colour scanning electron micrograph of the electrode configuration over the suspended region of SiN_x is shown in the inset of Fig. 3.6(a) (these devices were repurposed from other experiments, however, the exact electrode geometry is not important). These experiments were performed by wire-bonding the device electrodes to a printed circuit board which then fits into a custom-made fluidic cell (described in more detail in Sec. 4.2). This enables control over the voltage applied to the on-chip electrodes as well as to the Ag/AgCl electrodes in each reservoir. To avoid delamination of the electrodes, the voltage of the on-chip electrodes and the voltage of the electrolyte solution in contact with the on-chip electrodes were held at ground. The forward (reverse) biased configuration was then achieved by applying a

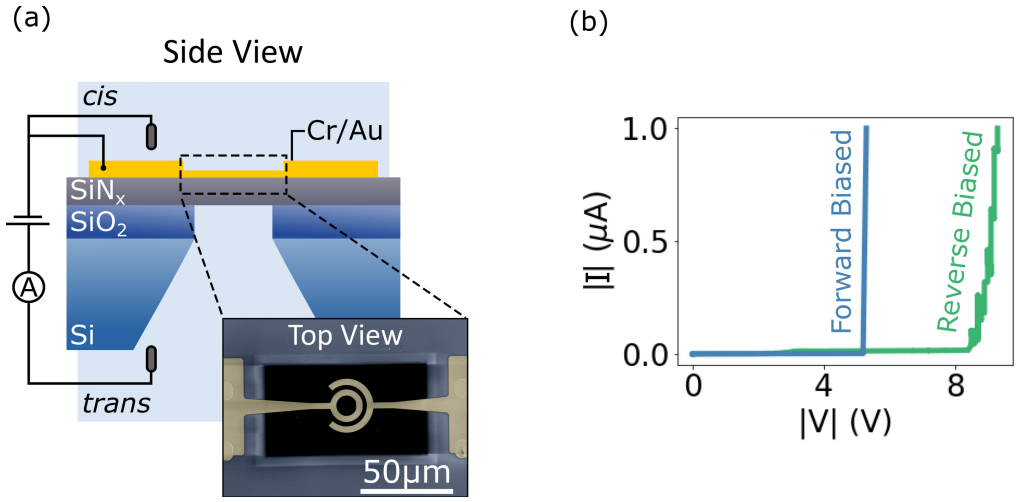


FIGURE 3.6: (a) Schematic of the experimental setup used for CBD experiments with microelectrodes on the membrane surface. Electrodes on the membrane surface and the Ag/AgCl electrode in the *cis* chamber are held at ground. The forward (reverse) biased configuration are obtained by applying a positive (negative) voltage to the Ag/AgCl electrode in the *trans* chamber. The inset shows a false-colour scanning electron micrograph of the electrode configuration over the suspended region of SiN_x. (b) Typical CBD curves for devices with microelectrodes on the membrane surface for the forward and reverse-biased configurations.

positive (negative) voltage to the electrolyte solution in contact with the other side of the membrane.

Figure 3.6(b) shows typical CBD measurements for this device in the forward and reverse-biased configurations. It is observed that the device in the forward-biased configuration undergoes breakdown at a significantly lower voltage. This is consistent with the results in the previous section for MIE devices. In particular, for the forward-biased configuration, electrons can be supplied to the SiN_x from the electrodes on the membrane surface. As such, oxidation reactions do not need to occur at the membrane-electrolyte interface in this region. This results in breakdown occurring at a lower voltage. Following this, one would expect nanopores to form only within the area covered by the electrodes for the forward-biased configuration.

To determine the position of the nanopores formed during CBD, fluorescence microscopy with Ca^{2+} and Ca^{2+} indicators was performed. To do this, devices were cleaned in DI water, followed by acetone and O_2 plasma etching. Prior to measurement, the devices were

again cleaned via UV-ozone treatment. The devices were then loaded into a custom-built device holder that was mounted in an inverted microscope. For fluorescence imaging, a similar process to that previously described was used [95, 96, 171]. Namely, the device was illuminated by a fibre-coupled 488 nm tunable Argon ion laser. A 498 nm dichroic mirror reflected the incoming light towards the sample where a 60x objective was used to illuminate the sample and collect the emitted fluorescence. The *cis* and *trans* chambers were filled with $CaCl_2$ solution (50 μM $CaCl_2$, 100 mM KCl in DI water) and Fluo-4 solution (5 μM Fluo-4, 100 mM KCl in DI water) respectively. Ag/AgCl electrodes were inserted into each chamber and a negative voltage applied to the *trans* chamber to drive Ca^{2+} ions through the nanopore. Transport of Ca^{2+} ions into the *trans* chamber activates the Ca^{2+} dependent Fluo-4 resulting in a highly localised fluorescence hotspot at the nanopore which was recorded by an electron multiplying charge coupled device.

Figure 3.7 shows several fluorescence micrographs of the position of nanopores formed during CBD for each electric field direction. The white dashed box represents the edge of the suspended region of SiN_x. The solid white lines depict the position of the electrodes on the membrane surface. For each chip, three micrographs are shown depicting a time series of data with a frame before, during, and after the application of a voltage that drives Ca^{2+} ions through the nanopore. For the forward-biased configuration, it is observed that nanopores only form within the area covered by the electrodes on the membrane surface. However, for the reverse-biased configuration the nanopores form at random positions in the membrane. These results are consistent with those discussed above. Namely, for the forward-biased configuration, electrodes on the membrane surface can supply electrons to the SiN_x. Therefore, an oxidation reaction does not need to take place here, thus resulting in breakdown occurring at a lower voltage in these regions. As a result, nanopores form only within the area covered by the electrodes on the membrane surface. For the reverse-biased configuration, an oxidation reaction must occur to inject electrons into the membrane (it is the reduction reaction that does not need to occur within the electrodes).

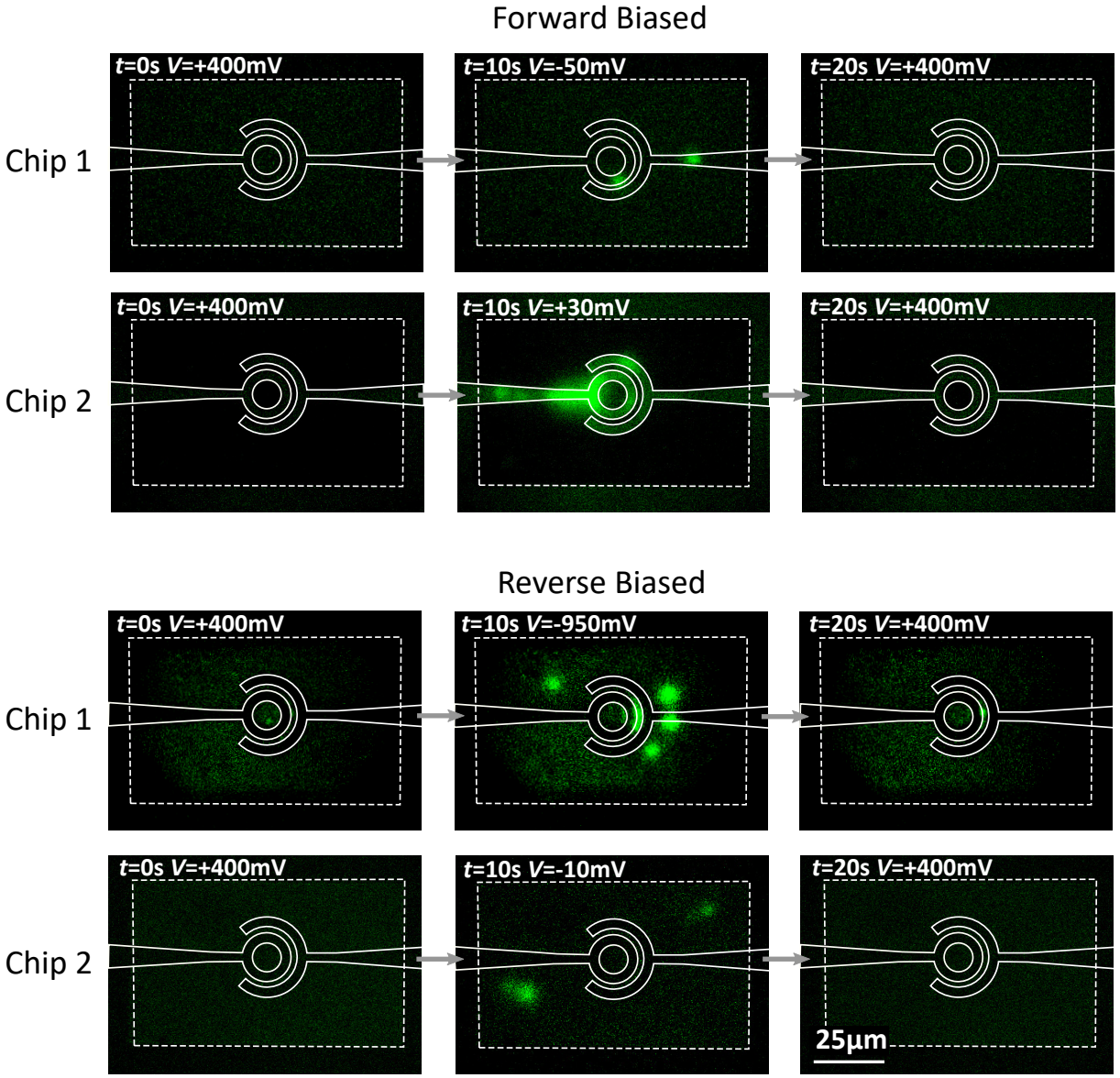


FIGURE 3.7: Fluorescence images of the position of nanopores formed during CBD for devices with microelectrodes on the membrane surface in the forward-biased configuration (top panels) and reverse-biased configuration (bottom-panels). The dashed white box shows the edges of the suspended region of SiN_x. The solid white lines show the position of the electrodes. A time series of images are shown for each device (left to right) with a frame before, during, and after the application of a voltage that drives Ca^{2+} ions through the nanopore.

As such, the nanopores form at random locations in the membrane. For these measurements the voltage was intentionally not reduced immediately following breakdown which resulted in the creation of multiple pores in the membrane. This enabled more statistics on the resulting nanopore position to be obtained from a single device. These fluorescence imaging results indicate that the created nanopores likely extend through the metal electrode. Indeed, this is confirmed via TEM imaging and biomolecular sensing experiments discussed below. This is consistent with previous studies where it was postulated that electrochemical etching of the metal immediately after breakdown results in a nanopore which extends through the SiN_x/metal stack [162].

These results are of practical importance for nanopore fabrication via CBD when micro/-nanostructures are on the membrane surface. Nanopores integrated with complementary on-chip nanostructures have received interest in recent years as they have the ability to overcome issues associated with ionic current based sensing including limited device densities [21, 64] and low bandwidth [21, 60, 64, 66, 120]. To date, the development of these devices has been limited by the difficult fabrication processes that are required to integrate pores with on-chip nanostructures [64, 75]. Developing CBD techniques to self-align nanopores with on-chip nanostructures is a promising way to overcome many of these issues. The results discussed in this chapter are promising as they demonstrate that nanopores can be localised to on-chip electrodes simply by applying the appropriate polarity electric field during CBD. These results will be built upon in later chapters where I will demonstrate that Joule heating from on-chip electrodes can be used to localise pore formation to a specific location in an electrode. It is also highlighted that the expansion of nanopores following CBD is commonly performed using voltage pulses of alternating polarity [139, 152]. The significant difference in the breakdown voltage, depending on the electric field direction, will therefore need to be taken into account when performing pore expansion on devices with electrodes on the membrane surface to avoid the unintentional formation of multiple pores.

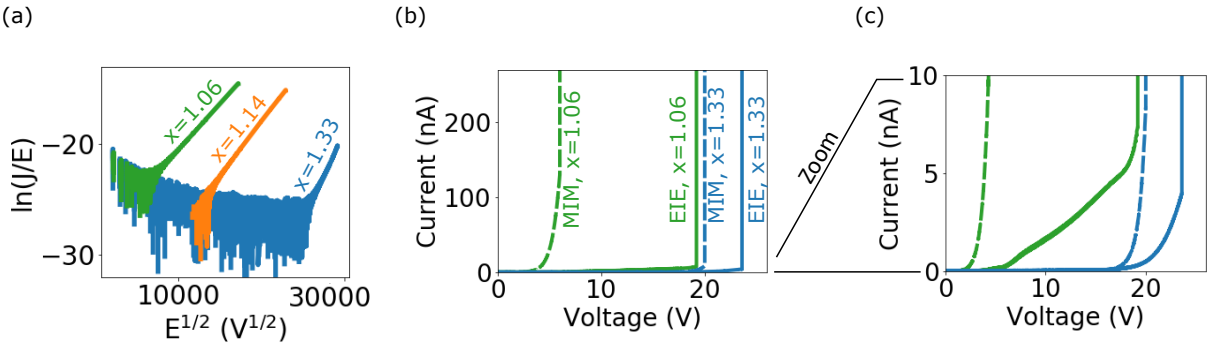


FIGURE 3.8: (a) Conduction in MIM devices for three different membrane stoichiometries. (b) Comparison of conduction and breakdown in MIM and EIE devices for two different membrane stoichiometries. (c) Shows a zoom in of (b) at low currents so the conduction behaviour of EIE devices can be observed.

3.6 Varying the Membrane Stoichiometry

I will now discuss how the stoichiometry of the SiN_x membrane affects conduction and breakdown during CBD. Typically, solid-state nanopore experiments have been performed using Si-rich SiN_x membranes. This is due to the low intrinsic stress of these films which results in superior mechanical strength compared to stoichiometric SiN_x membranes [41, 204]. That said, some nanopore studies have utilised stoichiometric SiN_x films [105, 172, 173]. Other dielectrics such as HfO_2 are also becoming increasingly popular for solid-state nanopore measurements [45, 117].

It is known from studies within the microelectronics community that electron transport in SiN_x is affected by the film stoichiometry. In particular, it has been demonstrated that increasing the Si content of the SiN_x results in an increased electrical conductivity [150]. This was thought to result from the decreased bond strain in Si-rich films which reduces the energy required to excite trapped electrons to the conduction band [150]. This results in a lower electric field strength required to induce PF emission in Si-rich SiN_x. I have measured conduction in MIM devices for three different SiN_x stoichiometries [Fig. 3.8(a)]. Consistent with the literature, an increased conduction with increasing Si content is observed.

Given the above results, one may expect that the stoichiometry of the SiN_x membrane also affects breakdown during CBD. I have measured conduction and breakdown in EIE devices for SiN_x membranes of different stoichiometries. Figure 3.8(b) shows a comparison of conduction and breakdown in MIM and EIE devices for membranes with a N:Si ratio of x=1.06 (Si-rich) and x=1.33 (stoichiometric). As previously discussed, for Si-rich SiN_x membranes the EIE device shows significantly less conduction and undergoes breakdown at a much larger voltage than the MIM device. This is a result of oxidation reactions limiting the conduction across the membrane. However, this is no longer the case for the stoichiometric SiN_x. Here, the MIM and EIE devices show comparable levels of conduction with the EIE device undergoing breakdown at only a slightly higher voltage. This results from the reduced electron transport through stoichiometric SiN_x as discussed above. As a result, it is the electron transport across the dielectric (rather than oxidation reactions at the membrane interface) that predominately limit conduction for these membranes.

The different conduction behaviour depending on the membrane stoichiometry is also highlighted in Fig. 3.8(c). This plot shows the same data as Fig. 3.8(b) with a reduced y-scale to enable visualisation of the conduction behaviour prior to breakdown in the EIE devices. For the Si-rich SiN_x, a leakage current can be measured at low voltages ($\sim$5 V) since electron transport through these devices begins at low electric fields. The leakage current then increases slowly (approximately linearly) until breakdown since the conduction is limited by oxidation reactions at the membrane interface. In contrast, for the stoichiometric membrane, a leakage current cannot be measured until large voltages are applied ($\sim$17 V). This is because of the reduced electron transport in this dielectric which results in negligible conduction up to large electric fields. After the onset of conduction, the current increases approximately exponentially until breakdown (albeit at a slower rate than the MIM device since oxidation reactions still limit the current to some extent). These results highlight the material dependent nature of the conduction and nanopore formation processes during CBD. As such, these results may be of interest as this technique

is further developed to fabricate nanopores via CBD in previously unexplored material systems.

3.7 Charge Accumulation in the Membrane

It has already been discussed that previous studies on electron transport through SiN_x in semiconductor devices have observed slow changes in the current due to space charge effects in the dielectric [201–203]. Such space charge effects result from the accumulation of charge injected into the dielectric which leads to a non-uniform charge distribution across the membrane. As shown in Sec. 3.3, similar slow changes in the current were also seen in MIM devices. I have also observed slow changes in the current upon changing the voltage in EIE devices [Fig. 3.9(a)]. The time constant for the decay in current upon making a step change in the voltage from 0 V to 10 V is approximately 2.3 s.

To compare these slow changes in the current to the expected RC time constant I have measured the capacitance using a similar procedure as previously described for MIM devices [Sec. 3.3]. Namely, a triangular wave voltage (f=1 kHz, V_{PP}=100 mV) was applied across the membrane and the resulting current measured [Fig. 3.9(c)]. By doing this, a capacitance of ∼11 pF was obtained. This is about 6 times smaller than the capacitance

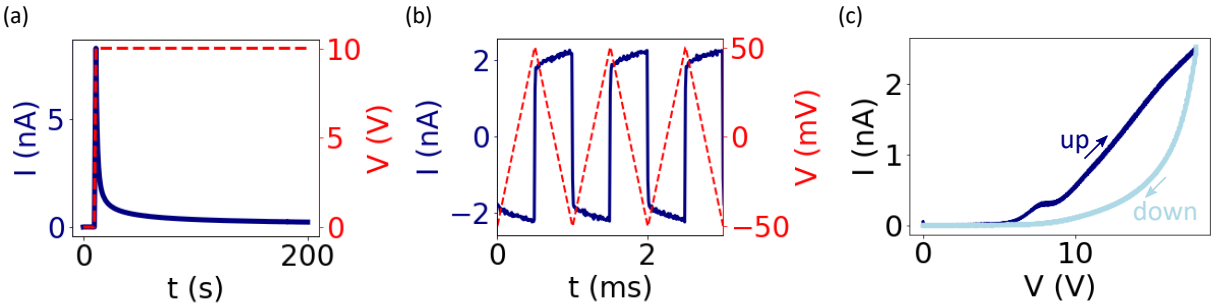


FIGURE 3.9: (a) Change in current when applying a step in the voltage from 0 V to 10 V for an EIE device. (b) Measured current when applying a triangular wave with frequency 1 kHz and amplitude V_{PP}=100 mV for an EIE device. The extracted capacitance from this measurement is 11 pF. (c) Hysteresis in the measured current when ramping the voltage from 0 V, up to 18 V, and then back to 0 V for an EIE device.

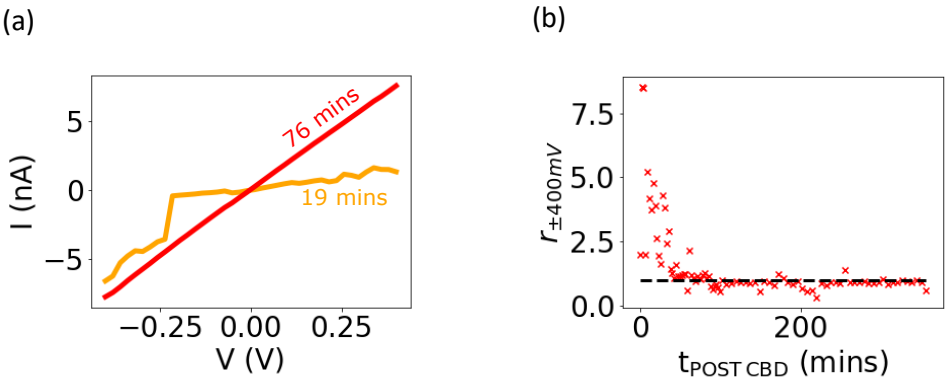


FIGURE 3.10: Rectification in ionic current through a nanopore directly after breakdown. (a) Ionic current through a nanopore as a function of voltage for two times after CBD. (b) Rectification in the ionic current (calculated at ±400 mV) as a function of time after breakdown. Immediately after breakdown the pore demonstrated significant rectification. This is reduced and the current voltage characteristics become approximately linear after an hour.

measured for the MIM devices. This is due to the reduced area exposed to the electrolyte (a circle with diameter ∼1 mm) compared to the large metal electrodes that were deposited on the membrane for MIM devices (∼3x3 mm^2). The extracted capacitance is consistent with values reported in the literature for similar device geometries [61]. Assuming a resistance of 5 kΩ for 1 M KCl [41, 197], the estimated *RC* time constant is ∼50 ns . This is comparable to what is expected from the literature [41], but is much faster than the extracted decay constant when changing the applied voltage from 0 V to 10 V as discussed above. This result suggests that significant space-charge effects resulting from the accumulation of injected charge are also present in EIE devices. Indeed, consistent with this result, hysteresis in the electrical conduction when ramping the voltage from 0 V to 18 V and back to 0 V is also observed [Fig. 3.9(c)]. Similar hysteresis effects have previously been observed during CBD [147, 197].

Charge accumulation in the membrane has important practical implications for the fabrication of nanopores via CBD. Figure 3.10(a) shows measurements of the ionic current through a nanopore as a function of voltage at two time periods following breakdown.

Note that the *RC* time constant places a fundamental limit on the obtainable bandwidth during nanopore sensing. However, in reality the bandwidth is typically much lower than what is possible based on the *RC* time constant. This is due to the low signal-to-noise ratio when operating at high bandwidths due to large capacitive noise in this regime [58, 63]

Consistent with previous studies, significant rectification and instability in the ionic current are observed immediately after breakdown [157]. After a given time period, the pore becomes stable and shows linear current-voltage characteristics. Figure 3.10(b) shows the rectification (calculated at ±400 mV) in the ionic current through the nanopore as a function of time after breakdown. A significant rectification in the ionic current is observed immediately after breakdown which becomes linear after approximately one hour. Such rectification in the ionic current through a nanopore is known to result from either asymmetry in the nanopore geometry or a non-uniform charge distribution along the length of the pore [205–208]. Given the significant change in rectification over time observed here, it is unlikely that the observed rectification results from asymmetry in the pore geometry (since this would require widening of the pore at one side and narrowing at the other). Rather, it is proposed that this is a result of the non-uniform charge distribution along the length of the nanopore resulting from the accumulation of trapped charge during CBD. Following breakdown, the charge becomes slowly detrapped resulting in a reduction in the rectification over time. It is also noted that rectification due to charge accumulation can be observed when thinned regions of the membrane are formed during CBD rather than nanopores [172, 173].

3.8 Conclusion and Outlook

In this chapter I discussed the mechanism of conduction and nanopore formation during CBD. In particular, I demonstrated that depending on the stoichiometry of the SiN_x membrane, conduction is either limited by oxidation reactions that must occur at the membrane-electrolyte interface (Si-rich SiN_x), or charge transport across the dielectric (stoichiometric Si_3N_4). Several important implications of these results are discussed, particular when extending CBD to create nanopores in devices with electrodes on the membrane surface. I also reported results consistent with charge accumulation in the

membrane during CBD and proposed that this leads to the rectification in the ionic current often observed in a nanopore directly after breakdown.

The results shown in this chapter build on the current understanding of the mechanism of conduction and nanopore formation during CBD. Understanding this process will be necessary to further develop CBD as a nanopore fabrication technique in the coming years. Indeed, in the following chapters, the results presented here will be utilised to develop CBD protocols that enable the fabrication of nanopores integrated with on-chip nanoelectrodes. However, there are still many future studies that could be performed to further understand the mechanism of nanopore formation during CBD. In particular, performing breakdown on MIE devices in varying electrolyte compositions may be of interest. While varying the electrolyte composition has previously been done for the commonly used CBD configuration, the MIE devices presented here could build on this work by isolating contributions from oxidation and reduction reactions. Moreover, while the results presented here suggested that charge accumulation may be responsible for rectification in the ionic current through a nanopore after breakdown, directly linking these two phenomenon would be useful. This could be done by performing breakdown at a fixed voltage and comparing the time to breakdown (which should vary the degree of charge accumulation) and the resulting rectification.

Chapter 4

Independent Fabrication of Multiple Nanopores via Controlled Breakdown Using On-Chip Electrodes

In this chapter I demonstrate the fabrication of nanopores via CBD when the electric field is applied between an electrode on the membrane surface and an electrolyte solution in contact with the other side of the membrane. Using this technique, it is shown that multiple nanopores can be independently fabricated (i.e. without affecting the previously created pores) by performing CBD using different electrodes on the membrane surface. This is the first demonstration of nanopore fabrication using CBD by applying the voltage between an on-chip electrode and an electrolyte solution in contact with the other side of the membrane. The development of this new CBD protocol is a step towards a rapid, low-cost, and scalable technique to fabricate arrays of nanopores integrated with complementary on-chip nanostructures.

Results from this chapter and the following chapter are currently being written up for publication. I am also in the process of creating a patent application for these results.

4.1 Motivation

As discussed in Sec. 1.3, there has been interest in developing nanopore sensing modalities in addition to ionic current based detection. These additional sensing modalities often utilise complementary nanostructures such as field-effect sensors, tunnelling nanogaps, or plasmonic nanostructures integrated with a nanopore [19, 20, 46, 209]. One common advantage of many of these additional sensing modalities is that the signal from each nanopore can be read out independently without the need for complex microfluidics to isolate each pore. This opens up routes for the development of high-density arrays of nanopore sensors which is desirable for proposed applications where quantitative analysis is essential (e.g. in clinical diagnostics).

To date, the fabrication of nanopores integrated with complementary nanostructures has been challenging [64, 75]. Most commonly, nanopores in these devices have been fabricated using focused charged particle beams such as those generated in a TEM. However, this technique requires expensive equipment, highly trained operators, and has a low throughput. CBD is a technique that overcomes many of these challenges as it is inexpensive, rapid, and can be fully automated [139, 140]. However, in its most common form (where breakdown is performed by applying a voltage between an electrolyte solution on both sides of the membrane), CBD creates a single nanopore at a random location in the membrane. To overcome this, several advanced CBD techniques have been demonstrated to enable the fabrication of nanopore arrays. This has included the use of an AFM tip to apply the electric field [182], or a micropipette to confine the electrolyte on one side of the membrane [146] (see Sec. 2.4). However, these techniques require relatively complex instrumentation which reduces the appeal of CBD as an accessible nanopore fabrication technique. Moreover, time consuming alignment procedures would be required to integrate nanopores with on-chip nanostructures. The development of accessible CBD techniques to fabricate nanopore arrays, self-aligned with complementary nanostructures,

would significantly accelerate research in this field and open up routes for the commercial development of these devices.

4.2 On-Chip Biasing Fluidic Cell Design

Before discussing the results of this chapter, I will introduce the fluidic cell that was used for these experiments. For this study, it is necessary to control the voltage applied to the on-chip electrodes as well as the voltage of the electrolyte solution in contact with the membrane. To enable this, I have designed a fluidic cell in collaboration with Nanopore Solutions. A schematic and photograph of this on-chip biasing fluidic cell is shown in Fig. 4.1. Similar to the commercially available nanopore fluidic cell that was used in previous chapters when measuring devices without on-chip electrodes, this fluidic cell consists of a central cassette compressed together between two PFTE blocks each containing a 300 μL reservoir [Fig. 4.1(b)]. However, for the on-chip biasing fluidic cell, the cassette was modified so that a printed circuit board (PCB) can be sandwiched between the two halves of the cassette [Fig. 4.1(a)]. The PCB has an aperture for the

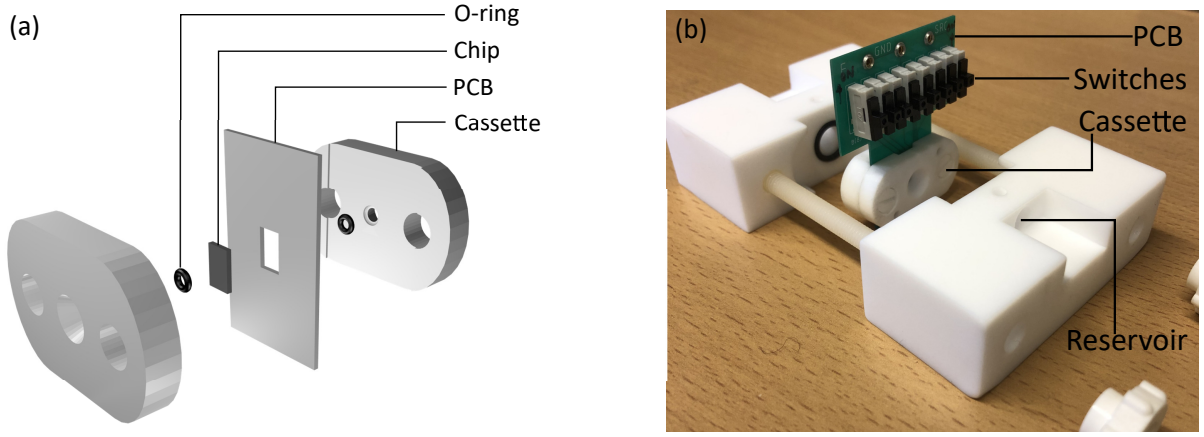


FIGURE 4.1: Fluidic cell design that enables applying voltages (and measuring currents) to the on-chip electrodes and transmembrane (Ag/AgCl) electrodes. (a) Schematic of the cassette design. The chip floats in a socket in the PCB. The chip is then compressed together by O-rings and two halves of a cassette. The cassette then fits into a fluidic cell (not shown in schematic). (b) Photograph of the fluidic cell.

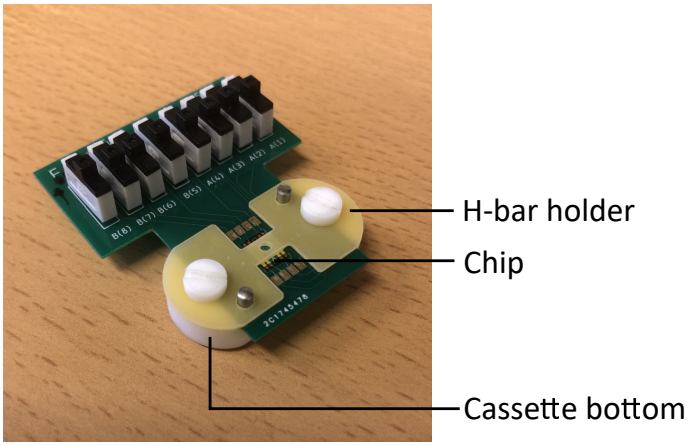


FIGURE 4.2: Photograph of the wire-bonding jig that enables easy wire-bonding of the chip to a printed circuit board as well as transfer of the device to the on-chip biasing fluidic cell described above.

chip to sit in. The O-rings in each half of the cassette compress against the chip when the cassette is screwed together to provide a fluidic seal on each side of the membrane.

To enable electrical contact to the on-chip electrodes, it is necessary to make wire-bonds between electrodes on the chip and the PCB. To do this, I have designed a jig that enables wire-bonding of a device. The device can then be easily transferred to the fluidic cell described above. A photograph of the wire-bonding jig is shown in Fig. 4.2. It consists of a 3D printed acrylic 'H-bar' holder that screws into the bottom half of the on-chip biasing cassette. The 'H-bar' holder provides the down pressure to keep the chip stationary during wire-bonding while also providing access to the electrode contact pads on the chip surface. After wire-bonding, the 'H-bar' holder is removed and the top half on the on-chip biasing cassette is screwed into place.

Unlike several designs of on-chip biasing fluidic cells reported in the literature [21], the strategy described above does not require gluing of the chip to the PCB. Such gluing of the chip can (i) be a tedious process, (ii) be surprisingly expensive, and (iii) make removal of the chip for later experiments such as TEM imaging difficult. Technical drawings for the

A single tube of Kwik Cast which is often used for adhesion of a chip to a PCB in nanopore experiments costs ~£100

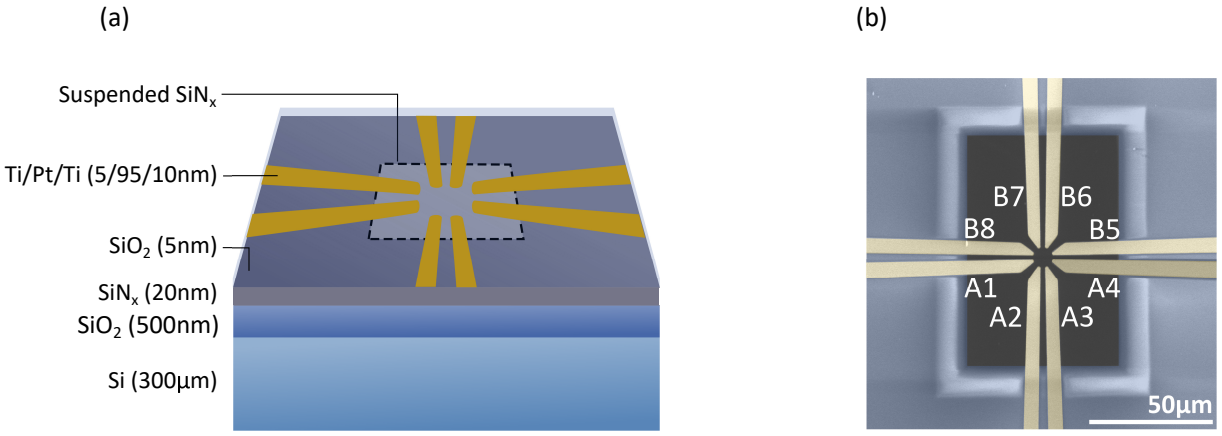


FIGURE 4.3: (a) Schematic of the device geometry used in this chapter. (b) False-colour scanning electron micrograph of the electrode configuration over the suspended region of SiN_x (the suspended SiN_x is the dark grey rectangle). The electrodes are labelled A1-A4 and B5-B8 for convenience in the following discussion (electrode labels are added and are not part of the device geometry).

on-chip biasing cassette and the 'H-bar' holder for wire-bonding are shown in Appendix B.

4.3 Device Geometry and Experimental Setup

A schematic of the device geometry used in this chapter is shown in Fig. 4.3(a). The devices consist of a 20 nm thick Si-rich SiN_x (x=1.14) membrane suspended on a 500 nm thick SiO_2 layer on a 300 μm thick Si substrate. Eight independently addressable metal electrodes (5/95/10 nm Ti/Pt/Ti) were patterned on the membrane surface via photolithography. Finally, a 5 nm thick SiO_2 layer was deposited over the electrodes via atomic layer deposition. A false-colour scanning electron micrograph of the electrode configuration over the suspended region of SiN_x is shown in Fig. 4.3(b). For convenience, in the following discussion the electrodes have been labelled A1-A4 and B5-B8 as shown in Fig. 4.3(b). A detailed description of the fabrication of these devices is given in Appendix A.

The basic experimental setup used for CBD in this chapter is shown in Fig. 4.4(a). Here, CBD was performed by applying a voltage between an electrode on the membrane surface

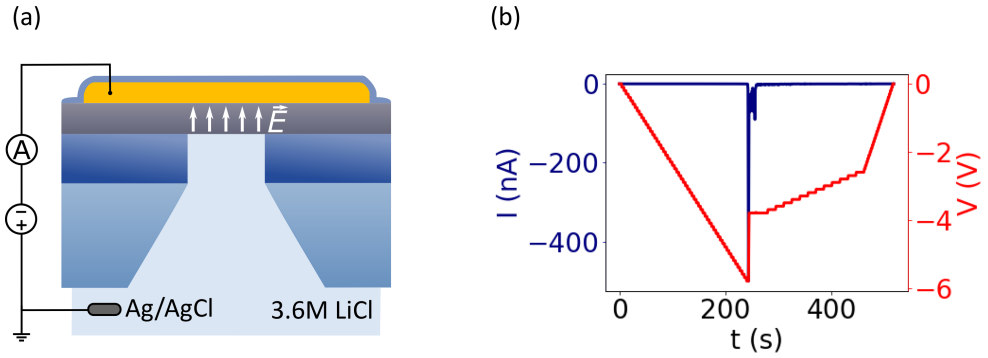


FIGURE 4.4: (a) Schematic of the measurement setup used when performing CBD by applying a voltage between an on-chip electrode and an electrolyte solution in contact with the other side of the membrane. (b) Voltage protocol and resulting measured current when performing CBD by applying a voltage between an on-chip electrode and an electrolyte solution in contact with the other side of the membrane.

and an electrolyte solution in contact with the other side of the membrane. Unlike the most common form of CBD which is performed by applying a voltage between electrolyte solutions in contact with both sides of the membrane, in this experimental setup the electrolyte is only present on one side of the device. The advantage of this CBD configuration is that it enables the independent fabrication of multiple nanopores in a single membrane without affecting previously created pores. If electrolyte was present on both sides of the membrane (as is typically the case in CBD), previously created nanopores would be enlarged during each new breakdown event since a significant ionic current would flow through the pore [151, 152].

Unless noted otherwise, in this chapter CBD was performed by applying a negative voltage to an on-chip electrode while the electrolyte solution in contact with the other side of the membrane is held at ground. This is the forward-biased configuration as discussed in Sec. 3.4 (i.e. an oxidation reaction does not need to occur to inject electrons into the dielectric since they can be supplied by the metal electrode). This results in breakdown occurring at a relatively low voltage (∼5-6 V). To perform CBD, the amplitude of the voltage applied to the on-chip electrode was increased in steps of 100 mV every 4 s while simultaneously measuring the resulting current. When a spike in the current is observed, the voltage was immediately reduced to a pre-defined value of 3.8 V and held at this

value for 20 s. The voltage was then reduced in steps of 100 mV every 15 s to a value of 2.5 V, and then to 0 V in steps of 100 mV every 2 s. After testing several different voltage protocols, it was found that above protocol was able to consistently fabricate nanopores with diameters in the range of 1-15 nm. A typical nanopore fabrication experiment using this protocol is shown in Fig. 4.4(b).

It is noted that the breakdown protocol described above is different from that typically used during CBD where the voltage is applied between electrolyte solutions in contact with either side of the membrane. In such measurements, the voltage is typically immediately reduced to 0 V following breakdown [see Sec. 2.8] [139]. However, when performing CBD on devices with on-chip electrodes in the forward-biased configuration, breakdown occurs at relatively low voltages (5-6 V). If the voltage is immediately reduced following breakdown at such low voltages, 'soft-breakdown' will typically occur. This is where the membrane material is not fully removed during breakdown to form a nanopore [139, 159]. As such, it is necessary to slowly reduce the voltage following breakdown to create nanopores using this CBD configuration. CBD was also performed using 3.6 M LiCl as the electrolyte for experiments in this chapter.

4.4 Independent Fabrication of Multiple Nanopores

The main advantage of performing CBD by applying a voltage between an on-chip electrode and an electrolyte solution is that it enables the independent fabrication of multiple nanopores in a membrane. Figure 4.5 shows four CBD experiments performed on a single membrane where the breakdown voltage was applied to a different on-chip electrode for each measurement. Each CBD measurement is quantitatively similar, with breakdown occurring at -5.8,-5.5,-5.7, and -5.6 V. Moreover, the leakage current prior to breakdown is similar for each CBD measurement with values of -110,-125,-106, and -124 pA measured at 5 V. The fact that the current prior to breakdown is independent of previous CBD

measurements indicates that there is no fluidic connection between the on-chip electrodes after nanopore formation. Namely, if there was a fluidic connection between the on-chip electrodes, redox reactions would occur due to the large voltage difference between the electrodes which would modify the measured current. This is an important result as it enables the independent fabrication of multiple nanopores in a single membrane without affecting the previously created pores.

To determine the position and number of nanopores created using this CBD protocol, fluorescence imaging of the nanopores was performed [95, 96, 171]. Fluorescence imaging of nanopores was discussed in detail in Sec. 3.5. Figure 4.6 shows fluorescence micrographs of the nanopores formed from the CBD measurements shown in Fig. 4.5. Three fluorescence micrographs are shown representing a time series of data with a frame before, during, and after the application of a voltage that drives Ca^{2+} ions through the nanopore. The white dashed box represents the edge of the suspended region of SiN_x. The solid white/red lines represent the position of the on-chip electrodes with red lines for electrodes that CBD was performed on and white lines for electrodes that CBD was not performed on.

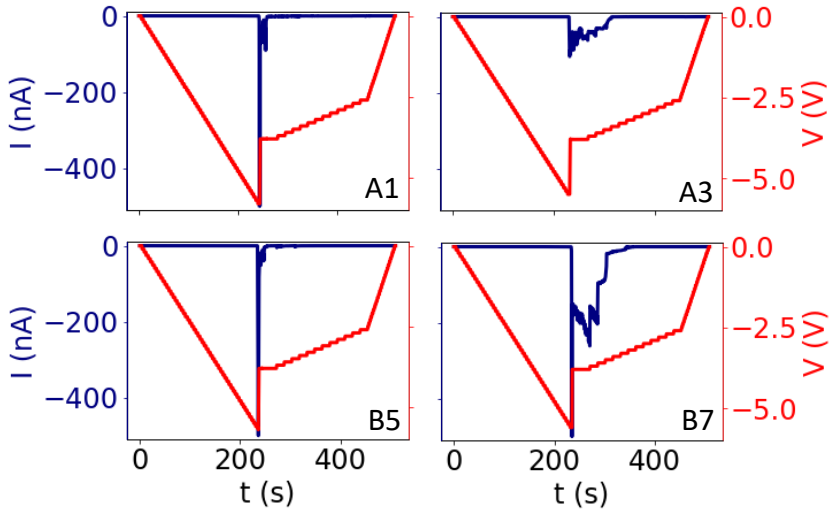


FIGURE 4.5: CBD measurements performed by applying a voltage between an on-chip electrode and an electrolyte solution in contact with the other side of the membrane. The four measurements were performed on the same membrane by applying a voltage to a different on-chip electrode. The on-chip electrode that the voltage was applied to is shown in the bottom right hand corner of the plot (see Fig. 4.3 for the electrode naming convention).

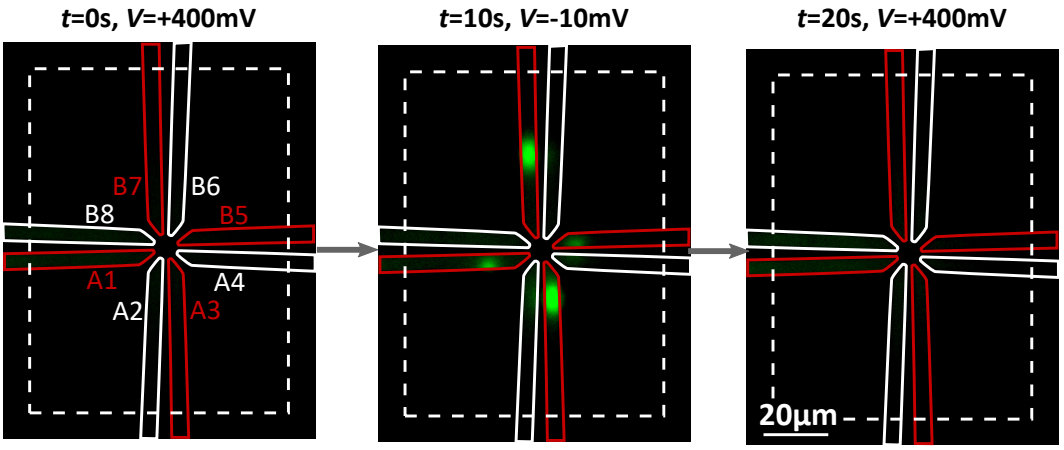


FIGURE 4.6: Fluorescence micrographs of nanopores created when a voltage is applied between an on-chip electrode and an electrolyte solution in contact with the other side of the membrane. The white dashed box depicts the edge of the suspended region of SiN_x. The red/white solid lines depict the electrode positions with red lines for electrodes that CBD was performed on and white lines for electrodes that CBD was not performed on. The three images represent a time series of data, with an image before, during, and after the application of a voltage that drive Ca^{2+} ions through the nanopore.

When a voltage is applied to drive Ca^{2+} ions through the nanopore, a single fluorescence signal is observed in each electrode that CBD was performed on. No fluorescence signals are observed in electrodes that CBD was not performed on. Changes in the brightness of the signal at each nanopore correspond to differences in the size of the created pore [171]. This result demonstrates that the CBD protocol used here enables the independent fabrication of a single nanopore in each electrode on the membrane surface.

To further characterise the nanopores created via this CBD protocol, TEM imaging of the nanopores was performed. Figure 4.7 shows bright-field (top row) and high-angle annular dark field (bottom row) scanning transmission electron micrographs of a created nanopore at various magnifications. A nanopore with diameter ~20 nm is observed in the SiN_x membrane (see right most images). This is surrounded by a larger region (200 nm) where the metal has been removed. A similar pore structure was previously reported in devices where CBD was used to create nanopores in a SiN_x membrane covered by a metal film [162]. Here, the removal of metal from around the nanopore was thought to result from electrochemical reactions that occur during breakdown and nanopore expansion when a large ionic current flows through the pore. However, future studies may be required

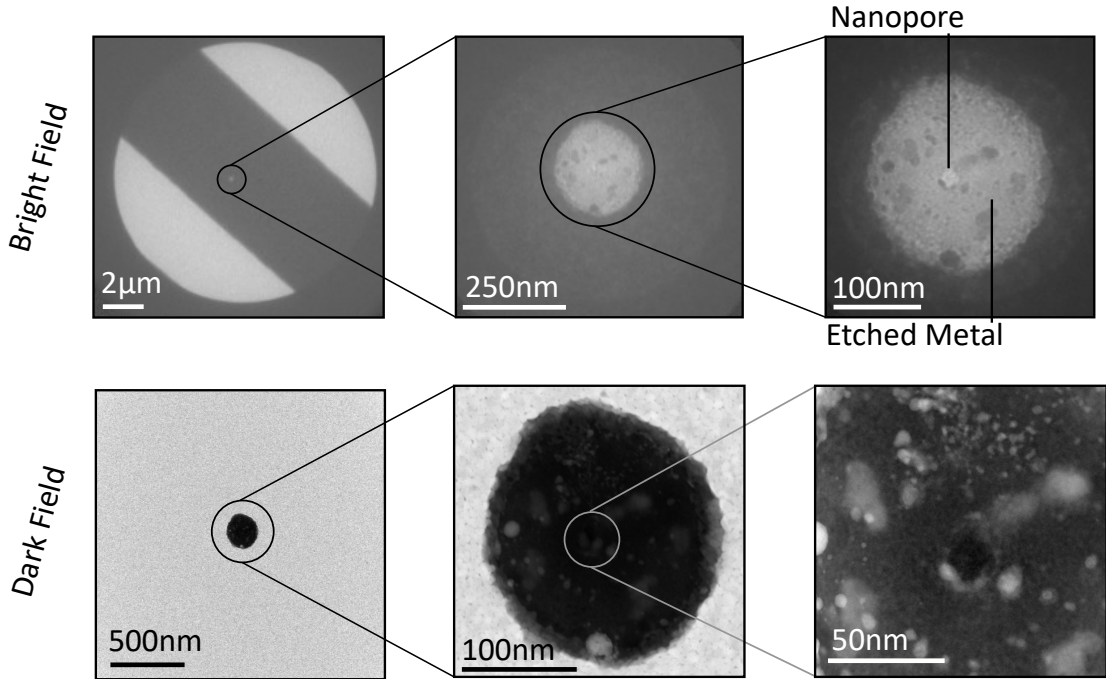


FIGURE 4.7: Bright field (top row) and high-angle annual dark field (bottom row) scanning transmission electron microscope images of a nanopore formed using the CBD protocol introduced in this chapter. Images of the nanopore are shown at various magnifications.

to confirm this is the mechanism by which metal is removed around the pore. Note that the pore diameter observed via TEM imaging (∼17.2 nm) is comparable to that estimated from conductance measurements (∼18.7 nm). This slight difference may result from errors in the effective length of the nanopore used to estimate the diameter from the conductance measurements. Namely, the effective length of the nanopore was assumed to be equal to the membrane thickness. However, previous studies have shown that the effective length of nanopores created via CBD can range from the membrane thickness down to one third of the membrane thickness [145, 158, 159, 171]. Pore expansion [117, 157] during the various experiments that were performed between conductance measurements and TEM imaging (such as fluorescence imaging) may also result in differences in the nanopore diameter estimated from these two methods.

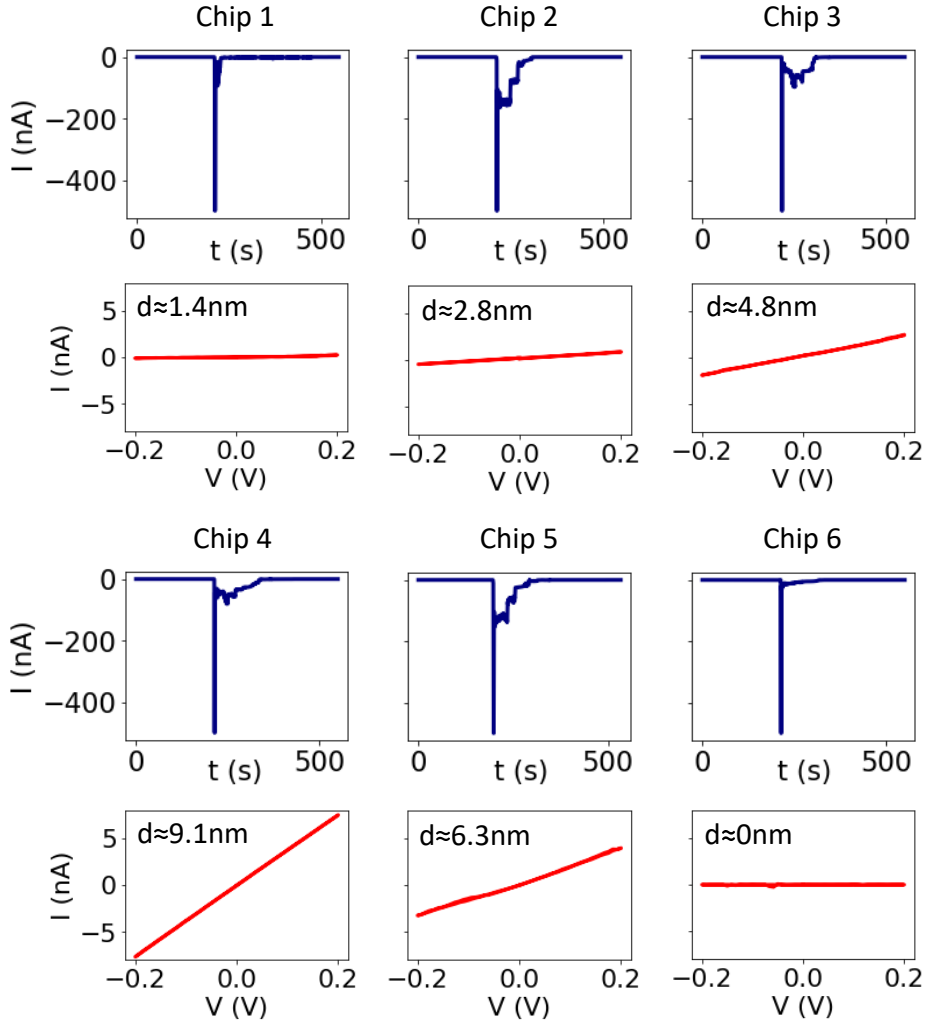


FIGURE 4.8: CBD measurements (top panel) and the resulting conductance of the created nanopore for six different devices.

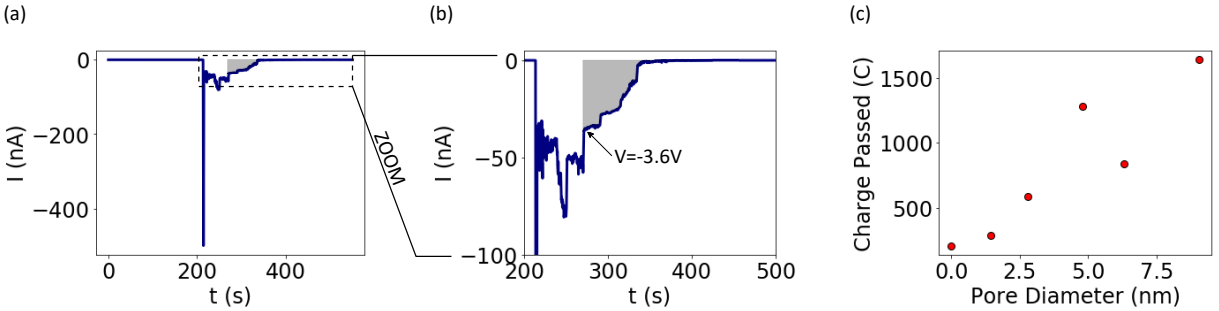


FIGURE 4.9: (a) A typical CBD trace and (b) a zoom in of that trace after breakdown. The grey shaded region represents the area that is integrated to quantify the charge passed after breakdown. (c) Plot of the charge passed after breakdown and the resulting nanopore diameter for six membranes.

4.5 Resulting Nanopore Diameters

To characterise the size of the nanopores created by this CBD protocol, I have fabricated a single pore in six different membranes. After fabricating the nanopore, reservoirs on both sides of the membrane were filled with 3.6 M LiCl and left for one hour to allow the ionic current through the pore to stabilise. Figure 4.8 shows the CBD curve along with a measurement of the resulting nanopore conductance for each device. The resulting nanopore diameters estimated from Eq. 2.1 are 1.4, 2.8, 4.8, 9.1, and 6.3 nm. One device underwent soft breakdown and no appreciable nanopore was created. Interestingly, by comparing the CBD curves and the resulting nanopore conductance, a correlation between the current measured while ramping the voltage to zero following breakdown and the resulting nanopore diameter is observed. Namely, measuring a greater current when ramping the voltage to zero after breakdown generally results in the formation of a larger nanopore (e.g. compare the CBD curves and resulting pore diameter of chip 5 and chip 6).

To further highlight this correlation between the current measured after breakdown and the resulting nanopore diameter, I have quantified the charge passed after breakdown while the voltage is being decreased to zero. Namely, I have integrated the current between -3.6 V and 0 V while the voltage is reduced after breakdown [shaded area in Fig. 4.9(a)-(b)]. As shown in Fig. 4.9(c), in general there is an increase in the nanopore diameter with increasing charge passed after breakdown. This is a promising result as it indicates that the nanopore diameter could be precisely controlled by using an active feedback where the rate at which the voltage is ramped down after breakdown depends on the measured current.

4.6 Reverse Biased Configuration

I have also created nanopores by performing breakdown between an on-chip electrode and an electrolyte solution when the electric field is applied in the reverse-biased configuration. As described in Sec. 3.4, the reverse-biased configuration is achieved when the electric field is applied so that an oxidation reaction must occur to inject electrons into the membrane (i.e. electrons cannot be supplied by the on-chip electrode). Since breakdown occurs at a much higher voltage for this electric field configuration, a typical CBD protocol was used for these measurements whereby the voltage is immediately reduced to zero following breakdown. Figure 4.10 shows four CBD experiments performed on a single membrane where the breakdown voltage was applied to a different on-chip electrode for each measurement. Similar to the forward-biased configuration, each CBD curve is similar regardless of whether or not breakdown had previously been performed on the membrane. This indicates that there is no fluidic connection between the on-chip electrodes after nanopore formation which enables the independent fabrication of multiple nanopores in a single membrane.

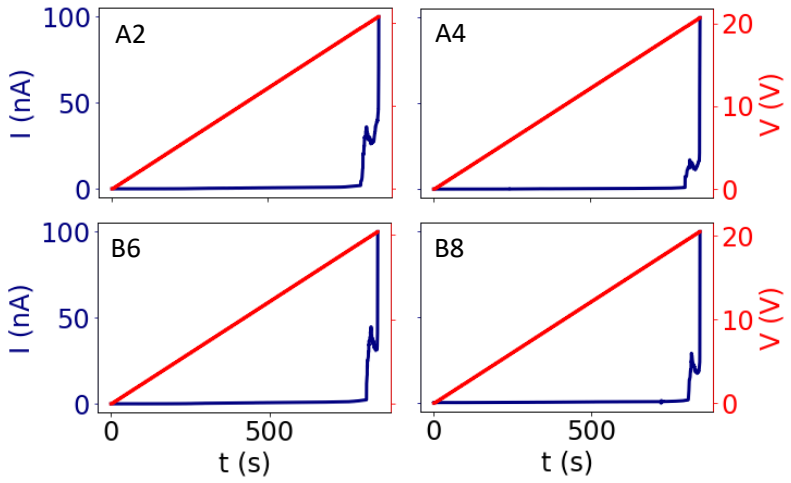


FIGURE 4.10: CBD measurements where the voltage is applied between an on-chip electrode and an electrolyte solution in contact with the other side of the membrane in the reverse-biased configuration. Four measurements were performed using different electrodes on a single membrane.

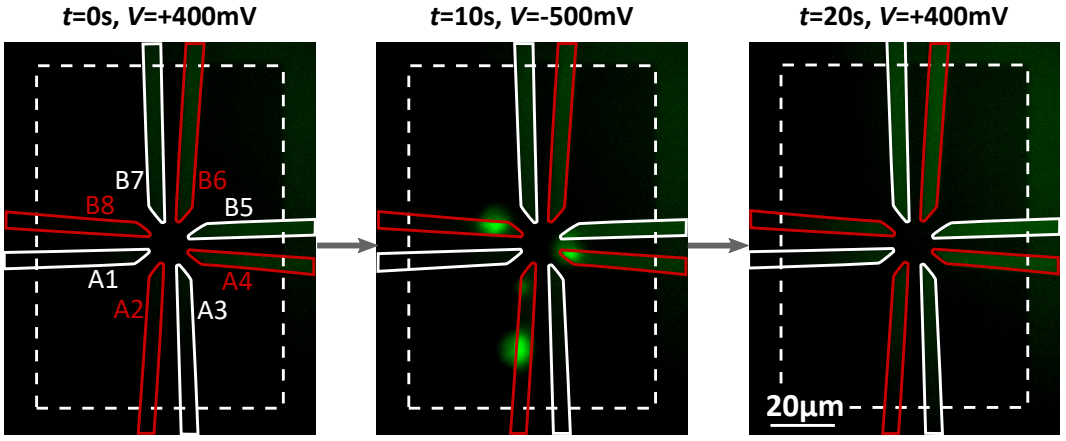


FIGURE 4.11: Fluorescence micrographs of nanopores when CBD is performed in the reverse-biased configuration. The dashed white box shows the edge of the suspended region of SiN_x. The solid red/white lines show the edges of the electrodes with the red lines for electrodes CBD was performed on and white lines for electrodes CBD was not performed on. There are three micrographs representing a time-series of data with one frame before, during, and after the application of a voltage which drives Ca^{2+} ions through the nanopore.

To demonstrate the presence of nanopores when CBD is performed in the reverse-biased configuration, fluorescence imaging of these pores was again performed. As shown in Fig. 4.11, nanopores were only created in the electrodes that CBD was performed on. It is noted that no fluorescence signal is observed in electrode 'B6' despite the fact that CBD was performed using this electrode. This may be because either there was no pore created in this electrode, or the pore was clogged prior to fluorescence imaging. Moreover, there are two nanopores formed in electrode 'A2' (a weak fluorescence signal can be observed close to the pore tip). These results demonstrate that although it is possible to independently fabricate multiple nanopores in a single membrane using the reverse-biased CBD configuration, the protocol/device geometry may need to be optimised to ensure the reproducible fabrication of a single nanopore. Indeed, an advantage of performing CBD in the forward-biased configuration is that the low breakdown voltage results in slow nanopore formation. This reduces the requirement for stringent feedback conditions to ensure the formation of a single nanopore and should enable tuning of the nanopore diameter using active feedback of the applied voltage following breakdown (as described in Sec. 4.5).

4.7 Biomolecular Translocation

To demonstrate the utility of nanopores fabricated using the CBD protocol described in this chapter, I have detected translocation of dsDNA through these pores. To do this, a single nanopore was created in the membrane by performing CBD in the forward-biased configuration. Following breakdown, reservoirs on both sides of the membrane were filled with 3.6 M LiCl and the device was left overnight to allow the nanopore to stabilise [157, 188]. Following this, a stable, linear, ionic current was measured through the pore when a voltage is applied between Ag/AgCl electrodes inserted into each reservoir [Fig. 4.12]. The potential of the on-chip electrodes and the *cis* chamber were held at ground while the transmembrane voltage is applied to the *trans* chamber. The diameter of the nanopore as estimated from Eq. 2.1 was ∼13 nm. The noise spectrum of the ionic current at an applied voltage of 200 mV is shown in Fig. 4.12. The noise spectrum is comparable to those observed for solid-state nanopores fabricated via TEM drilling [59] and CBD when the voltage is applied via electrolyte solutions on both sides of the membrane [139]. Integrating the normalised noise spectrum between 1-100 Hz to quantify the low-frequency noise (as per Eq. 2.2) yields a value of $6\text{x}10^{-4}$ which is well below the

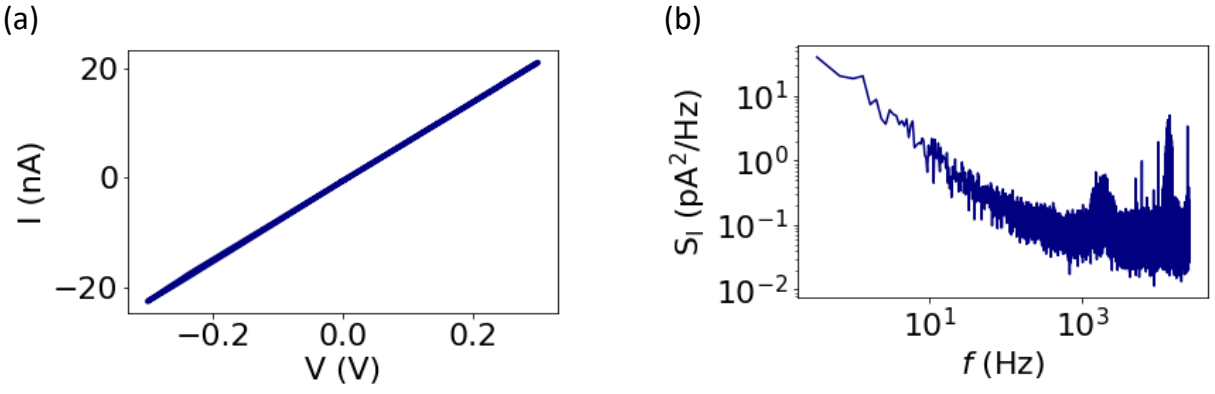


FIGURE 4.12: Ionic current characteristics of a nanopore fabricated by CBD when the voltage is applied between an on-chip electrode and an electrolyte solution in contact with the other side of the membrane. (a) Ionic current as a function of voltage applied to Ag/AgCl electrodes on each side of the membrane. (b) Noise spectrum of the ionic current as measured at 200 mV. Measurements were performed in 3.6 M LiCl and the pore was left to stabilise in this buffer overnight after CBD. On-chip electrodes were held at ground during these measurements.

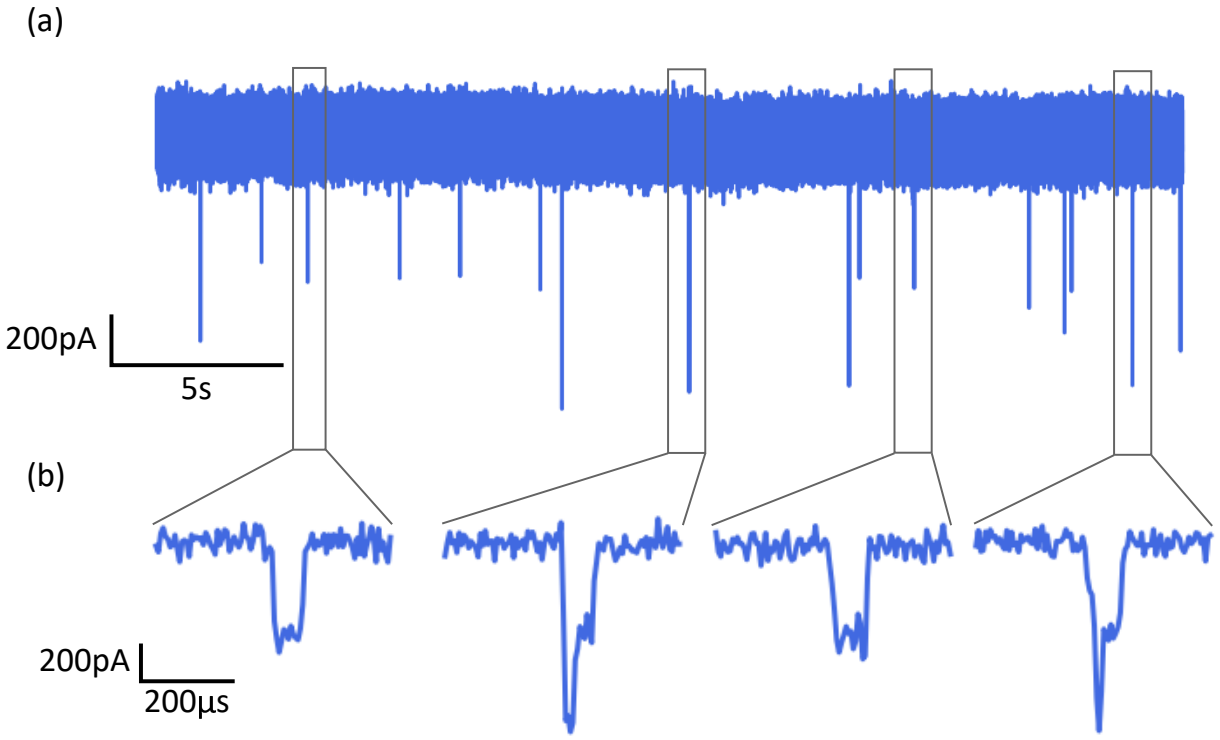


FIGURE 4.13: DNA translocation through a nanopore fabricated by CBD where the voltage is applied between an on-chip metal electrode and an electrolyte solution in contact with the other side of the membrane. (a) Example of translocation of 1 kbp dsDNA through a 13 nm nanopore at 200 mV. (b) Zoom of several events shown in (a) demonstrating the translocation of folded and unfolded DNA strands. Measurements were performed in 3.6 M LiCl with a final DNA concentration of 5 nM. Data was low pass filtered at 100 kHz and sampled at 200 kHz.

threshold of $1x10^{-2}$ required for a nanopore to be usable for single-molecule biosensing applications [139].

To detect analyte translocation through the nanopore, the *cis* chamber was 'spiked' with 1 kbp dsDNA (NoLimits 1000bp DNA, ThermoFisher, SM1671) and the solution was mixed using a pipette resulting in a final DNA concentration of ~5 nM. When a positive voltage was applied to the *trans* chamber, transient decreases in the ionic current were observed typical of DNA translocation through the nanopore [Fig. 4.13]. Closer inspection of the current transients reveal that the translocation events can be classified into two groups: (i) single-level current blockades, and (ii) two-level current blockades. This is typical of DNA translocation through solid-state nanopores with diameters significantly larger than the cross section of dsDNA (~2.4 nm). As discussed in Sec. 2.8, single-level and

two-level current blockades are indicative of the translocation of dsDNA in an unfolded and folded manner respectively [193]. These results confirm that nanopores fabricated via the CBD protocol developed in this chapter can be used for single-molecule biosensing applications.

4.8 Conclusion and Outlook

In this chapter I introduced a new CBD protocol that enabled the independent fabrication of multiple nanopores in a single membrane. This was done by applying the breakdown voltage between an on-chip electrode and an electrolyte solution in contact with the other side of the membrane. Importantly, in this CBD configuration, there is no electrolyte present on the front-side of the membrane. This ensures that previously fabricated nanopores are not expanded during each new breakdown event. Together with the results presented in the following chapter, this is a promising step towards the fabrication of high density arrays of nanopores integrated with on-chip nanostructures.

There is still significant research that could be performed in the coming years to further characterise this CBD protocol. It is first noted that, to be able to independently fabricate nanopores there must not be a fluidic connection between electrodes on the membrane surface. As such, it would be useful to characterise the area of electrolyte in contact with the front of the membrane after nanopore formation since this would limit the array density that can be achieved. The CBD protocol could also be easily optimised in the coming years by developing active feedback conditions after breakdown to enable finer control over the resulting nanopore size. Another interesting area for future work would be to characterise nanopores fabricated in the reverse-biased configuration using TEM imaging. In this chapter, it was demonstrated that removal of the metal around a nanopore occurs when breakdown is performed in the forward-biased configuration. However, given the significantly different breakdown protocols depending on the electric field direction,

removal of the metal may be different for the reverse-biased configuration. Indeed, minimising removal of the metal electrode will be important in future studies when using this technique to integrate nanopores with on-chip nanoelectrodes.

Chapter 5

Self-Aligning Nanopores with Complementary Nanostructures using Controlled Breakdown

Here, I extend the CBD protocol introduced in the previous chapter to fabricate nanopores that are self-aligned with on-chip nanostructures. This technique relies on passing a large current density through an on-chip metal nanoconstriction to induce localised Joule heating of the membrane. I demonstrate that performing CBD simultaneous to Joule heating results in nanopore formation at the narrowest part of the constriction. Together with the results presented in the previous chapter, this opens up a route towards the fabrication of high-density arrays of nanopores integrated with on-chip nanostructures.

Results from this chapter and the previous chapter are currently being written up for publication. I am also in the process of creating a patent application for these results.

5.1 Motivation

As discussed in previous chapters, there has been significant interest in fabricating nanopores integrated with complementary on-chip nanostructures. Such on-chip nanostructures may include field-effect sensors, tunnelling nanogaps, and plasmonic nanodevices. These nanostructures provide alternative sensing modalities which can overcome some of the limitations of ionic current based detection including low device densities and limited detection bandwidth. Moreover, in some cases, they can probe molecular properties not possible using ionic current based detection [22]. Unfortunately, the fabrication of nanopores integrated with on-chip nanostructures has often relied on time consuming processes that can have a low yield (e.g. drilling pores and sculpting nanostructures in a TEM [64, 72, 75]). To overcome this, complementary nanostructures have recently been integrated with nanopores in glass pipettes [131, 164, 210]. However, it is difficult to extend this technique to fabricate high density arrays of nanopores as desired for most commercial applications.

In the previous chapter, I introduced a new CBD protocol that can be used to independently fabricate many nanopores in a single membrane. This technique relied on applying a voltage between an on-chip electrode and an electrolyte solution in contact with the other side of the membrane. The resulting nanopore formed at a random location in the on-chip electrode. However, most of the advanced nanopore sensing strategies (as discussed in Sec. 1.3) rely on precisely aligning a nanopore with an on-chip nanostructure. As such, for the CBD technique described in the previous chapter to reach its full potential, it will be necessary to extend this method to enable the fabrication of nanopores aligned with on-chip nanostructures. The development of such an accessible technique to fabricate nanopores self-aligned with complementary nanostructures would accelerate research into advanced nanopore sensing modalities and open up routes for the development of these devices for commercial applications.

5.2 Device geometry and Experimental Setup

A schematic of the device geometry is shown in Fig. 5.1(a). The devices are similar to those used in previous chapters. Namely, each device consists of a 20 nm thick Si-rich SiN_x membrane (x=1.14) suspended on a 500 nm thick SiO_2 layer on a Si substrate. Metal electrodes (5/75 nm Cr/Au) were deposited on the membrane surface via photolithography followed by thermal evaporation. Electron beam lithography was then used to pattern a metal nanoconstriction (5/30 nm Cr/Au) between two of these electrodes. Note that unlike devices discussed in Chapter 4, a thin passivation layer was not deposited over the electrodes for these devices. False colour scanning electron micrographs of the electrode configuration over the suspended region of SiN_x are shown in Fig. 5.1(b). The width at the narrowest part of the nanoconstriction is approximately 200 nm [Fig. 5.1(b)(ii)]. A detailed description of the fabrication process for these devices is given in Appendix A.

Figure 5.1(c) shows a schematic of the experimental setup used in this chapter. Similar to Chapter 4, CBD was performed by applying a voltage between an on-chip electrode and an electrolyte solution in contact with the other side of the membrane. However, for experiments in this chapter, a transverse voltage (V_{TV}) was applied across the on-chip electrodes to drive a current (I_{TV}) through the metal nanoconstriction and produce significant Joule heating at the centre of the constriction. Simultaneous to this, an increasing transmembrane voltage (V_{TM}) was applied to the electrolyte solution which drives a transmembrane leakage current (I_{TM}) and eventually induces breakdown. Breakdown was performed in the reverse-biased configuration (as described in Sec. 3.4) with a positive voltage applied across the nanoconstriction and a negative voltage applied to the electrolyte solution. The reverse-biased configuration was used since, as demonstrated below, the breakdown voltage has a larger temperature dependence than the forward-biased configuration. Note, as shown in Appendix C, these devices are very sensitive to electric discharge. This amplifies the importance of designing an easy to use fluidic cell that eliminates the need

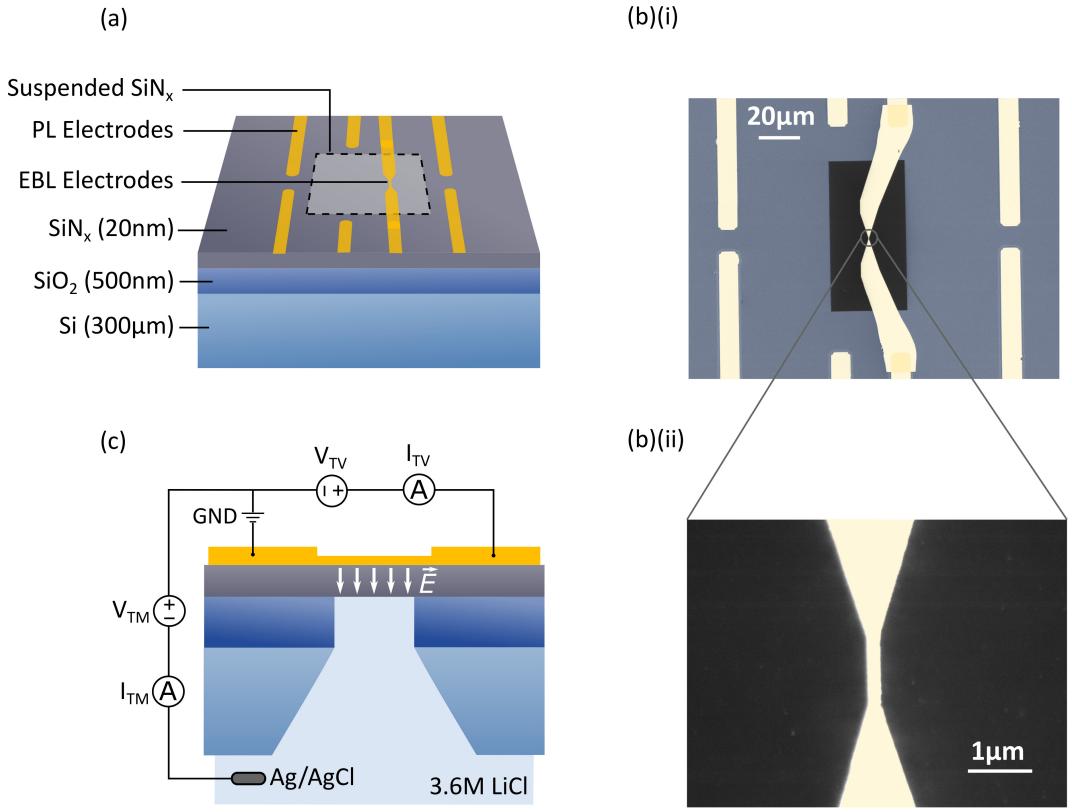


FIGURE 5.1: (a) Schematic of the device geometry used in this chapter. (b) False-colour scanning electron micrographs of (i) the electrode configuration over the suspended region of SiN_x and (ii) the narrowest part of the metal nanoconstriction. (c) Schematic of the experimental setup used in this chapter.

for switching cables during measurements (e.g. to measure a different device on the same membrane). Such a fluidic cell was described in Sec. 4.2.

5.3 CBD Temperature Dependence

Before discussing the integration of nanopores with the metal nanoconstrictions described above, it is first necessary to understand how temperature affects the voltage at which breakdown occurs. This is important, since the proposed technique relies on passing a large current density through the nanoconstriction to locally Joule heat the membrane and thereby confine nanopore formation to this region. It is known from studies of dielectric breakdown in microelectronic devices that the electric field at which breakdown occurs

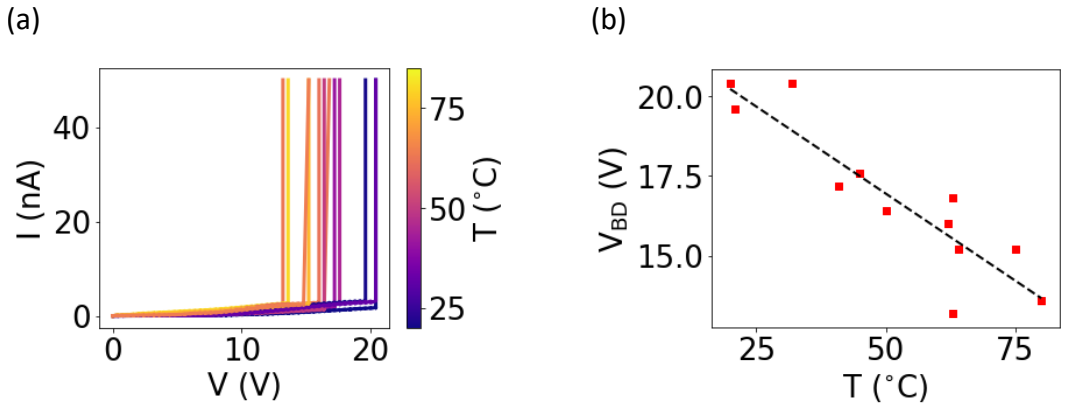


FIGURE 5.2: (a) CBD measurements as a function of temperature. Measurements were performed in the most commonly used CBD configuration where the voltage is applied between electrolyte solutions on either side of the membrane. (b) Shows the breakdown voltage from (a) as a function of temperature.

at depends on the membrane temperature [148, 186]. Moreover, the breakdown voltage during CBD has also been demonstrated to decrease with increasing temperature [197]. However, it is noted that this work utilised stoichiometric SiN_x membranes as opposed to Si-rich SiN_x used here. As discussed in Sec. 3.6, the membrane stoichiometry can affect the electrical conduction mechanism during CBD. As such, it is necessary to confirm that the breakdown voltage also decreases with increasing temperature for the membranes used in this study.

Firstly, I have demonstrated the temperature dependence of the breakdown voltage (V_{BD}) when CBD is performed in its most common configuration (i.e. the voltage is applied via electrolyte solutions on both sides of the membrane). This was done by placing the fluidic cell on a hot-plate and allowing the system to equilibrate for approximately one hour. The electrolyte reservoirs were covered during this period to avoid evaporation of the solution. Figure 5.2(a) shows CBD measurements for a range of temperatures. There is a decrease in the voltage at which breakdown occurs with increasing temperature. This is further highlighted in Fig. 5.2(b) which plots the breakdown voltage as a function of temperature. The breakdown voltage decreases approximately linearly with temperature. The line of best fit (black dashed line) has a gradient of -0.11 V/°C.

As described in Chapters 3 and 4, when CBD is performed by applying a voltage between an on-chip electrode and an electrolyte solution in contact with the other side of the membrane, the mechanism of electrical conduction depends on the direction the electric field is applied. As such, I have also measured the temperature dependence of breakdown when the voltage is applied between an on-chip electrode and an electrolyte solution in the forward and reverse-biased configurations.

Figure 5.3 shows the breakdown voltage as a function of temperature for the forward and reverse-biased configurations. For both electric field configurations, there is an approximately linear decrease in the breakdown voltage with increasing temperature. However, the decrease in breakdown voltage is less pronounced for the forward-biased configuration compared to the reverse-biased configuration. Indeed, the gradient of the lines of best fit are -0.012 and -0.053 V/°C for the forward and reverse-biased configurations respectively. This difference in the temperature dependence of the breakdown voltage is likely a result of the different conduction mechanisms for these two electric field configurations (as discussed in Sec. 3.4). Namely, for the reverse-biased configuration, conduction is limited by oxidation reactions that must occur at the membrane-electrolyte interface. On the other hand, for the forward-biased configuration, conduction is limited by charge transport through the dielectric. Given the greater temperature dependence of the breakdown voltage for devices in the reverse-biased configuration, this electric field configuration will be used in the experiments discussed below.

5.4 Electromigration of Metal Nanoconstrictions

The above results are promising as they demonstrate that it should be possible to confine nanopore formation via CBD by locally increasing the temperature of the membrane. As such, it is now useful to understand how much the temperature of the membrane is increased when passing a current through a metal nanoconstriction. Fortunately, this

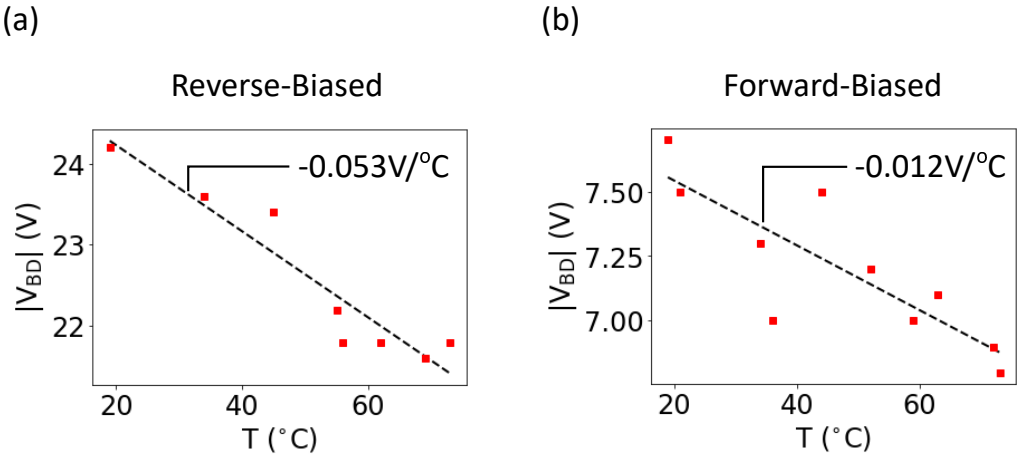


FIGURE 5.3: Temperature dependence of the breakdown voltage when the electric field is applied between an on-chip electrode and an electrolyte solution in contact with the other side of the membrane. This is shown for devices in the (a) reverse-biased configuration and (b) forward-biased configuration.

question has largely been answered by previous works that have performed electromigration of gold nanoconstrictions to fabricate nanogap devices. Such devices have been used for a range of applications including molecular electronics [211, 212], thermoelectrics [213], and single-molecule biosensing [78]. Electromigration is typically performed by applying a voltage across a metal nanoconstriction resulting in a high current density ($J \sim 1\text{x}10^{12}\text{A/m}^2$ [214]) at the centre of the constriction. This large current density leads to the migration of metal atoms due to momentum transfer from the electrons [215]. This process is assisted by a local increase in temperature at the centre of the constriction due to Joule heating. Indeed, previous studies have used scanning thermal microscopy to map the temperature increase during electromigration of gold nanoconstrictions [215]. Here, it was demonstrated that the temperature 100 nm away from the narrowest part of the constriction could reach up to 660 K during electromigration [215]. The temperature at the narrowest part of the constriction was likely even higher.

Although electromigration will not be used to create nanostructures here, it is still useful to perform this technique on some devices to understand the operating limits of the nanoconstrictions fabricated in this work. As shown in Fig. 5.4(a), I have performed electromigration of these devices by increasing the voltage applied across the constriction

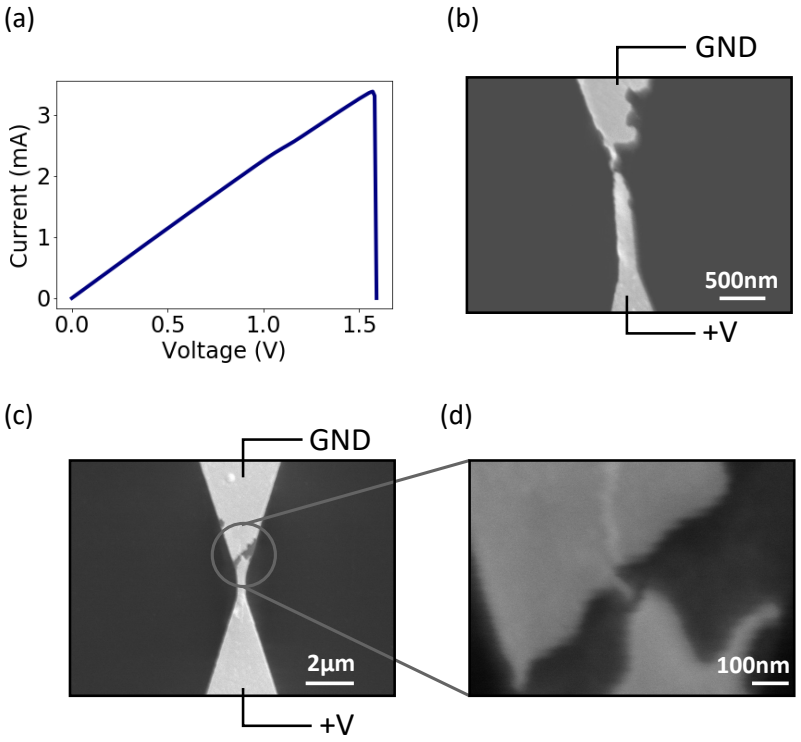


FIGURE 5.4: (a) Example measurement of electromigration in a metal nanoconstriction. The voltage was increased while simultaneously measuring the resulting current. When the current drops to zero the device has undergone electromigration. (b-c) Example scanning electron micrographs of electromigration in the metal nanoconstriction. (d) Shows a zoom of (c) at the region of electromigration highlighting the formation of a sub 50 nm gap.

while monitoring the resulting current. When the applied voltage reaches ∼1.5 V, the current abruptly decreases to zero indicating electromigration of the device. Indeed, SEM imaging of devices following electromigration reveals the formation of a nanometric sized gap. The voltage at which breakdown occurs at is consistent with the literature for similar device geometries [215], and reproducible across multiple devices (for three devices the voltage at which electromigration occurred at was 1.57, 1.59, and 1.60 V). It is also noted that, consistent with previous works [216], the nanogap forms on the side of the constriction that electrons are injected from. Based on these results, the voltage applied across the metal nanoconstriction during CBD is limited to 1 V. This voltage is chosen as it leads to significant Joule heating of the membrane while ensuring that electromigration of the nanoconstriction does not occur. Indeed, I have applied a voltage of 1 V across the nanoconstriction for 20 minutes without observing gap formation.

5.5 Localised Breakdown via Joule Heating

Figure 5.5 shows a typical CBD measurement where a large current density was passed through the metal nanoconstriction simultaneous to performing CBD. To perform these experiments, the voltage applied across the metal nanoconstriction was quickly ramped to 1 V and held at this value [Fig. 5.5(b)]. The voltage across the membrane was then increased in steps of 100 mV every 4 s until breakdown is observed [Fig. 5.5(a)]. When breakdown occurs, V_{TV} and V_{TM} were both quickly reduced to zero. Notably, when breakdown occurs, the current through the metal nanoconstriction drops to zero. As will be discussed below, this indicates that there is damage to the metal nanoconstriction after breakdown.

To determine the position of the nanopores created by this CBD protocol, fluorescence imaging was performed. A detailed description of the method used to perform fluorescence imaging was given in Sec. 3.5. Fluorescence micrographs of the created nanopores are shown in Fig. 5.6 for three different chips. The white dashed box represents the edge of the suspended region of SiN_x while the solid white lines represent the edges of the electrodes. For each chip, three micrographs are shown representing a time-series of data

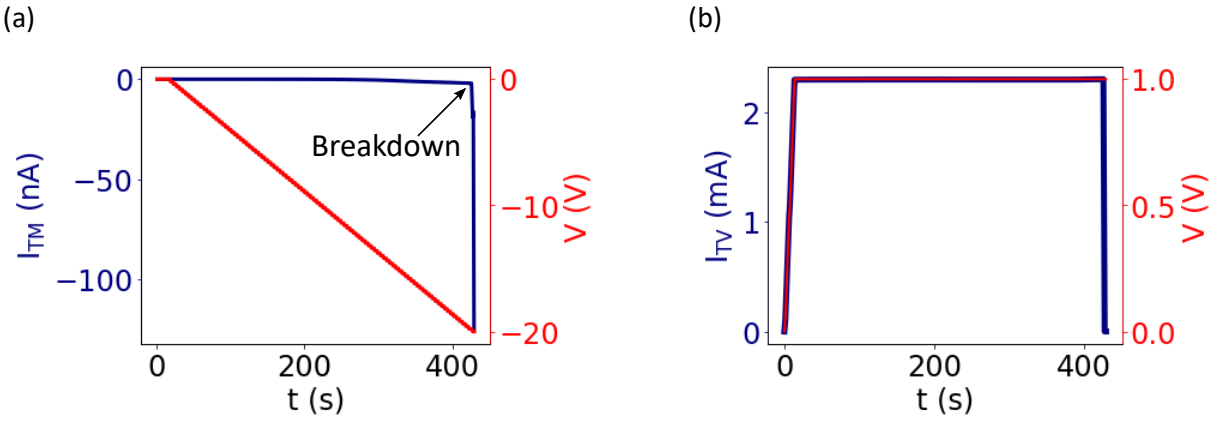


FIGURE 5.5: Measurement traces when performing CBD simultaneous to passing a large current density through an on-chip metal nanoconstriction. (a) The transmembrane current (i.e. measured between an on-chip electrode and an electrolyte solution in contact with the other side of the membrane) during CBD. (b) The transverse current (i.e. measured across the on-chip nanoconstriction) during CBD.

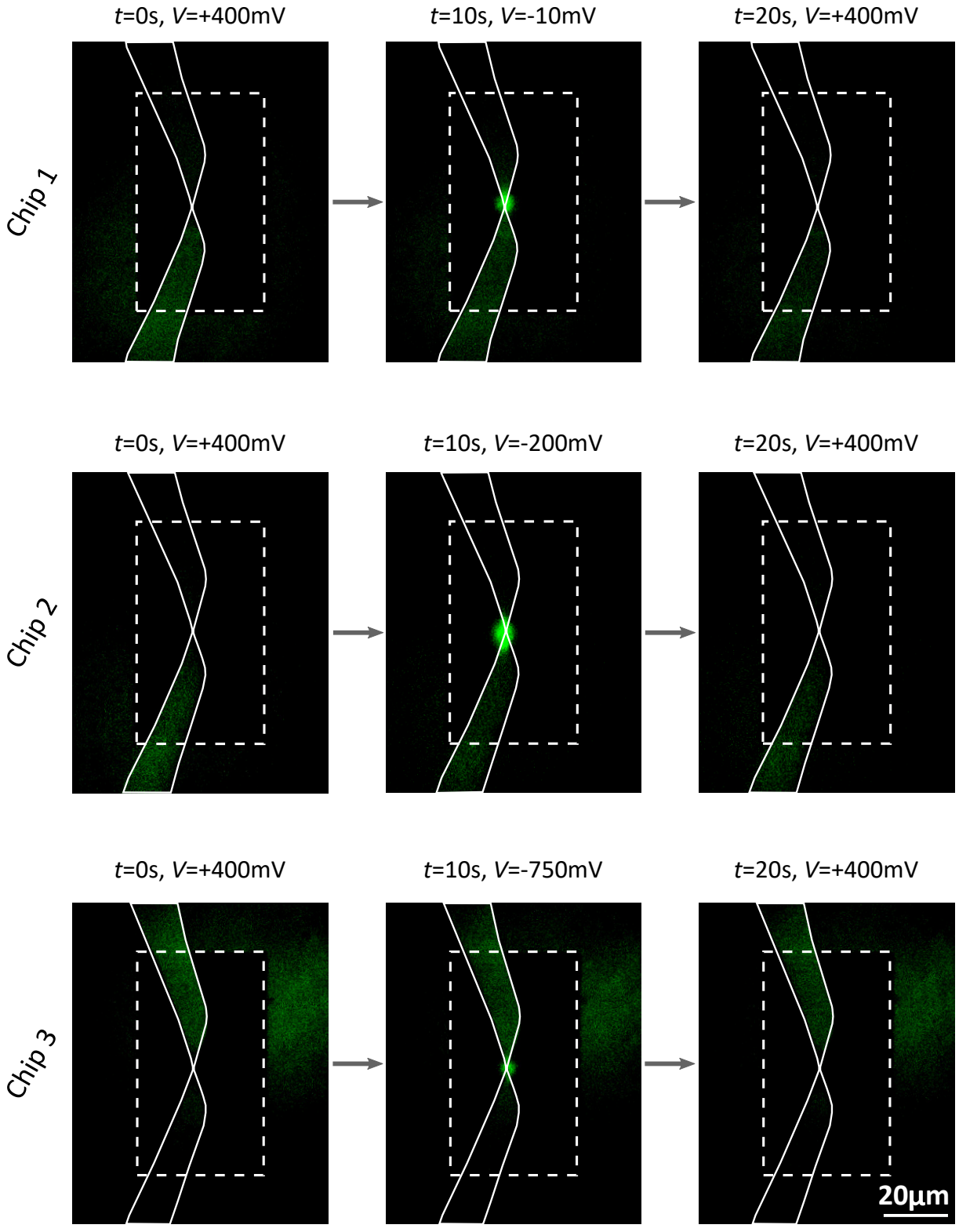


FIGURE 5.6: Fluorescence micrographs of nanopores created when performing CBD simultaneous to passing a large current density through an on-chip metal nanoconstriction. Data is shown for three separate chips. The dashed white box represents the edge of the suspended region of SiN_x while the solid white lines depict the electrode edges. For each chip, three micrographs are shown representing a time series of data with a frame before, during, and after the application of a voltage that drives Ca^{+2} ions through the nanopore.

with a frame before, during, and after the application of a voltage which drives Ca^{2+} ions through the nanopore. For each device, a single nanopore was formed at the narrowest region of the nanoconstriction. This result demonstrates that it is possible to create nanopores that are self-aligned with an on-chip metal nanoconstriction by passing a large current density through the electrodes to locally heat the membrane during CBD.

As discussed above, the current through the metal nanoconstriction drops to zero when breakdown occurs. This indicates that there is significant damage to the metal nanoconstriction during breakdown. To directly observe this damage, I have performed SEM imaging of the devices following CBD [Fig. 5.7]. For each device, the metal at the narrowest part of the constriction has been removed. This damage can extend up to several microns away from the narrowest part of the constriction. Such damage likely results after nanopore formation when the electrolyte solution comes into contact with the metal electrodes. When this occurs, there is temporarily a large voltage between the electrodes and the electrolyte solution which likely results in electrochemical etching of the metal. Damage to the nanoconstriction may be reduced by depositing a thin passivation layer over the electrodes via atomic layer deposition. A similar device geometry with a thin passivation layer over the metal electrodes was used in Chapter 4 where it was demonstrated that nanopores could successfully be created via CBD in these devices. Utilising a faster feedback (currently $\sim$10 Hz) to reduce the voltage after breakdown would also likely limit the damage to the electrodes. Indeed, both of these proposed methods to reduce damage to the metal nanoconstriction during CBD are currently being explored.

5.6 Other Potential Device Geometries

The results shown above are promising as they demonstrate that nanopores can be self-aligned with complementary on-chip electrodes via localised heating during CBD. However, due to time constraints, the potential of this technique was not able to be fully

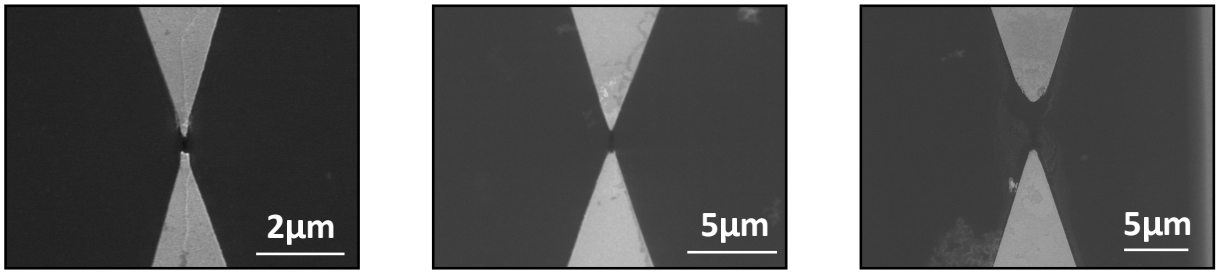


FIGURE 5.7: Scanning electron micrographs of damage to the metal nanoconstriction after performing CBD simultaneous to passing a large current density through the on-chip electrodes to provide localised Joule heating.

explored during this thesis. Indeed, there are likely many different device geometries that could exploit localised heating to enable the fabrication of nanopores self-aligned with on-chip nanostructures via CBD.

Firstly, it is noted nanopore devices with an embedded electrode (similar to the devices considered in Chapter 4) have been used to control the pore surface charge [121, 217–220]. This is a promising method to control the translocation dynamics of biomolecules. However, the full potential of the nanopore fabrication technique described above will likely be realised by integrating a nanopore with on-chip nanostructures that provide sensing modalities in addition to ionic current based detection. Below I discuss a few of the possible device geometries.

Field-Effect Sensors

Integration of nanopores with a field-effect sensor (alternatively called a field-effect transistor/FET) could be achieved using a similar device geometry to the metal nanoconstrictions discussed above [Fig. 5.8(a)]. However, instead of fabricating the nanoconstriction out of metal, a material that is sensitive to the local electric potential (such as graphene [64, 69] or MoS_2 [71]) would be used. Similar to the results discussed above, localised Joule heating of the membrane could be achieved by passing a large current density through the nanoconstriction [221]. Performing CBD simultaneous to Joule heating should then enable the formation of a nanopore self-aligned with the FET. As demonstrated in Chapter 4, this process could be performed repeatedly on a single membrane to fabricate high-density

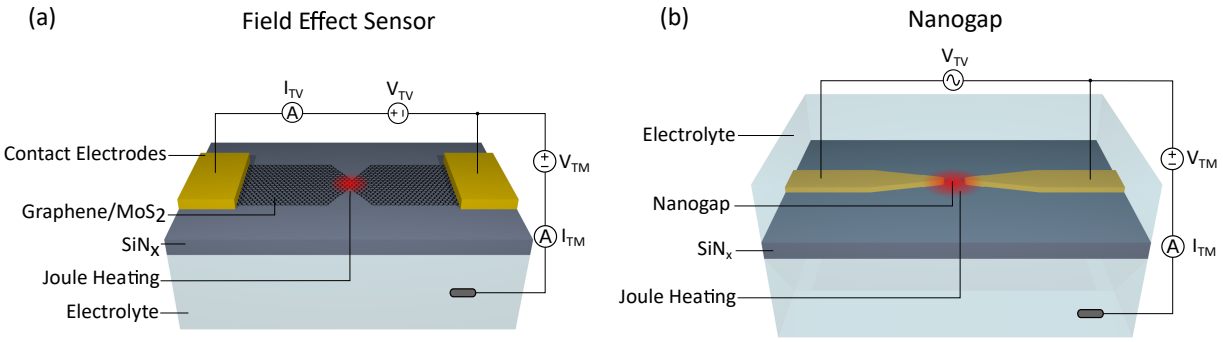


FIGURE 5.8: (a) Potential geometry that could be used for to create nanopores self-aligned with a field-effect sensor via CBD. (b) Potential geometry that could be used to create nanopores that are self-aligned with a nanogap via CBD.

arrays of nanopores self-aligned with FETs. The successful demonstration of this technique would overcome limitations associated with ionic current based sensing, including limited device densities [21] and low operating bandwidths [60].

In my opinion, this represents the most appealing future direction of the research shown in this thesis. This said, there are several challenges that will likely be faced when attempting to extend the CBD technique demonstrated above to integrate nanopores with FETs. In particular, the results shown above demonstrated that significant damage to the metal nanoconstriction can occur during breakdown. Such damage could likely be reduced by incorporating a thin (∼5 nm) passivation layer over the electrodes and employing faster feedback conditions. However, this will need to be confirmed in future studies to ensure that the on-chip electrodes remain functional after nanopore fabrication. Extending the CBD technique introduced here to fabricate nanopores in materials such as graphene and MoS_2 may also be challenging. Previous studies have demonstrated that it is possible to create nanopores in suspended graphene [174] and MoS_2 [189] films by applying a large electric field across the membrane via electrolyte solutions. While this is promising, the breakdown conditions required to fabricate a nanopore through SiN_x and a FET simultaneously will likely need to be optimised. It is also noted that breakdown could likely be performed with electrolyte on both sides of the membrane for these experiments. While this would remove the ability to independently fabricate multiple nanopores in the

membrane, it would make tracking the nanopore size during fabrication easier.

Nanogap Devices

Nanogaps between two electrodes have previously been integrated with nanopores to enable electron tunnelling [22, 72, 75] and RF [66] based sensing (see Sec. 1.3). The breakdown protocol required to integrate a nanopore with nanogap electrodes would need to be different to that discussed above for a nanoconstriction. One method to obtain local heating of the membrane would rely on applying an AC voltage across the nanogap when an electrolyte solution is present on both sides of the membrane. This would result in Joule heating of the electrolyte solution due to AC electrothermal heating (namely the movement of ions with the AC field) [222]. The largest increase in temperature would occur where the electric field is highest (i.e. between the nanogap electrodes) [68, 223]. Performing CBD simultaneous to Joule heating may then enable the formation of a nanopore that is self-aligned between the nanogap electrodes [Fig. 5.8(b)].

The method discussed above to localise nanopores between nanogap electrodes is clearly in the early stages of its conception as I am yet to perform measurements to demonstrate its feasibility. As with any new research project, several challenges would likely be faced if this method is pursued. One such initial concern relates to whether the heating can be sufficiently localised to ensure alignment with the nanogap. This might be difficult since convection heat flow may increase the temperature over a relatively large area (although dielectric loss heating of the SiN_x may also be explored to locally heat the membrane [224]). Regardless of this, the above discussion was not given to provide a steadfast method to fabricate nanopores integrated with nanogap electrodes. Rather, I have provided this discussion to highlight that localised heating can be obtained in many different nanoelectronic device geometries simply by applying appropriate electric fields. This demonstrates the versatility of the CBD approach introduced in this chapter.

5.7 Conclusion and Outlook

Here, I extended the CBD protocol introduced in Chapter 4 to enable the fabrication of nanopores self-aligned with on-chip nanoelectrodes. In particular, I demonstrated that passing a large current density through an on-chip metal nanoconstriction creates localised Joule heating of the membrane which confines nanopore formation to this region. Together with the results presented in the previous chapter, this is a promising technique to fabricate high density arrays of nanopores self-aligned with on-chip nanostructures.

Although this is not the first CBD technique that has demonstrated the ability to localise nanopore formation, the method demonstrated here does have several advantages over previous techniques. In particular, it has previously been demonstrated that nanopores can be localised to a nanoscale region by locally thinning the membrane [180] or by applying the electric field via a nanoscale electrode such as an AFM tip [182]. However, these techniques utilise relatively expensive equipment and would require time consuming alignment steps to integrate nanopores with on-chip nanostructures. It has also been demonstrated that focusing a laser on a plasmonic nanostructure during CBD creates at nanopore at the center of the plasmonic hotspot [188]. Outside of the results presented in this thesis, this is the only method that has used CBD to fabricate nanopores self-aligned with complementary nanostructures. However, this method still requires relatively complex optical equipment and only works for integrating nanopores with plasmonic nanostructures. The technique discussed in this chapter overcomes several of the limitations discussed above as it is (i) all electrical, (ii) doesn't require any alignment steps, and (iii) can be performed without any complex instrumentation.

Despite the promise of the CBD method introduced in this chapter, there is still significant research that must be done for this technique to reach its full potential. In particular, significant damage to the metal nanoconstriction was observed during CBD. It should be possible to minimise this damage by depositing a thin dielectric layer over the on-chip

electrodes and utilising faster feedback conditions. However, this will need to be demonstrated in future studies. Once this damage is minimised, it would be useful to perform TEM imaging of the pores to characterise the localisation provided by this technique with nanoscale resolution. Future studies should also look at extending this CBD technique to integrate nanopores with various on-chip nanostructures such as field-effect sensors and nanogap electrodes.

Chapter 6

Noise in Graphene Nanoelectronic Devices

In this chapter I discuss noise in graphene nanoelectronic devices with a view towards their use in single-molecule biosensing applications. These devices are fabricated via a feedback controlled electroburning technique where large current densities are passed through graphene resulting in the controlled removal of carbon atoms via oxidation/sublimation. These devices display normalised noise amplitudes 3-4 times larger than micron sized graphene electronic devices. Moreover, in some cases, this charge noise results in two-level fluctuations in the measured current. Studying the noise in these devices when measured in different environments (substrates and atmospheres) suggests that the noise is dominated by charge trapping at the graphene edges. The reported noise has important implications for the use of these devices for single-molecule biosensing applications.

Parts of this chapter have been published in Nanoscale [225]

6.1 Motivation

Over the past decade, nanoelectronic graphene devices have received attention for single-molecule biosensing applications. As discussed in Sec. 1.3, integrating graphene based field-effect sensors or tunnelling nanogaps with a nanopore has been proposed to increase the device density and bandwidth of these sensors [46, 64, 69, 70, 226]. The use of nanoelectronic graphene devices for single-molecule biosensing applications also extends beyond nanopore devices. In particular, graphene tunnelling nanogap devices have the potential to be exploited for a range of studies on the fundamental electronic properties of analytes by enabling the measurement of electron transport through single biomolecules [80, 83, 84, 86]. Nanoscale graphene field-effect sensors could also be developed for single-molecule biosensing similar to what has been demonstrated using carbon nanotube devices [227–229]. Such devices have been used to measure the dynamics and kinetics of single analytes with high temporal resolution for a range of fundamental biological studies.

Clearly, an important consideration for the development of graphene nanoelectronic devices for single-molecule biosensing is the noise in these devices. While there are many studies on the electronic noise characteristics of micron sized graphene devices [230], there are relatively few works on the observed noise when the device dimensions are shrunk down to a few nanometres as required for single-molecule biosensing applications. Moreover, any such studies have typically been performed at cryogenic temperatures and under high vacuum [231, 232]. A detailed study on the electronic noise in graphene nanodevices with dimensions on the order of a few nanometres will be an important step towards the development of these devices for single-molecule biosensing applications.

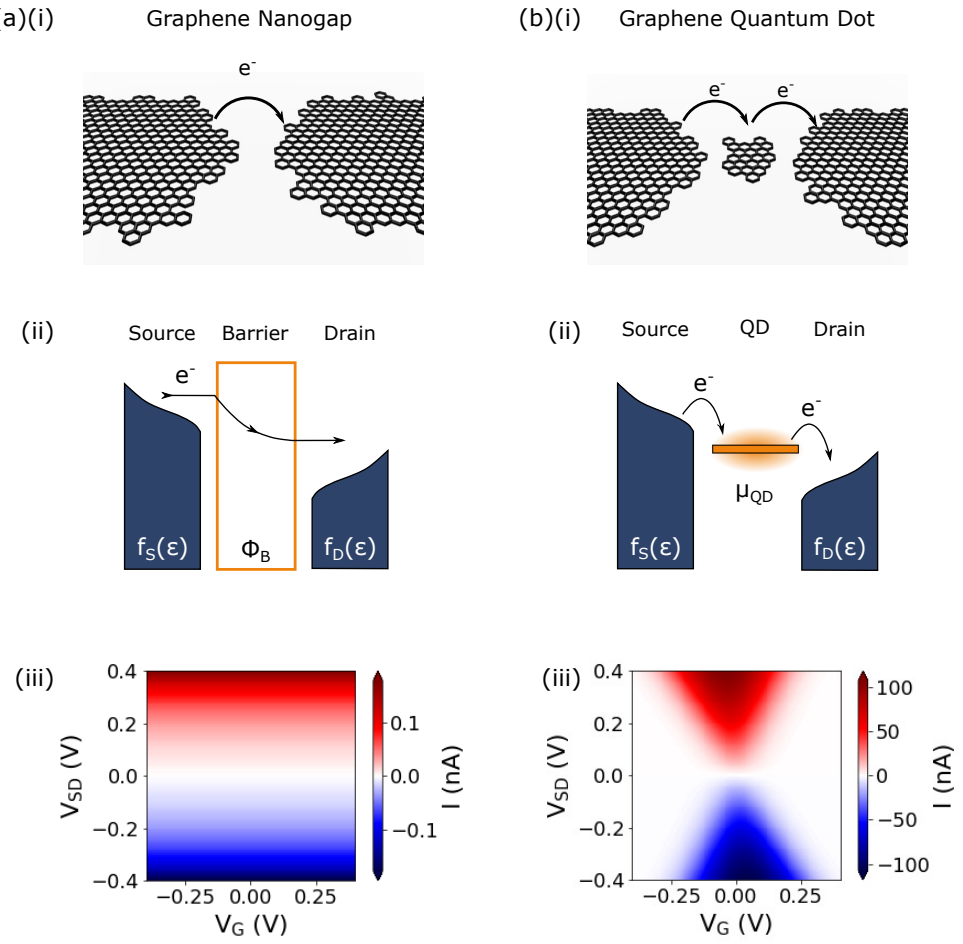


FIGURE 6.1: (a)(i) Schematic representation of a graphene nanogap device. (ii) Schematic representation of electron transport through a tunnelling nanogap. (iii) Calculated current as a function of the applied gate and source-drain voltage across a tunnelling nanogap. (b) Same as (a) but for a graphene quantum dot device rather than a graphene nanogap.

6.2 Electron Transport in Nanostructures

Before discussing the experimental results, it is necessary to introduce some basics on electron transport in graphene nanostructures. While this section will describe nanostructures made out of graphene, the electron transport characteristics are relevant for similar devices made of a range of materials.

Graphene Nanogaps

A schematic of this device geometry is shown in Fig. 6.1(a)(i). These devices consist

of graphene nanoelectrodes separated by a sub 5 nm gap. A current can be measured when a source-drain voltage is applied across the nanogap. This current relies on a quantum mechanical phenomenon called electron tunnelling whereby an electron can tunnel through a classically insurmountable barrier. A schematic of this phenomena is shown in Fig. 6.1(a)(ii) where an electron from a source electrode with Fermi distribution $f_S(\epsilon)$ tunnels through a classically insurmountable barrier, ϕ_B, to a drain electrode with a Fermi distribution $f_D(\epsilon)$.

The tunnelling current through a nanogap can be calculated based on the geometric and energetic properties of the system [233]. Equations for the tunnelling current through a nanogap are given in Appendix D. Figure 6.1(a)(iii) shows the current calculated through a 2 nm nanogap with a 1 eV tunnelling barrier as a function of the applied source-drain and gate voltage (the other parameters used to make this plot are given in Appendix D). Such a plot is usually referred to as a stability diagram. From the stability diagram, it is evident that the current is independent of the applied gate voltage.

Graphene Quantum Dots

A schematic of a graphene quantum dot (GQD) is shown in Fig. 6.1(b)(i). These devices consist of a graphene island separated from graphene electrodes via an energy barrier. The energy barrier is depicted as a physical gap in Fig. 6.1(b)(i), however this barrier could also result from electrostatic fields for example. The current through the quantum dot device is determined by electrons hopping to the energy levels of the quantum dot. This situation is represented in Fig. 6.1(b)(ii) which shows electrons hopping from a source electrode with Fermi distribution $f_S(\epsilon)$, to the energy level of the quantum dot (μ_{QD}) and then to the drain electrode with Fermi distribution $f_D(\epsilon)$.

The current through a quantum dot can be calculated by a rate equation model as outlined in Appendix E [234]. The rate constants for transport to and from the energy levels of the quantum dot can be calculated via a number of models. Rate constants calculated

via Marcus theory [234, 235] [Appendix E] are used throughout this work. The current calculated by the rate equation model as a function of source-drain voltage and gate voltage is shown in Fig. 6.1(b)(iii). Parameters used to calculate the rate constants for this figure are described in Appendix E.

Unlike graphene nanogap devices, the current through the quantum dot shows significant dependence on the gate voltage. This is because a gate voltage changes the energy levels of the quantum dot, aligning or misaligning them with the energy levels of the electrodes. In particular, a peak in the current at intermediate gate voltages is observed where an energy level of the quantum dot is aligned within the energy levels of the source and drain electrodes. This region is typically referred to as the resonant transport regime. The resonant transport regime is surrounded by regions of low current whereby the electrostatic energy required to add an electron to the quantum dot precludes electron transport. This region is known as Coulomb blockade.

6.3 Electroburning

Feedback controlled electroburning is the technique used in this chapter to fabricate graphene nanoelectronic devices. This technique can be used to create graphene nanogaps [236–238] and graphene quantum dots [239, 240]. Electroburning relies on passing a large current density (J $\sim$5x10^8 A/cm^2 [237]) through graphene to induce oxidation or sublimation of carbon atoms [238]. By reducing the current density quickly after the onset of electroburning, it is possible to controllably remove carbon atoms from the graphene lattice. Electroburning is an all electrical technique capable of rapid and automated device fabrication. However, as will be discussed below, it does possess several limitations which currently limits its applicability.

Several protocols for electroburning have been developed based on voltage ramps [237] and voltage pulses [238]. The protocol used in this work is described below. To begin with, a

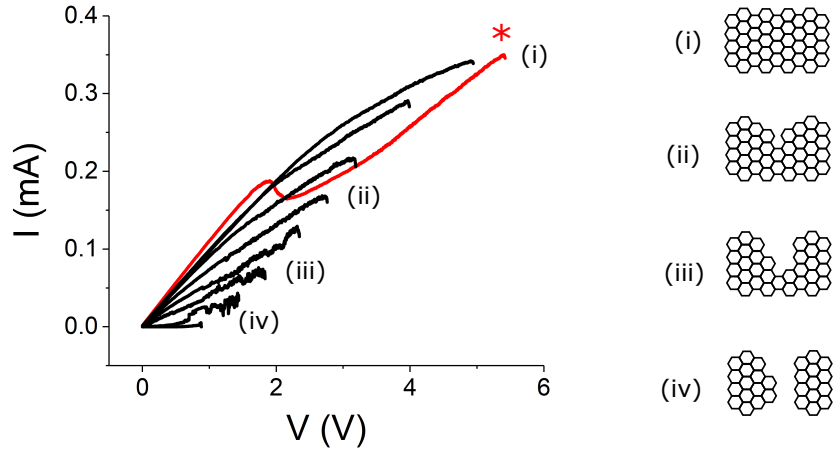


FIGURE 6.2: Current-voltage traces during electroburning cycles. The red curve is the first electroburning cycle. The red asterisk marks the onset of electroburning in this cycle. Subsequent cycles are shown in black. The schematics on the right illustrate the nanogap formation process at different stages of electroburning.

voltage ramp is applied across the graphene while measuring the current through the device [red curve in Fig. 6.2]. Large voltages across the device lead to high current densities and significant Joule heating of the graphene. This Joule heating can become so substantial that it causes oxidation or sublimation of carbon atoms from the graphene edges [238]. When this occurs, it leads to an increase in the device resistance and a corresponding drop in the current [asterisk in Fig. 6.2]. When a drop in the current is detected, the voltage is quickly ramped to zero to avoid catastrophic damage to the graphene. Repeating this process allows for the controlled removal of carbon atoms enabling the formation of graphene nanogaps and GQDs. Unfortunately, due to the stochastic nature of the electroburning process, the formation of either of these structures is largely random. However, the significant differences in the gate dependent electron transport through these structures (highlighted in Sec. 6.2) allows for discrimination between GQD and nanogap devices post electroburning. The majority of the work below will concentrate on results obtained for GQDs, however most of these results are also applicable to transport through graphene nanogaps.

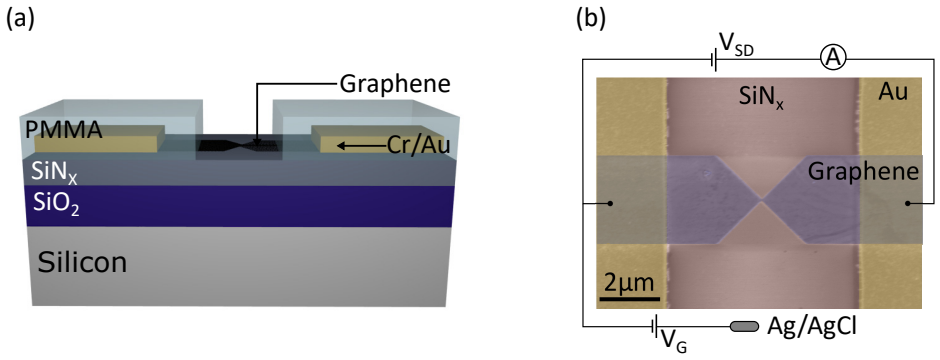


FIGURE 6.3: (a) Schematic of the device geometry. Note that SiN_x and SiO_2 layers are also present on the bottom of the device but are not shown for simplicity. (b) False-colour scanning electron micrograph of a device. The passivation layer is not imaged here due to charging issues.

6.4 Device Geometry and Measurement Setup

A schematic of the device geometry is shown in Fig. 6.3(a) while a false-colour scanning electron micrograph of a device is shown in Fig. 6.3(b). The devices were fabricated on a $SiN_x/SiO_2/Si$ substrate (thicknesses of each layer is 50 nm, 500 nm, and 300 μm respectively). Metal electrodes (5/95 nm Cr/Au) were then patterned on the membrane surface via photolithography. A graphene nanoconstriction with width ~100 nm at its narrowest region was patterned across two metal electrodes via electron beam lithography. Finally, a PMMA passivation layer was used to cover the metal electrodes to reduce Faradaic current when measuring these devices in electrolyte. Feedback controlled electroburning of the graphene constriction enables the formation of a GQD. The use of graphene nanoconstrictions (rather than a ribbon) ensures the current density is highest at the centre of the constriction enabling control over the position of the resulting GQD [237]. Each 1x1 cm^2 chip consists of 53 identical devices aligned along the centre of the chip while the metal electrodes extend to the chip edges. A detailed description of the fabrication procedure for these devices is provided in Appendix A.

To perform electroburning, a Femto DLPCA-200 current amplifier was used to measure the current. This amplifier has a variable gain of 10^3-10^{11} V/A allowing the measurement of the wide range of current values observed during the electroburning process (mA to

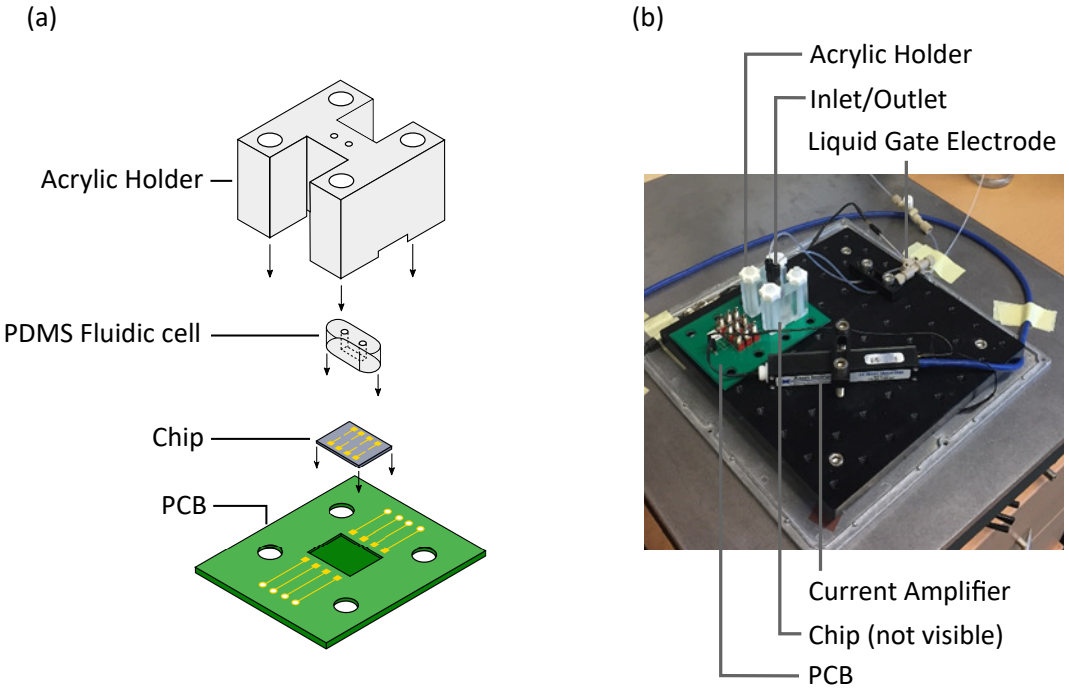


FIGURE 6.4: (a) Schematic of the custom-made flow cell used to measure graphene nanodevices in solution. (b) Photograph of the experimental setup used to measure graphene nanodevices in solution.

nA). An ADwin Gold II was used to apply the voltage across the graphene and digitise the measured current. This DAQ can process data at 300 MHz enabling the voltage to be quickly ramped to zero when electroburning is detected to avoid catastrophic failure of the device. Electroburning was performed using an automated probe station enabling the electroburning of the 53 devices on a chip to be completed within approximately one hour.

After electroburning, selected GQD devices are wire-bonded to a home-made PCB. The PCB allows for the bonding of 22 devices and switching between them. The PCB is also designed to be integrated with a custom-made flow cell. A schematic and photograph showing the integration of this flow cell with the PCB is shown in Fig. 6.4. The flow cell consists of a polydimethylsiloxane (PDMS) fluidic cell and an acrylic holder. The acrylic holder screws into a breadboard to align the PDMS fluidic cell with the chip. The acrylic holder also applies pressure between the chip and the PDMS to seal the channel. This is required since bonding of the PDMS to the chip using oxygen plasma treatment is not

possible as this will remove the graphene. The PDMS fluidic cell is connected to inlet and outlet tubing with the solution being delivered by an automated syringe pump. A Ag/AgCl electrode is placed upstream of the fluidic cell to control the potential of the solution, thus enabling liquid gating of the device.

To perform measurements of the electronic noise in these graphene nanodevices, the fluidic cell was filled with a 1 M aqueous KCl solution. A Faraday cage was then placed around the device to reduce electromagnetic noise during the measurements. Since the currents through the GQD are generally below 10 nA, an Axopatch 200B was used to measure the current. The resulting current was then digitised with a National Instruments data acquisition card (NI PCIe 6321). The source-drain voltage (V_{SD}) applied across the GQD and the gate voltage (V_G) applied to the electrolyte solution were both controlled using a 16 channel Stahl BS Series voltage source.

6.5 Liquid Gated Graphene Quantum Dots

Figure 6.5(a) shows the current through a GQD device as a function of V_{SD} and V_G. The data was obtained using the following protocol. First, V_G and V_{SD} were set to -400 mV and -200 mV respectively. A 2 s long current-time (I-t) trace low pass filtered at 10 kHz was then recorded (sampling frequency of 20 kHz). The voltage was then raster scanned along the gate voltage axis while measuring 2 s long I-t traces at each voltage. Steps in V_{SD} and V_G are 25 mV. The mean current from each I-t trace corresponds to each pixel in Fig. 6.5(a).

As discussed in Sec. 6.2, the data shown in Fig. 6.5(a) is typical of sequential electron transport through a GQD. Namely, a region of resonant electron transport is observed where one of the energy levels of the quantum dot is aligned within the energy levels of the electrodes. This is surrounded by regions of Coulomb blockade where the electrostatic energy required to add an electron to the quantum dot precludes electron transport.

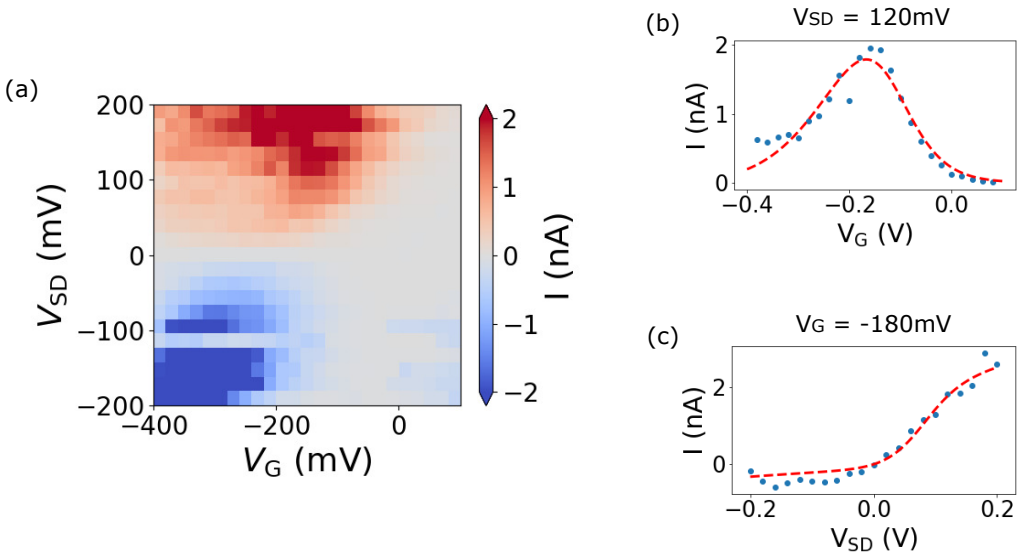


FIGURE 6.5: (a) Average current measured through the GQD as a function of V_{SD} and V_G. (b) Current as a function of gate voltage for V_{SD}=120 mV. (c) Current as a function of source-drain voltage for V_G=-180 mV. The red lines in (b) and (c) are fits to the rate equation discussed in Appendix E.

Note, it is not trivial to observe Coulomb blockade at room temperature. For this to be observed, the energy required to add an electron to the quantum dot must be greater than the thermal energy. At room temperature, the thermal energy is ∼26 meV which requires the dimensions of the quantum dot to be on the order of a few nanometres [239]. This cannot be obtained using most conventional top-down lithography techniques.

Figures 6.5(b) and (c) show slices through the stability diagram for a given V_{SD} and V_G respectively. Fits to the data based on the rate equation model discussed in Appendix E are shown by the red curve. A slight deviation from the fit at large negative voltages is likely due to the presence of Faradaic current here. As such, the discussion below will concentrate on data obtained for -0.3V≤V_G≤0.1V. These fits will be used below when analysing the noise in these devices. The fits also provide estimates for the ratio of the capacitive coupling to the source (C_S), drain (C_D) and gate (C_G) electrodes. The ratios obtained are C_S/C_G=0.36 and C_D/C_G=0.16. Different values of C_S and C_D likely result from asymmetries in the graphene electrodes contacting the quantum dot due to the probabilistic nature of the electroburning process. The large gate capacitance in these

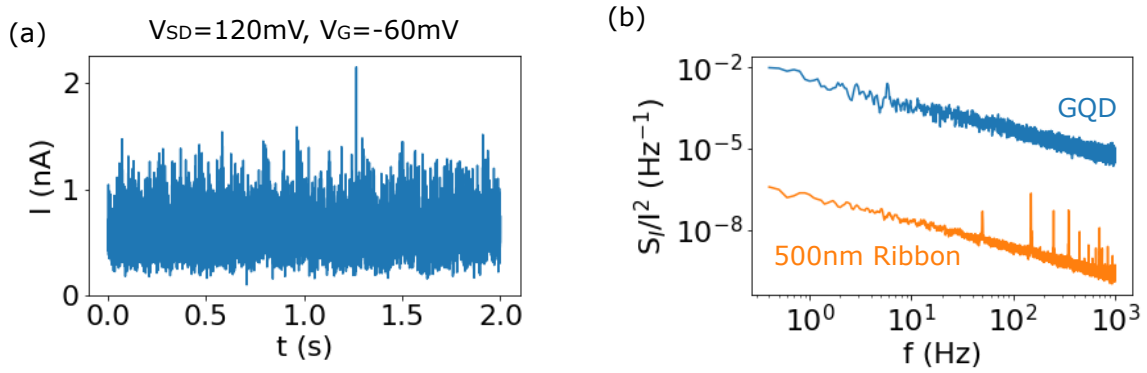


FIGURE 6.6: (a) An *I*-*t* trace for V_{SD}=120 mV and V_G=-60 mV. (b) Normalised noise spectrum of the current through a graphene quantum dot (blue) and a 500 nm wide, 10 μm long graphene ribbon (orange).

devices is due to the short electrochemical double layer in this system (Debye length λ ~0.3 nm in 1 M KCl) and results in the gate electrode being closely coupled to the energy level of the quantum dot.

6.6 Charge Noise in Graphene Quantum Dots

Fig. 6.6(a) shows an example *I*-*t* trace for V_{SD}=120 mV and V_G=-60 mV. The corresponding normalised noise spectrum of the *I*-*t* trace is shown in Fig. 6.6(b). A $1/f$ noise spectrum ubiquitous with nanoscale electronic devices is observed. The normalised noise spectrum for the current through a 10 μm long, 500 nm wide graphene ribbon is also shown in Fig. 6.6(b). The normalised noise in the GQD is ~4 orders of magnitude larger than in the 500 nm wide ribbon. The noise in 30 nm wide graphene ribbons has also been reported to be ~3 orders of magnitude lower than shown here for a GQD [241]. This result highlights the dramatic increase in the normalised noise magnitude when shrinking the device dimensions down to a few nanometres as done in this study.

Previous studies on quantum dots [231, 242] (as well as graphene ribbons [243] and carbon nanotubes [244]) have reported that the electrical noise scales with the magnitude of the transconductance (i.e. $|dI/dV_G|$). This result implies charge noise is dominant in

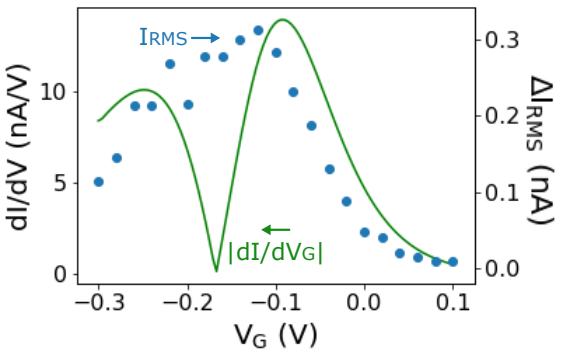


FIGURE 6.7: The measured RMS noise (blue dots, right axis) and the calculated transconductance (green line, left axis) as a function of V_G for V_{SD}=120 mV. The transconductance is calculated based on the fits to the rate equation model.

these devices. In particular, charge fluctuations in the local environment act to change the gate potential resulting in noise in the device. Figure 6.7 plots the measured RMS noise (ΔI_{RMS}) and the magnitude of the transconductance as calculated from the fits to the rate equation for V_{SD}=120 mV. Notably, the measured noise doesn't scale with the transconductance, a result that is particularly evident at the centre of the resonant transport regime. It is postulated that this is because charge fluctuations also act to change the source-drain potential. Indeed, below it will be shown that the measured noise can be replicated by adding fluctuations in V_{SD} as well as V_G.

To show that the measured noise can be described by adding fluctuations in V_{SD} and V_G, simulated I-t traces were created. Namely, using the fits to the rate equation described above, the current at any given source-drain and gate voltage can be calculated as $I(V_{SD},V_G)$. For a given fluctuation in the source-drain (ΔV_{SD}) and gate voltage (ΔV_G) the current can also be calculated as $I(V_{SD}+\Delta V_{SD},V_G+\Delta V_G)$. It is assumed ΔV_{SD} and ΔV_G have a $1/f$ spectrum with a Gaussian distribution. A simulated I-t trace was created by calculating the current for 5000 consecutive fluctuations in V_{SD} and V_G. As shown in Fig. 6.8(a) it is found that a standard deviation of potential fluctuations in V_{SD} and V_G of 13 mV reproduces the measured noise quite well.

In GQDs, the current depends non-linearly on V_{SD} and V_G. One result of this is that

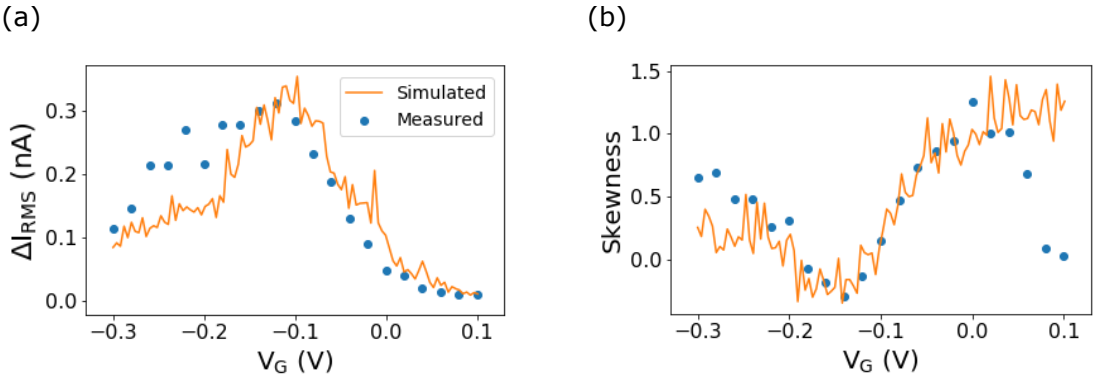


FIGURE 6.8: (a) Measured (blue dots) and simulated (orange line) RMS noise as a function of V_G for V_{SD}=120 mV. (b) Measured and simulated skewness of the I-t traces as a function of V_G for V_{SD}=120 mV.

symmetric fluctuations in V_{SD} and V_G lead to asymmetry in the I-t traces. Such asymmetry can be seen in the I-t trace shown in Fig. 6.6(a) where the distribution is skewed towards larger current values. The skewness (g_1) of a distribution can be quantified as $g_1 = m_3/m_2^{3/2}$ where m_r is the r^{th} moment about the mean and can be calculated for a distribution of N points with values x_i as $m_r = 1/N \sum(x_i - \bar{x})^r$ [245]. A skewness of zero indicates a symmetric distribution, while a skewness greater/smaller than zero indicates there is more weight towards higher/lower current values.

Figure 6.8(b) plots the skewness of the measured I-t traces as a function of V_G for V_{SD}=120 mV. Also shown is the skewness for the simulated traces which closely reproduces the measured data across the range of applied V_G (except at high V_G where the current approaches zero and the noise of the measurement system starts to dominate). The need to incorporate fluctuations in V_{SD} is again highlighted by considering the skewness in the I-t traces. In particular, when operating at the centre of the resonant transport regime, fluctuations in V_G would result only in negative changes in the current. In reality, a skewness close to zero is measured here since fluctuations in V_{SD} also contribute strongly to the noise. This analysis of the skewness in the I-t traces hasn't been considered before in previous studies on similar systems [231, 242–244, 246]. As demonstrated above, analysing the skewness of the I-t traces is another useful tool for isolating contributions to the observed noise, especially in non-linear systems such as the GQD considered here.

6.7 Random Telegraph Noise

An important observation of the observed noise is that, in some cases, two-level fluctuations (TLFs) in the current level are observed. These signals also result from the charge fluctuations described above, however, in this case the fluctuators are presumably very close to the GQD. To my knowledge, TLFs have not previously been reported in graphene nanoelectronic devices at room temperature. Since charge fluctuators are generally thermally activated [246], operating graphene devices at room temperature usually results in sampling a large number of fluctuators. However, given the device dimensions in this study are on the order of a few nanometres, a relatively small number of fluctuators are sampled, even at room temperature.

Figure 6.9(a) shows examples of observed TLFs in the current level through a GQD. The presence of TLFs are perhaps most easily observed in the corresponding histograms of the current level shown to the right of each I-t trace. Changing the applied V_G modifies the proportion of time spent in the high and low current states. In particular, for V_G=-360 mV [Fig. 6.9(a)(i)] the current is predominately in the high state, for V_G=-320 mV [Fig. 6.9(a)(ii)] the current is almost evenly split between the high and low states, while for V_G=-240 mV the current is predominately in the low state. The time spent in the high and low current states can be estimated by fitting two skewed Gaussian distributions to the peaks observed in the I-t histograms and integrating the area under each curve. The calculated proportion of time spent in the high and low current states is shown in Fig. 6.9(b). The proportion of time spent in the high state clearly decreases with increasing V_G, demonstrating the ability to tune the occupation of individual charge traps via the application of a gate voltage.

In some cases, remarkably large two-level fluctuations in the current level are observed. An example of this is shown in Fig. 6.9(c) where the current spikes are $\sim$10 times larger than the baseline current value. The duration of these current spikes has an exponential

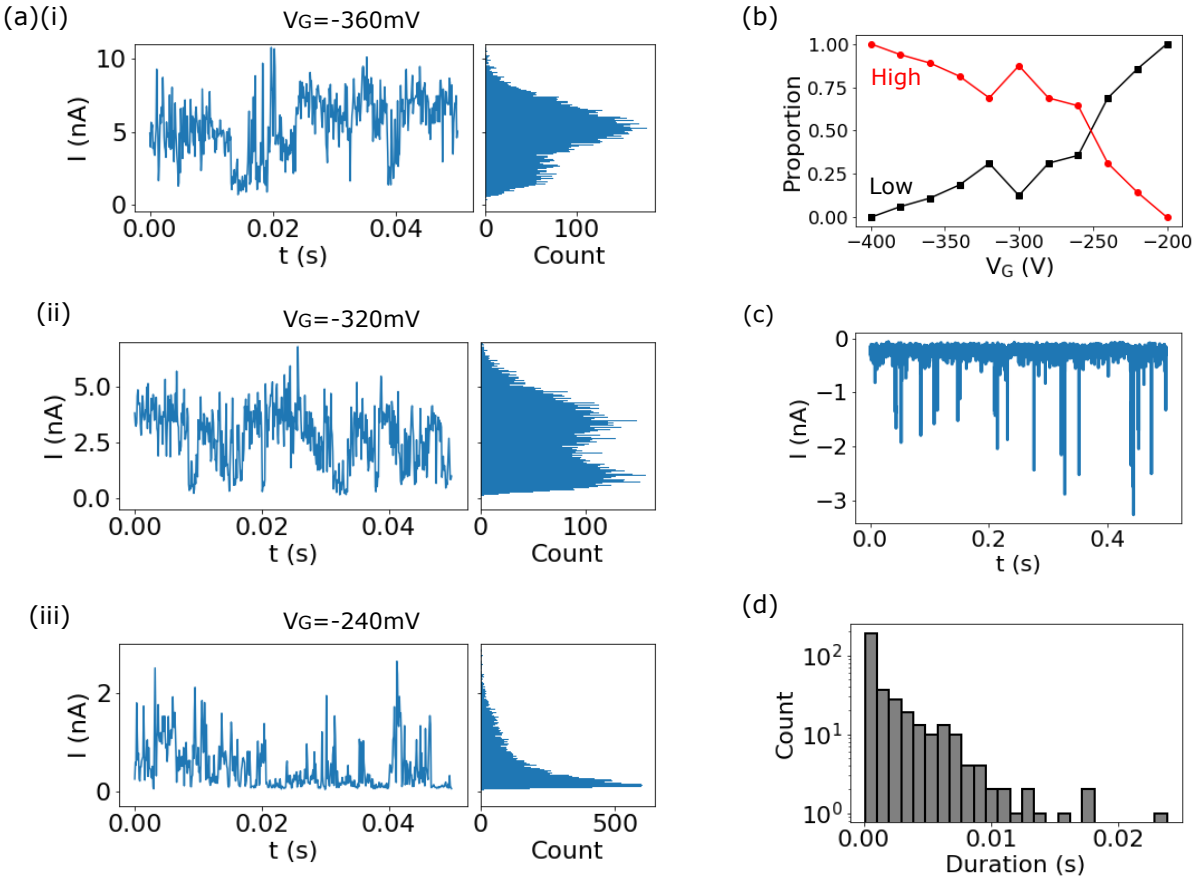


FIGURE 6.9: (a) Example *I*-*t* traces demonstrating two-level fluctuations in the current and the corresponding histograms of the current values. Traces were recorded at V_{SD}=200 mV and (i) V_G=-360 mV, (ii) V_G=-320 mV and (iii) V_G=-240 mV. (b) Change in the occupation of the high and low current states as a function of gate voltage. (c) Example *I*-*t* trace showing sharp spikes in the current level. (d) The distribution of the duration of the current spikes shown in (c).

distribution with a time constant of τ ~0.63 ms [Fig. 6.9(d)]. Importantly, these signals are very similar to the signals that are observed in many single-molecule biosensing experiments (e.g. from translocation of a biomolecule through a nanopore) [69, 227, 228]. The presence of these two-level fluctuations in the current level will therefore need to be carefully considered if nanoelectronic graphene devices are to be developed for single-molecule biosensing applications.

6.8 Noise in Different Environments

To try and understand the source of the charge noise discussed above, I have measured the noise from GQDs in different environments (atmosphere and substrate). Namely, I have compared the noise in a graphene quantum dot measured on: (i) a SiN_x substrate in 1 M KCl (as described above), (ii) a SiN_x substrate in air, and (iii) a HfO_2 substrate in air. To compare the low-frequency noise amplitude for each of these geometries, I have measured *I*-*t* traces across a range of applied source-drain and gate voltages. The value of the normalised noise spectrum at 500 Hz is then used to quantify the amplitude of the low-frequency noise. Only *I*-*t* traces where the absolute value of the mean current is greater than 0.25 nA are considered to ensure that the noise from the GQD is dominant (rather than the amplifier noise). Figure 6.10 shows histograms of the values of the normalised noise spectrum extracted at 500 Hz for the three device geometries described above. The distributions in the noise magnitudes are relatively similar independent of the atmosphere or the substrate (any differences in the distributions are likely explained by device-to-device variability). This results suggests that the observed charge noise does not originate from the environment, but is rather intrinsic to the graphene nanodevice itself.

The result that the observed noise is largely independent of environment is consistent with a previous study that measured the noise in GQDs at cryogenic temperatures under vacuum [231]. Here, it was demonstrated that the charge noise in suspended graphene quantum dots is the same as graphene quantum dots supported by a substrate. As such, it was suggested that the observed noise originates from charge trapping at the disordered graphene edges. This explanation is also consistent with a previous study that used scanning noise microscopy to demonstrate that the charge noise at the edges of a graphene domain is orders of magnitude larger than the charge noise far away from the domain boundary [247]. Given the above results, it thus seems likely that charge trapping at the disordered graphene edges also dominates the noise in our devices. However,

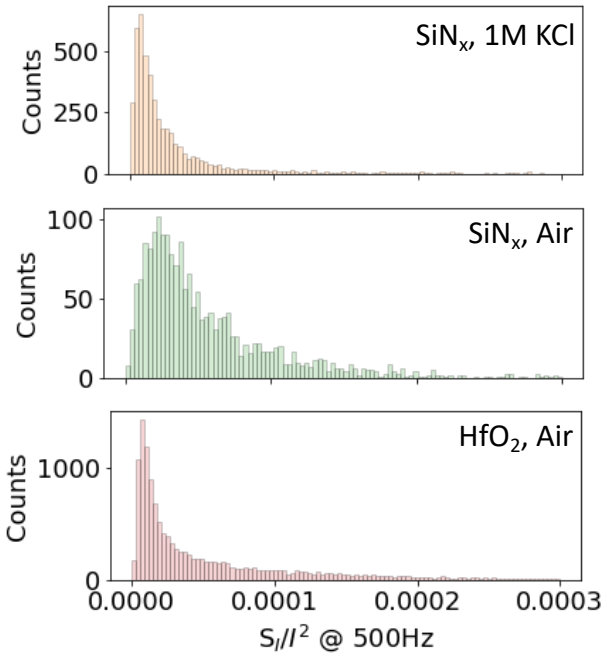


FIGURE 6.10: Comparison of the normalised noise spectrum at 500 Hz for a graphene quantum dot on a SiN_x substrate in 1 M KCl (top), a SiN_x substrate in air (middle), and a HfO_2 substrate in air (bottom). Measurements are performed across a range of source-drain and gate voltages. Only I-t traces with an average absolute current value greater than 0.25 nA are considered since the low-frequency noise dominates for such measurements.

noise originating from the graphene surface or the graphene substrate interface cannot be discounted from our measurements.

6.9 Outlook For Single Molecule Biosensing Applications

As discussed at the start of this chapter, the ultimate goal of this study was to develop graphene nanoelectronic devices fabricated by feedback controlled electroburning for single-molecule biosensing applications. I will therefore now discuss some of the implications of the observed noise for such applications. Several different device geometries and sensing modalities that have been envisioned for single-molecule biosensing using graphene nanodevices are discussed.

Molecule Binding Nearby a GQD

First, consider the case of a charged analyte binding close to a GQD. The charged molecule changes the local electric potential which results in a change in the current through the GQD. This approach is very similar to single-molecule field-effect sensing that has been demonstrated with carbon nanotubes [227–229, 248, 249].

To determine the limitations of the observed noise for such a sensing approach a simple calculation was carried out. Namely, the electric potential as a function of distance, r, from the base of a 20 base pair strand of dsDNA to a point in the plane perpendicular to DNA is calculated [inset to Fig. 6.11(a)]. For simplicity, the dsDNA is assumed to be rigid and consist of 20 point charges of charge $-2e$ separated by 0.34 nm. The electric potential is calculated by summing the potential from each point charge, i.e. $\Delta V = \sum Q/4\pi\epsilon_0\epsilon_r r'$ where Q is the charge, ϵ_0 is the permittivity of free space, ϵ_r is the relative permittivity of the environment and r' is the distance to the point charge. The calculation is carried out for a deionised water environment and screening effects are neglected. To obtain a change in the electric potential three times larger than the charge noise observed in

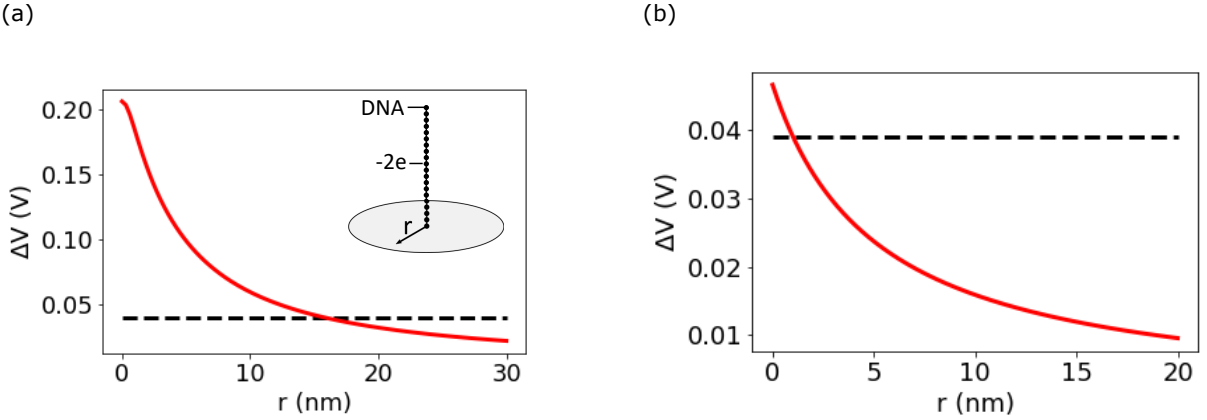


FIGURE 6.11: (a) Plot of the change in potential as a function of distance from the base of a 20bp strand of dsDNA (assumed to be rigid and consist of 20 point charges of charge -2e). The inset shows a schematic of the calculation. (b) Change in potential as a function of distance away from a nanopore due to the translocation of an analyte through the pore. Parameters used for these calculations are given in the text. The black dashed lines show the threshold required to obtain a signal-to-noise ratio greater than three.

GQDs, the dsDNA must be within ∼16 nm of the quantum dot [Fig. 6.11(a)]. However, this distance would be reduced if screening effects in electrolyte solutions were taken into account. Previous studies have non-covalently functionalised carbon nanostructures with biomolecules using a pyrene-NHS ester molecule [250]. For DNA functionalisation, this strategy has led to an average spacing between molecules of ∼25 nm [251]. As such, it seems unlikely that a sufficient signal-to-noise ratio will be obtainable for this sensing modality.

Integrating a GQD with a Nanopore

GQD devices could also be integrated with nanopores for biosensing applications. Here, changes in the local electric potential result when the nanopore is blocked by a translocating analyte. The change in electric potential (ΔV) when a biomolecule blocks a pore can be calculated as [21]:

$$\Delta V \approx \frac{2VA(4l+d)(C_{cis}/C_{trans}-1)}{\pi \ln(C_{cis}/C_{trans})(2l+d)(d^2(C_{cis}/C_{trans}-1)+4r(2l+d))} \tag{6.1}$$

where V is the transmembrane potential, A is the cross-sectional area of the translocating molecule, l is the length of the pore, d is the pore diameter, $C_{cis/trans}$ are the electrolyte concentrations in the *cis* and *trans* chambers respectively, and r is the distance to the nanopore. Using this equation, the potential change as a function of distance to the nanopore can be obtained. Parameters to optimise the change in the local electric potential are used with V=0.5 V, A=π nm^2, l=20 nm, d=3 nm and C_{cis}/C_{trans}=100. To obtain a change in the voltage greater than three times the standard deviation of the charge noise observed in GQDs, the nanopore must be within ∼1 nm of the quantum dot [Fig. 6.11(b)]. Such alignment would likely be very difficult to obtain.

Tunnelling Based Sensing

The electroburning technique discussed here can also be used to create graphene nanogaps [236]. These devices have received interest for single-molecule biosensing applications. Here, sensing is accomplished by detecting changes in the tunnelling current between the nanoelectrodes as a molecule enters the gap. Such devices could be integrated with nanopores or used as stand-alone single-molecule biosensors.

One of the major issues in developing such biosensing devices using the electroburning technique discussed here is the low yield of graphene nanogaps. Previous studies have demonstrated that >70% of electroburnt devices yield GQDs [240]. The ratio of graphene nanogap devices created via electroburning would therefore likely need to be increased by modifying the fabrication process if these devices are to be successfully used for tunnelling based single-molecule biosensing. A more promising method to fabricate sub 10 nm graphene nanogaps using dashed line lithography has been reported [252]. Indeed, using this technique, single-molecule biosensing of amino acid binding dynamics has been reported [253]. The charge noise discussed in this chapter will still be of importance for such studies. In particular, care will need to be taken during such measurements as typical single-molecule biosensing signals are very similar to two-level fluctuations resulting from charge noise reported in this chapter.

The integration of graphene nanogaps fabricated via electroburning with a nanopore [226] presents several more issues. In particular, the nanopore will need to be aligned with the graphene nanogap with almost nanometre precision. While this may be possible using a transmission electron microscope to create the pore, using such equipment would severely limit the high throughput nature of the electroburning process (which is its main attraction). Moreover, TEM drilling of nanopores after electroburning would likely damage the graphene nanogap. Results from within our group have also demonstrated that electroburning can result in significant damage to suspended SiN_x substrates due to

extreme heating [68]. As such, it will likely be difficult to use the electroburning technique discussed here to create graphene nanogaps integrated with nanopores.

6.10 Conclusion and Outlook

In this chapter I studied electronic noise in graphene nanodevices fabricated via feedback controlled electroburing. I demonstrated that these devices show extremely large normalised noise amplitudes (3-4 magnitudes larger than that observed in micron sized graphene devices). The observed noise can be described by a charge noise model by incorporating fluctuations in the source-drain and gate voltages. In some cases, the observed noise can even result in two-level fluctuations in the current level. Lastly, by measuring devices in different environments (i.e. atmosphere and substrate), I suggested that the observed noise results from charge trapping at the disordered graphene edges.

Based on the results demonstrated in this chapter, it will likely be difficult to use graphene nanoelectronic devices fabricated via feedback controlled electroburning for single-molecule biosensing applications. This is largely because the large amplitude charge noise places an unrealistic requirement on the alignment needed between the biomolecule and the graphene nanostructure. A more promising path to developing these devices utilises graphene nanogaps fabricated via dashed line lithography. Such devices display no appreciable current until a biomolecule is present within the gap. However, the results presented here will still be of importance for such devices since, when a biomolecule is within the gap, the observed charge noise may obscure the signal from the analyte.

Chapter 7

Summary

This thesis focused on the fabrication of single-molecule nanoelectronic biosensors via electrical breakdown techniques. These fabrication techniques are rapid, low cost, and can be fully automated making them widely accessible to the community. A large part of this thesis looked at developing CBD techniques to fabricate nanopores integrated with on-chip nanostructures. Such on-chip nanostructures have received interest for nanopore sensing as they can be used to enhance the capabilities of these devices. This thesis also analysed the potential of graphene nanoelectronic devices fabricated via feedback controlled electroburning for single-molecule biosensing applications. Here, a particular focus was given to the noise properties in these devices.

After providing a background on solid-state nanopores with a focus on fabricating these devices via CBD, the first research results of this thesis were given in **Chapter 3**. Here, I studied the mechanism of electrical conduction and nanopore formation during CBD. In particular, I demonstrated that depending on the SiN_x stoichiometry, conduction is limited by either oxidation reactions that must occur at the membrane-electrolyte interface (Si-rich SiN_x) or charge transport through the dielectric (stoichiometric SiN_x). Several important practical implications from understanding this process were provided which

proved to be crucial for extending CBD to fabricate nanopores with on-chip electrodes in the following chapters.

Next, **Chapter 4** introduced a new CBD protocol that enabled the independent fabrication of multiple nanopores in a single membrane. This technique relied on applying the breakdown voltage between an on-chip electrode and an electrolyte solution in contact with the other side of the membrane. Importantly, in this CBD configuration, electrolyte is only present on one side of the membrane. This enables the independent fabrication of multiple nanopores, since previously created pores will not be expanded during each new breakdown event.

In **Chapter 5** I extend the CBD technique introduced in the previous chapter to self-align nanopores with on-chip nanostructures. In particular, I demonstrated that passing a large current density through an on-chip metal nanoconstriction leads to localised heating of the membrane which confines nanopore formation to this region. This is a simple, cost effective, and accessible method to fabricate nanopores integrated with on-chip nanostructures.

Lastly, in **Chapter 6**, I explored the use of graphene nanoelectronic devices fabricated via a feedback controlled electroburning technique for single-molecule biosensing applications. I demonstrated that these devices display large amplitude charge noise (normalised amplitude is 3-4 orders of magnitude larger than micron sized graphene devices). In some cases, this charge noise results in two-level fluctuations in the current level. Such charge noise will likely limit the development of these devices for single-molecule biosensing applications.

Much of this thesis was focused on developing accessible techniques to integrate nanopores with complementary on-chip nanostructures. Nanostructures that have been integrated with nanopores include field-effect sensors, tunnelling nanogaps, and plasmonic nanodevices. While there has been plenty of interest in these devices, to date their full potential

has yet to be explored. This has largely been due to the complex fabrication procedures required to create these devices. This is particularly the case for nanopores integrated with field-effect sensors and nanogaps whereby it has often been reported that only a handful of devices are successfully fabricated after years of research [64, 75]. As such, it has been almost impossible to explore the intrinsic capabilities of these devices. The accessible fabrication techniques presented here are hopefully a step towards researchers being able to fully explore the capabilities of these devices. Only then will it become apparent whether nanopores integrated with on-chip nanostructures can be used for their array of proposed applications.

Bibliography

[1] Nikhil Bhalla, Pawan Jolly, Nello Formisano, and Pedro Estrela. Introduction to biosensors. *Essays in Biochemistry*, 60(1):1–8, jun 2016.

[2] Daniel Quesada-González and Arben Merkoçi. Nanomaterial-based devices for point-of-care diagnostic applications. *Chemical Society Reviews*, 47(13):4697–4709, 2018.

[3] Namik Akkilic, Stefan Geschwindner, and Fredrik Höök. Single-molecule biosensors: Recent advances and applications. *Biosensors and Bioelectronics*, 151:111944, mar 2020.

[4] Yu Li, Lihua Zhao, Yuan Yao, and Xuefeng Guo. Single-molecule nanotechnologies: An evolution in biological dynamics detection. *ACS Applied Bio Materials*, 3(1):68–85, dec 2019.

[5] Jacob K. Rosenstein, Serge G. Lemay, and Kenneth L. Shepard. Single-molecule bioelectronics. *Wiley Interdisciplinary Reviews: Nanomedicine and Nanobiotechnology*, 7(4):475–493, dec 2014.

[6] Elizabeth A Manrao, Ian M Derrington, Andrew H Laszlo, Kyle W Langford, Matthew K Hopper, Nathaniel Gillgren, Mikhail Pavlenok, Michael Niederweis, and Jens H Gundlach. Reading DNA at single-nucleotide resolution with a mutant MspA nanopore and phi29 DNA polymerase. *Nature Biotechnology*, 30(4):349–353, mar 2012.

[7] Gerald M Cherf, Kate R Lieberman, Hytham Rashid, Christopher E Lam, Kevin Karplus, and Mark Akeson. Automated forward and reverse ratcheting of DNA in a nanopore at 5a precision. *Nature Biotechnology*, 30(4):344–348, feb 2012.

[8] J. Eid, A. Fehr, J. Gray, K. Luong, J. Lyle, G. Otto, P. Peluso, D. Rank, P. Baybayan, B. Bettman, A. Bibillo, K. Bjornson, B. Chaudhuri, F. Christians, R. Cicero, S. Clark, R. Dalal, A. deWinter, J. Dixon, M. Foquet, A. Gaertner, P. Hardenbol, C. Heiner, K. Hester, D. Holden, G. Kearns, X. Kong, R. Kuse, Y. Lacroix, S. Lin, P. Lundquist, C. Ma, P. Marks, M. Maxham, D. Murphy, I. Park, T. Pham, M. Phillips, J. Roy, R. Sebra, G. Shen, J. Sorenson, A. Tomaney, K. Travers, M. Trulson, J. Vieceli, J. Wegener, D. Wu, A. Yang, D. Zaccarin, P. Zhao, F. Zhong, J. Korlach, and S. Turner. Real-time DNA sequencing from single polymerase molecules. *Science*, 323(5910):133–138, jan 2009.

[9] Laura Restrepo-Pérez, Chirlmin Joo, and Cees Dekker. Paving the way to single-molecule protein sequencing. *Nature Nanotechnology*, 13(9):786–796, sep 2018.

[10] Rui Hu, Xin Tong, and Qing Zhao. Four aspects about solid-state nanopores for protein sensing: Fabrication, sensitivity, selectivity, and durability. *Advanced Healthcare Materials*, 9(17):2000933, jul 2020.

[11] Yanfang Wu, Danielle Bennett, Richard D. Tilley, and John Justin Gooding. How nanoparticles transform single molecule measurements into quantitative sensors. *Advanced Materials*, 32(18):1904339, sep 2019.

[12] Yanfang Wu, Richard D. Tilley, and J. Justin Gooding. Challenges and solutions in developing ultrasensitive biosensors. *Journal of the American Chemical Society*, 141(3):1162–1170, nov 2018.

[13] Jasper P. Fried, Jacob L. Swett, Binoy Paulose Nadappuram, Jan A. Mol, Joshua B. Edel, Aleksandar P. Ivanov, and James R. Yates. In situ solid-state nanopore fabrication. *Chemical Society Reviews*, 50(8):4974–4992, 2021.

[14] Daniel Branton, David W Deamer, Andre Marziali, Hagan Bayley, Steven A Benner, Thomas Butler, Massimiliano Di Ventra, Slaven Garaj, Andrew Hibbs, Xiaohua Huang, Stevan B Jovanovich, Predrag S Krstic, Stuart Lindsay, Xinsheng Sean Ling, Carlos H Mastrangelo, Amit Meller, John S Oliver, Yuriy V Pershin, J Michael Ramsey, Robert Riehn, Gautam V Soni, Vincent Tabard-Cossa, Meni Wanunu, Matthew Wiggin, and Jeffery A Schloss. The potential and challenges of nanopore sequencing. *Nature Biotechnology*, 26(10):1146–1153, oct 2008.

[15] Liang Xue, Hirohito Yamazaki, Ren Ren, Meni Wanunu, Aleksandar P. Ivanov, and Joshua B. Edel. Solid-state nanopore sensors. *Nature Reviews Materials*, 5:932–951, sep 2020.

[16] Benjamin N. Miles, Aleksandar P. Ivanov, Kerry A. Wilson, Fatma Doğan, Deanpen Japrung, and Joshua B. Edel. Single molecule sensing with solid-state nanopores: novel materials, methods, and applications. *Chem. Soc. Rev.*, 42(1):15–28, 2013.

[17] J. J. Kasianowicz, E. Brandin, D. Branton, and D. W. Deamer. Characterization of individual polynucleotide molecules using a membrane channel. *Proceedings of the National Academy of Sciences*, 93(24):13770–13773, nov 1996.

[18] Tal Gilboa and Amit Meller. Optical sensing and analyte manipulation in solid-state nanopores. *The Analyst*, 140(14):4733–4747, 2015.

[19] Denis Garoli, Hirohito Yamazaki, Nicolò Maccaferri, and Meni Wanunu. Plasmonic nanopores for single-molecule detection and manipulation: Toward sequencing applications. *Nano Letters*, 19(11):7553–7562, oct 2019.

[20] Joshua D. Spitzberg, Adam Zrehen, Xander F. van Kooten, and Amit Meller. Plasmonic-nanopore biosensors for superior single-molecule detection. *Advanced Materials*, 31(23):1900422, apr 2019.

[21] Ping Xie, Qihua Xiong, Ying Fang, Quan Qing, and Charles M. Lieber. Local electrical potential detection of DNA by nanowire–nanopore sensors. *Nature Nanotechnology*, 7(2):119–125, dec 2011.

[22] Aleksandar P. Ivanov, Emanuele Instuli, Catriona M. McGilvery, Geoff Baldwin, David W. McComb, Tim Albrecht, and Joshua B. Edel. DNA tunneling detector embedded in a nanopore. *Nano Letters*, 11(1):279–285, jan 2011.

[23] Yanxiao Feng, Yuechuan Zhang, Cuifeng Ying, Deqiang Wang, and Chunlei Du. Nanopore-based fourth-generation DNA sequencing technology. *Genomics, Proteomics & Bioinformatics*, 13(1):4–16, feb 2015.

[24] Erik C. Yusko, Brandon R. Bruhn, Olivia M. Eggenberger, Jared Houghtaling, Ryan C. Rollings, Nathan C. Walsh, Santoshi Nandivada, Mariya Pindrus, Adam R. Hall, David Sept, Jiali Li, Devendra S. Kalonia, and Michael Mayer. Real-time shape approximation and fingerprinting of single proteins using a nanopore. *Nature Nanotechnology*, 12(4):360–367, dec 2016.

[25] Hadjer Ouldali, Kumar Sarthak, Tobias Ensslen, Fabien Piguet, Philippe Manivet, Juan Pelta, Jan C. Behrends, Aleksei Aksimentiev, and Abdelghani Oukhaled. Electrical recognition of the twenty proteinogenic amino acids using an aerolysin nanopore. *Nature Biotechnology*, 38(2):176–181, dec 2019.

[26] Nicholas A. W. Bell and Ulrich F. Keyser. Digitally encoded DNA nanostructures for multiplexed, single-molecule protein sensing with nanopores. *Nature Nanotechnology*, 11(7):645–651, apr 2016.

[27] Kaikai Chen, Jinbo Zhu, Filip Bošković, and Ulrich F. Keyser. Nanopore-based DNA hard drives for rewritable and secure data storage. *Nano Letters*, 20(5):3754–3760, apr 2020.

[28] Jasmine Y. Y. Sze, Aleksandar P. Ivanov, Anthony E. G. Cass, and Joshua B. Edel. Single molecule multiplexed nanopore protein screening in human serum using aptamer modified DNA carriers. *Nature Communications*, 8(1):1552, nov 2017.

[29] Yana Rozevsky, Tal Gilboa, Xander F. van Kooten, Dennis Kobelt, Diana Huttner, Ulrike Stein, and Amit Meller. Quantification of mRNA expression using single-molecule nanopore sensing. *ACS Nano*, 14(10):13964–13974, sep 2020.

[30] Kyloon Chuah, Yanfang Wu, S. R. C. Vivekchand, Katharina Gaus, Peter J. Reece, Adam P. Micolich, and J. Justin Gooding. Nanopore blockade sensors for ultrasensitive detection of proteins in complex biological samples. *Nature Communications*, 10(1):2109, may 2019.

[31] Kherim Willems, Veerle Van Meervelt, Carsten Wloka, and Giovanni Maglia. Single-molecule nanopore enzymology. *Philosophical Transactions of the Royal Society B: Biological Sciences*, 372(1726):20160230, jun 2017.

[32] Vignesh Sundaresan and Paul W. Bohn. Acid–base chemistry at the single ion limit. *Chemical Science*, 11(40):10951–10958, 2020.

[33] Kaiyu Fu and Paul W. Bohn. Nanopore electrochemistry: A nexus for molecular control of electron transfer reactions. *ACS Central Science*, 4(1):20–29, jan 2018.

[34] Yujia Qing, Mira D. Liu, Denis Hartmann, Linna Zhou, William J. Ramsay, and Hagan Bayley. Single-molecule observation of intermediates in bioorthogonal 2-cyanobenzothiazole chemistry. *Angewandte Chemie International Edition*, 59(36):15711–15716, aug 2020.

[35] Cees Dekker. Solid-state nanopores. *Nature Nanotechnology*, 2(4):209–215, mar 2007.

[36] Qi Chen and Zewen Liu. Fabrication and applications of solid-state nanopores. *Sensors*, 19(8):1886, apr 2019.

[37] Stefan Howorka. Building membrane nanopores. *Nature Nanotechnology*, 12(7):619–630, jul 2017.

[38] Min-Hyun Lee, Ashvani Kumar, Kyeong-Beom Park, Seong-Yong Cho, Hyun-Mi Kim, Min-Cheol Lim, Young-Rok Kim, and Ki-Bum Kim. A low-noise solid-state nanopore platform based on a highly insulating substrate. *Scientific Reports*, 4(1), dec 2014.

[39] Adrian Balan, Chen-Chi Chien, Rebecca Engelke, and Marija Drndić. Suspended solid-state membranes on glass chips with sub 1-pF capacitance for biomolecule sensing applications. *Scientific Reports*, 5(1), dec 2015.

[40] Mohamed Gad el Hak. *MEMS: Design and Fabrication*. CRC Press, 2005.

[41] J. Edel and T. Albrecht. *Engineered Nanopores For Bioanalytical Applications*. Elsevier, 2013.

[42] Bala Murali Venkatesan, Brian Dorvel, Sukru Yemenicioglu, Nicholas Watkins, Ivan Petrov, and Rashid Bashir. Highly sensitive, mechanically stable nanopore sensors for DNA analysis. *Advanced Materials*, 21(27):2771–2776, apr 2009.

[43] Bala Murali Venkatesan, Amish B. Shah, Jian-Min Zuo, and Rashid Bashir. DNA sensing using nanocrystalline surface-enhanced al2o3nanopore sensors. *Advanced Functional Materials*, 20(8):1266–1275, apr 2010.

[44] H. M. Wang, Z. Zheng, Y. Y. Wang, J. J. Qiu, Z. B. Guo, Z. X. Shen, and T. Yu. Fabrication of graphene nanogap with crystallographically matching edges and its electron emission properties. *Applied Physics Letters*, 96(2):023106, jan 2010.

[45] Joseph Larkin, Robert Henley, David C. Bell, Tzahi Cohen-Karni, Jacob K. Rosenstein, and Meni Wanunu. Slow DNA transport through nanopores in hafnium oxide membranes. *ACS Nano*, 7(11):10121–10128, oct 2013.

[46] Stephanie J. Heerema and Cees Dekker. Graphene nanodevices for DNA sequencing. *Nature Nanotechnology*, 11(2):127–136, feb 2016.

[47] Hadi Arjmandi-Tash, Liubov A. Belyaeva, and Grégory F. Schneider. Single molecule detection with graphene and other two-dimensional materials: nanopores and beyond. *Chemical Society Reviews*, 45(3):476–493, 2016.

[48] Jiandong Feng, Ke Liu, Roman D. Bulushev, Sergey Khlybov, Dumitru Dumcenco, Andras Kis, and Aleksandra Radenovic. Identification of single nucleotides in MoS2 nanopores. *Nature Nanotechnology*, 10(12):1070–1076, sep 2015.

[49] Song Liu, Bo Lu, Qing Zhao, Ji Li, Teng Gao, Yubin Chen, Yanfeng Zhang, Zhongfan Liu, Zhongchao Fan, Fuhua Yang, Liping You, and Dapeng Yu. Boron nitride nanopores: Highly sensitive DNA single-molecule detectors. *Advanced Materials*, 25(33):4549–4554, jun 2013.

[50] Gopinath Danda, Paul Masih Das, Yung-Chien Chou, Jerome T. Mlack, William M. Parkin, Carl H. Naylor, Kazunori Fujisawa, Tianyi Zhang, Laura Beth Fulton, Mauricio Terrones, Alan T. Charlie Johnson, and Marija Drndić. Monolayer WS2 nanopores for DNA translocation with light-adjustable sizes. *ACS Nano*, 11(2):1937–1945, feb 2017.

[51] Mehrnaz Mojtabavi, Armin VahidMohammadi, Wentao Liang, Majid Beidaghi, and Meni Wanunu. Single-molecule sensing using nanopores in two-dimensional transition metal carbide (MXene) membranes. *ACS Nano*, 13(3):3042–3053, mar 2019.

[52] Lorenz J. Steinbock, Oliver Otto, Catalin Chimerel, Joanne Gornall, and Ulrich F. Keyser. Detecting DNA folding with nanocapillaries. *Nano Letters*, 10(7):2493–2497, jul 2010.

[53] Erik C. Yusko, Jay M. Johnson, Sheereen Majd, Panchika Prangkio, Ryan C. Rollings, Jiali Li, Jerry Yang, and Michael Mayer. Controlling protein translocation through nanopores with bio-inspired fluid walls. *Nature Nanotechnology*, 6(4):253–260, feb 2011.

[54] Meni Wanunu, Jason Sutin, Ben McNally, Andrew Chow, and Amit Meller. DNA translocation governed by interactions with solid-state nanopores. *Biophysical Journal*, 95(10):4716–4725, nov 2008.

[55] Meni Wanunu, Tali Dadosh, Vishva Ray, Jingmin Jin, Larry McReynolds, and Marija Drndić. Rapid electronic detection of probe-specific microRNAs using thin nanopore sensors. *Nature Nanotechnology*, 5(11):807–814, oct 2010.

[56] Nitinun Varongchayakul, Jiaxi Song, Amit Meller, and Mark W. Grinstaff. Single-molecule protein sensing in a nanopore: a tutorial. *Chemical Society Reviews*, 47(23):8512–8524, 2018.

[57] Matthew Davenport, Ken Healy, Matthew Pevarnik, Nick Teslich, Stefano Cabrini, Alan P. Morrison, Zuzanna S. Siwy, and Sonia E. Létant. The role of pore geometry in single nanoparticle detection. *ACS Nano*, 6(9):8366–8380, aug 2012.

[58] Vincent Tabard-Cossa, Dhruti Trivedi, Matthew Wiggin, Nahid N Jetha, and Andre Marziali. Noise analysis and reduction in solid-state nanopores. *Nanotechnology*, 18(30):305505, jun 2007.

[59] Alessio Fragasso, Sonja Schmid, and Cees Dekker. Comparing current noise in biological and solid-state nanopores. *ACS Nano*, 14(2):1338–1349, feb 2020.

[60] William M. Parkin and Marija Drndić. Signal and noise in FET-nanopore devices. *ACS Sensors*, 3(2):313–319, jan 2018.

[61] Jacob K Rosenstein, Meni Wanunu, Christopher A Merchant, Marija Drndic, and Kenneth L Shepard. Integrated nanopore sensing platform with sub-microsecond temporal resolution. *Nature Methods*, 9(5):487–492, mar 2012.

[62] Siddharth Shekar, David J. Niedzwiecki, Chen-Chi Chien, Peijie Ong, Daniel A. Fleischer, Jianxun Lin, Jacob K. Rosenstein, Marija Drndić, and Kenneth L. Shepard. Measurement of DNA translocation dynamics in a solid-state nanopore at 100 ns temporal resolution. *Nano Letters*, 16(7):4483–4489, jun 2016.

[63] Chen-Chi Chien, Siddharth Shekar, David J. Niedzwiecki, Kenneth L. Shepard, and Marija Drndić. Single-stranded DNA translocation recordings through solid-state nanopores on glass chips at 10 MHz measurement bandwidth. *ACS Nano*, 13(9):10545–10554, aug 2019.

[64] Stephanie J. Heerema, Leonardo Vicarelli, Sergii Pud, Raymond N. Schouten, Henny W. Zandbergen, and Cees Dekker. Probing DNA translocations with inplane current signals in a graphene nanoribbon with a nanopore. *ACS Nano*, 12(3):2623–2633, feb 2018.

[65] Radin Tahvildari, Eric Beamish, Vincent Tabard-Cossa, and Michel Godin. Integrating nanopore sensors within microfluidic channel arrays using controlled breakdown. *Lab on a Chip*, 15(6):1407–1411, 2015.

[66] Abhishek Bhat, Paul V. Gwozdz, Arjun Seshadri, Marcel Hoeft, and Robert H. Blick. Tank circuit for ultrafast single-particle detection in micropores. *Physical Review Letters*, 121(7):078102, aug 2018.

[67] Kevin J. Freedman, Lauren M. Otto, Aleksandar P. Ivanov, Avijit Barik, Sang-Hyun Oh, and Joshua B. Edel. Nanopore sensing at ultra-low concentrations using single-molecule dielectrophoretic trapping. *Nature Communications*, 7(1), jan 2016.

[68] Jacob L Swett. *Low-Noise Suspended Silicon Nitride Devices and Their Applications*. PhD thesis, University of Oxford, 2020.

[69] F. Traversi, C. Raillon, S. M. Benameur, K. Liu, S. Khlybov, M. Tosun, D. Krasnozhon, A. Kis, and A. Radenovic. Detecting the translocation of DNA through a nanopore using graphene nanoribbons. *Nature Nanotechnology*, 8(12):939–945, nov 2013.

[70] Matthew Puster, Adrian Balan, Julio A. Rodríguez-Manzo, Gopinath Danda, Jae-Hyuk Ahn, William Parkin, and Marija Drndić. Cross-talk between ionic and nanoribbon current signals in graphene nanoribbon-nanopore sensors for single-molecule detection. *Small*, 11(47):6309–6316, oct 2015.

[71] Michael Graf, Martina Lihter, Damir Altus, Sanjin Marion, and Aleksandra Radenovic. Transverse detection of DNA using a MoS2 nanopore. *Nano Letters*, 19(12):9075–9083, nov 2019.

[72] Axel Fanget, Floriano Traversi, Sergey Khlybov, Pierre Granjon, Arnaud Magrez, László Forró, and Aleksandra Radenovic. Nanopore integrated nanogaps for DNA detection. *Nano Letters*, 14(1):244–249, dec 2013.

[73] Francesca Nicoli, Daniel Verschueren, Misha Klein, Cees Dekker, and Magnus P. Jonsson. DNA translocations through solid-state plasmonic nanopores. *Nano Letters*, 14(12):6917–6925, nov 2014.

[74] Dong Xiang, Xiaolong Wang, Chuancheng Jia, Takhee Lee, and Xuefeng Guo. Molecular-scale electronics: From concept to function. *Chemical Reviews*, 116(7):4318–4440, mar 2016.

[75] Ken Healy, Vishva Ray, Lauren J. Willis, Neil Peterman, John Bartel, and Marija Drndić. Fabrication and characterization of nanopores with insulated transverse nanoelectrodes for DNA sensing in salt solution. *Elecrophoresis*, 33(23):3488–3496, dec 2012.

[76] Patrick S Spinney, Scott D Collins, David G Howitt, and Rosemary L Smith. Fabrication and characterization of a solid-state nanopore with self-aligned carbon nanoelectrodes for molecular detection. *Nanotechnology*, 23(13):135501, mar 2012.

[77] Pei Pang, Brian Alan Ashcroft, Weisi Song, Peiming Zhang, Sovan Biswas, Quan Qing, Jialing Yang, Robert J. Nemanich, Jingwei Bai, Joshua T. Smith, Kathleen Reuter, Venkat S. K. Balagurusamy, Yann Astier, Gustavo Stolovitzky, and Stuart Lindsay. Fixed-gap tunnel junction for reading DNA nucleotides. *ACS Nano*, 8(12):11994–12003, nov 2014.

[78] Makusu Tsutsui, Sakon Rahong, Yoko Iizumi, Toshiya Okazaki, Masateru Taniguchi, and Tomoji Kawai. Single-molecule sensing electrode embedded in-plane nanopore. *Scientific Reports*, 1(1), jul 2011.

[79] Makusu Tsutsui, Masateru Taniguchi, Kazumichi Yokota, and Tomoji Kawai. Identifying single nucleotides by tunnelling current. *Nature Nanotechnology*, 5(4):286–290, mar 2010.

[80] Shuai Chang, Jin He, Ashley Kibel, Myeong Lee, Otto Sankey, Peiming Zhang, and Stuart Lindsay. Tunnelling readout of hydrogen-bonding-based recognition. *Nature Nanotechnology*, 4(5):297–301, mar 2009.

[81] T. Ohshiro and Y. Umezawa. Complementary base-pair-facilitated electron tunneling for electrically pinpointing complementary nucleobases. *Proceedings of the National Academy of Sciences*, 103(1):10–14, dec 2005.

[82] Longhua Tang, Binoy Paulose Nadappuram, Paolo Cadinu, Zhiyu Zhao, Liang Xue, Long Yi, Ren Ren, Jiangwei Wang, Aleksandar P. Ivanov, and Joshua B. Edel. Combined quantum tunnelling and dielectrophoretic trapping for molecular analysis at ultra-low analyte concentrations. *Nature Communications*, 12(1), feb 2021.

[83] Yanan Zhao, Brian Ashcroft, Peiming Zhang, Hao Liu, Suman Sen, Weisi Song, JongOne Im, Brett Gyarfas, Saikat Manna, Sovan Biswas, Chad Borges, and Stuart

Lindsay. Single-molecule spectroscopy of amino acids and peptides by recognition tunnelling. *Nature Nanotechnology*, 9(6):466–473, apr 2014.

[84] JongOne Im, Sovan Biswas, Hao Liu, Yanan Zhao, Suman Sen, Sudipta Biswas, Brian Ashcroft, Chad Borges, Xu Wang, Stuart Lindsay, and Peiming Zhang. Electronic single-molecule identification of carbohydrate isomers by recognition tunnelling. *Nature Communications*, 7(1):13868, dec 2016.

[85] Makusu Tsutsui, Kazuki Matsubara, Takahito Ohshiro, Masayuki Furuhashi, Masateru Taniguchi, and Tomoji Kawai. Electrical detection of single methylcytosines in a DNA oligomer. *Journal of the American Chemical Society*, 133(23):9124–9128, jun 2011.

[86] Bintian Zhang, Weisi Song, Pei Pang, Yanan Zhao, Peiming Zhang, István Csabai, Gábor Vattay, and Stuart Lindsay. Observation of giant conductance fluctuations in a protein. *Nano Futures*, 1(3):035002, nov 2017.

[87] Bintian Zhang, Weisi Song, Pei Pang, Huafang Lai, Qiang Chen, Peiming Zhang, and Stuart Lindsay. Role of contacts in long-range protein conductance. *Proceedings of the National Academy of Sciences*, 116(13):5886–5891, mar 2019.

[88] Stuart Lindsay. Ubiquitous electron transport in non-electron transfer proteins. *Life*, 10(5):72, may 2020.

[89] Gautam V. Soni, Alon Singer, Zhiliang Yu, Yingjie Sun, Ben McNally, and Amit Meller. Synchronous optical and electrical detection of biomolecules traversing through solid-state nanopores. *Review of Scientific Instruments*, 81(1):014301, jan 2010.

[90] Ben McNally, Alon Singer, Zhiliang Yu, Yingjie Sun, Zhiping Weng, and Amit Meller. Optical recognition of converted DNA nucleotides for single-molecule DNA sequencing using nanopore arrays. *Nano Letters*, 10(6):2237–2244, jun 2010.

[91] Ruby dela Torre, Joseph Larkin, Alon Singer, and Amit Meller. Fabrication and characterization of solid-state nanopore arrays for high-throughput DNA sequencing. *Nanotechnology*, 23(38):385308, sep 2012.

[92] Rui Wang, Tal Gilboa, Jiaxi Song, Diana Huttner, Mark W. Grinstaff, and Amit Meller. Single-molecule discrimination of labeled DNAs and polypeptides using photoluminescent-free TiO2 nanopores. *ACS Nano*, 12(11):11648–11656, oct 2018.

[93] Furat Sawafta, Bason Clancy, Autumn T. Carlsen, Martin Huber, and Adam R. Hall. Solid-state nanopores and nanopore arrays optimized for optical detection. *Nanoscale*, 6(12):6991–6996, 2014.

[94] Ossama N. Assad, Nicolas Di Fiori, Allison H. Squires, and Amit Meller. Two color DNA barcode detection in photoluminescence suppressed silicon nitride nanopores. *Nano Letters*, 15(1):745–752, dec 2014.

[95] Brett N. Anderson, Ossama N. Assad, Tal Gilboa, Allison H. Squires, Daniel Bar, and Amit Meller. Probing solid-state nanopores with light for the detection of unlabeled analytes. *ACS Nano*, 8(11):11836–11845, nov 2014.

[96] Andrey Ivankin, Robert Y. Henley, Joseph Larkin, Spencer Carson, Michael L. Toscano, and Meni Wanunu. Label-free optical detection of biomolecular translocation through nanopore arrays. *ACS Nano*, 8(10):10774–10781, sep 2014.

[97] Andrew J. Heron, James R. Thompson, Bríd Cronin, Hagan Bayley, and Mark I. Wallace. Simultaneous measurement of ionic current and fluorescence from single protein pores. *Journal of the American Chemical Society*, 131(5):1652–1653, feb 2009.

[98] Ossama N. Assad, Tal Gilboa, Joshua Spitzberg, Matyas Juhasz, Elmar Weinhold, and Amit Meller. Light-enhancing plasmonic-nanopore biosensor for superior single-molecule detection. *Advanced Materials*, 29(9):1605442, dec 2016.

[99] Colin R. Crick, Pablo Albella, Hyung-Jun Kim, Aleksandar P. Ivanov, Ki-Bum Kim, Stefan A. Maier, and Joshua B. Edel. Low-noise plasmonic nanopore biosensors for single molecule detection at elevated temperatures. *ACS Photonics*, 4(11):2835–2842, oct 2017.

[100] SungWoo Nam, Inhee Choi, Chi cheng Fu, Kwanpyo Kim, SoonGweon Hong, Yeonho Choi, Alex Zettl, and Luke P. Lee. Graphene nanopore with a self-integrated optical antenna. *Nano Letters*, 14(10):5584–5589, sep 2014.

[101] Xin Shi, Rui Gao, Yi-Lun Ying, Wei Si, Yun-Fei Chen, and Yi-Tao Long. A scattering nanopore for single nanoentity sensing. *ACS Sensors*, 1(9):1086–1090, aug 2016.

[102] Daniel V. Verschueren, Sergii Pud, Xin Shi, Lorenzo De Angelis, L. Kuipers, and Cees Dekker. Label-free optical detection of DNA translocations through plasmonic nanopores. *ACS Nano*, 13(1):61–70, dec 2018.

[103] Daniel Verschueren, Xin Shi, and Cees Dekker. Nano-optical tweezing of single proteins in plasmonic nanopores. *Small Methods*, 3(5):1800465, jan 2019.

[104] Maxim Belkin, Shu-Han Chao, Magnus P. Jonsson, Cees Dekker, and Aleksei Aksimentiev. Plasmonic nanopores for trapping, controlling displacement, and sequencing of DNA. *ACS Nano*, 9(11):10598–10611, oct 2015.

[105] Jiali Li, Derek Stein, Ciaran McMullan, Daniel Branton, Michael J. Aziz, and Jene A. Golovchenko. Ion-beam sculpting at nanometre length scales. *Nature*, 412(6843):166–169, jul 2001.

[106] A. J. Storm, J. H. Chen, X. S. Ling, H. W. Zandbergen, and C. Dekker. Fabrication of solid-state nanopores with single-nanometre precision. *Nature Materials*, 2(8):537–540, jul 2003.

[107] M. J. Kim, M. Wanunu, D. C. Bell, and A. Meller. Rapid fabrication of uniformly sized nanopores and nanopore arrays for parallel DNA analysis. *Advanced Materials*, 18(23):3149–3153, dec 2006.

[108] Meng-Yue Wu, Ralph M. M. Smeets, Mathijs Zandbergen, Ulrike Ziese, Diego Krapf, Philip E. Batson, Nynke H. Dekker, Cees Dekker, and Henny W. Zandbergen. Control of shape and material composition of solid-state nanopores. *Nano Letters*, 9(1):479–484, jan 2009.

[109] Michiel van den Hout, Adam R Hall, Meng Yue Wu, Henny W Zandbergen, Cees Dekker, and Nynke H Dekker. Controlling nanopore size, shape and stability. *Nanotechnology*, 21(11):115304, feb 2010.

[110] J. Gierak, A. Madouri, A.L. Biance, E. Bourhis, G. Patriarche, C. Ulysse, D. Lucot, X. Lafosse, L. Auvray, L. Bruchhaus, and R. Jede. Sub-5nm FIB direct patterning of nanodevices. *Microelectronic Engineering*, 84(5-8):779–783, may 2007.

[111] Chih Jen Lo, Thomas Aref, and Alexey Bezryadin. Fabrication of symmetric sub-5 nm nanopores using focused ion and electron beams. *Nanotechnology*, 17(13):3264–3267, jun 2006.

[112] Furat Sawafta, Autumn Carlsen, and Adam Hall. Membrane thickness dependence of nanopore formation with a focused helium ion beam. *Sensors*, 14(5):8150–8161, may 2014.

[113] D. Emmrich, A. Beyer, A. Nadzeyka, S. Bauerdick, J. C. Meyer, J. Kotakoski, and A. Gölzhäuser. Nanopore fabrication and characterization by helium ion microscopy. *Applied Physics Letters*, 108(16):163103, apr 2016.

[114] Deying Xia, Chuong Huynh, Shawn McVey, Aaron Kobler, Lewis Stern, Zhishan Yuan, and Xinsheng Sean Ling. Rapid fabrication of solid-state nanopores with high reproducibility over a large area using a helium ion microscope. *Nanoscale*, 10(11):5198–5204, 2018.

[115] Jingwei Bai, Deqiang Wang, Sung wook Nam, Hongbo Peng, Robert Bruce, Lynn Gignac, Markus Brink, Ernst Kratschmer, Stephen Rossnagel, Phil Waggoner, Kathleen Reuter, Chao Wang, Yann Astier, Venkat Balagurusamy, Binquan Luan, Young Kwark, Eric Joseph, Mike Guillorn, Stanislav Polonsky, Ajay Royyuru, S. Papa Rao, and Gustavo Stolovitzky. Fabrication of sub-20 nm nanopore arrays in membranes with embedded metal electrodes at wafer scales. *Nanoscale*, 6(15):8900–8906, 2014.

[116] Matthew Puster, Julio A. Rodríguez-Manzo, Adrian Balan, and Marija Drndić. Toward sensitive graphene nanoribbon–nanopore devices by preventing electron beam-induced damage. *ACS Nano*, 7(12):11283–11289, nov 2013.

[117] Yung-Chien Chou, Paul Masih Das, Dimitri S. Monos, and Marija Drndić. Lifetime and stability of silicon nitride nanopores and nanopore arrays for ionic measurements. *ACS Nano*, 14(6):6715–6728, apr 2020.

[118] Anpan Han, Gregor Schürmann, Giampietro Mondin, Roland Andreas Bitterli, Nicole G. Hegelbach, Nico F. de Rooij, and Urs Staufer. Sensing protein molecules using nanofabricated pores. *Applied Physics Letters*, 88(9):093901, feb 2006.

[119] Anpan Han, Marc Creus, Gregor Schurmann, Vincent Linder, Thomas R. Ward, Nico F. de Rooij, and Urs Staufer. Label-free detection of single protein molecules and protein-protein interactions using synthetic nanopores. *Analytical Chemistry*, 80(12):4651–4658, jun 2008.

[120] Daniel V Verschueren, Wayne Yang, and Cees Dekker. Lithography-based fabrication of nanopore arrays in freestanding SiN and graphene membranes. *Nanotechnology*, 29(14):145302, feb 2018.

[121] Sung-Wook Nam, Michael J. Rooks, Ki-Bum Kim, and Stephen M. Rossnagel. Ionic field effect transistors with sub-10 nm multiple nanopores. *Nano Letters*, 9(5):2044–2048, may 2009.

[122] Shuangshuang Zeng, Chenyu Wen, Paul Solomon, Shi-Li Zhang, and Zhen Zhang. Rectification of protein translocation in truncated pyramidal nanopores. *Nature Nanotechnology*, 14(11):1056–1062, oct 2019.

[123] Miloslav Karhanek, Jennifer T. Kemp, Nader Pourmand, Ronald W. Davis, and Chris D. Webb. Single DNA molecule detection using nanopipettes and nanoparticles. *Nano Letters*, 5(2):403–407, feb 2005.

[124] Celeste A. Morris, Alicia K. Friedman, and Lane A. Baker. Applications of nanopipettes in the analytical sciences. *The Analyst*, 135(9):2190, 2010.

[125] Zhe Wang, Yichong Liu, Lei Yu, Yunchuan Li, Gongming Qian, and Shuai Chang. Nanopipettes: a potential tool for DNA detection. *The Analyst*, 144(17):5037–5047, 2019.

[126] Liming Ying. Applications of nanopipettes in bionanotechnology. *Biochemical Society Transactions*, 37(4):702–706, jul 2009.

[127] David Perry, Dmitry Momotenko, Robert A. Lazenby, Minkyung Kang, and Patrick R. Unwin. Characterization of nanopipettes. *Analytical Chemistry*, 88(10):5523–5530, may 2016.

[128] Martin Holub, Maria Adobes-Vidal, Andreas Frutiger, Pascal M. Gschwend, Sotiris E. Pratsinis, and Dmitry Momotenko. Single-nanoparticle thermometry with a nanopipette. *ACS Nano*, 14(6):7358–7369, may 2020.

[129] Paolo Cadinu, Binoy Paulose Nadappuram, Dominic J. Lee, Jasmine Y. Y. Sze, Giulia Campolo, Yanjun Zhang, Andrew Shevchuk, Sylvain Ladame, Tim Albrecht, Yuri Korchev, Aleksandar P. Ivanov, and Joshua B. Edel. Single molecule trapping and sensing using dual nanopores separated by a zeptoliter nanobridge. *Nano Letters*, 17(10):6376–6384, sep 2017.

[130] Paolo Cadinu, Minkyung Kang, Binoy Paulose Nadappuram, Aleksandar P. Ivanov, and Joshua B. Edel. Individually addressable multi-nanopores for single-molecule targeted operations. *Nano Letters*, 20(3):2012–2019, feb 2020.

[131] Ren Ren, Yanjun Zhang, Binoy Paulose Nadappuram, Bernice Akpinar, David Klenerman, Aleksandar P. Ivanov, Joshua B. Edel, and Yuri Korchev. Nanopore extended field-effect transistor for selective single-molecule biosensing. *Nature Communications*, 8(1):586, sep 2017.

[132] Anna E. P. Schibel and Eric N. Ervin. Antigen detection via the rate of ion current rectification change of the antibody-modified glass nanopore membrane. *Langmuir*, 30(37):11248–11256, sep 2014.

[133] Shu Ding, Changlu Gao, and Li-Qun Gu. Capturing single molecules of immunoglobulin and ricin with an aptamer-encoded glass nanopore. *Analytical Chemistry*, 81(16):6649–6655, aug 2009.

[134] Niya Sa, Yaqin Fu, and Lane A. Baker. Reversible cobalt ion binding to imidazole-modified nanopipettes. *Analytical Chemistry*, 82(24):9963–9966, dec 2010.

[135] Yaqin Fu, Hideo Tokuhisa, and Lane A. Baker. Nanopore DNA sensors based on dendrimer-modified nanopipettes. *Chemical Communications*, (32):4877, 2009.

[136] Tal Gilboa, Adam Zrehen, Arik Girsault, and Amit Meller. Optically-monitored nanopore fabrication using a focused laser beam. *Scientific Reports*, 8(1):9765, jun 2018.

[137] Tal Gilboa, Eran Zvuloni, Adam Zrehen, Allison H. Squires, and Amit Meller. Automated, ultra-fast laser-drilling of nanometer scale pores and nanopore arrays in aqueous solutions. *Advanced Functional Materials*, 30(18):1900642, apr 2019.

[138] Hirohito Yamazaki, Rui Hu, Qing Zhao, and Meni Wanunu. Photothermally assisted thinning of silicon nitride membranes for ultrathin asymmetric nanopores. *ACS Nano*, 12(12):12472–12481, nov 2018.

[139] Matthew Waugh, Kyle Briggs, Dylan Gunn, Mathieu Gibeault, Simon King, Quinn Ingram, Aura Melissa Jimenez, Samuel Berryman, Dmytro Lomovtsev, Lukasz Andrzejewski, and Vincent Tabard-Cossa. Solid-state nanopore fabrication by automated controlled breakdown. *Nature Protocols*, 15(1):122–143, dec 2020.

[140] Harold Kwok, Kyle Briggs, and Vincent Tabard-Cossa. Nanopore fabrication by controlled dielectric breakdown. *PLoS ONE*, 9(3):e92880, mar 2014.

[141] Yusuke Goto, Itaru Yanagi, Kazuma Matsui, Takahide Yokoi, and Ken ichi Takeda. Identification of four single-stranded DNA homopolymers with a solid-state nanopore in alkaline CsCl solution. *Nanoscale*, 10(44):20844–20850, 2018.

[142] Kyle Briggs, Gregory Madejski, Martin Magill, Konstantinos Kastritis, Hendrick W. de Haan, James L. McGrath, and Vincent Tabard-Cossa. DNA translocations through nanopores under nanoscale preconfinement. *Nano Letters*, 18(2):660–668, dec 2017.

[143] Y.M. Nuwan D.Y. Bandara, Jugal Saharia, Buddini I. Karawdeniya, James T Hagan, Jason Dwyer, and MinJun Kim. Beyond nanopore sizing: improving solid-state single-molecule sensing performance, lifetime, and analyte scope for omics by targeting surface chemistry during fabrication. *Nanotechnology*, 31:335707, may 2020.

[144] Joshua D. Spitzberg, Xander F. van Kooten, Moran Bercovici, and Amit Meller. Microfluidic device for coupling isotachophoretic sample focusing with nanopore single-molecule sensing. *Nanoscale*, 12(34):17805–17811, 2020.

[145] Itaru Yanagi, Rena Akahori, Toshiyuki Hatano, and Ken ichi Takeda. Fabricating nanopores with diameters of sub-1 nm to 3 nm using multilevel pulse-voltage injection. *Scientific Reports*, 4(1):5000, may 2014.

[146] Christopher E. Arcadia, Carlos C. Reyes, and Jacob K. Rosenstein. In situ nanopore fabrication and single-molecule sensing with microscale liquid contacts. *ACS Nano*, 11(5):4907–4915, may 2017.

[147] Kyle Briggs, Martin Charron, Harold Kwok, Timothea Le, Sanmeet Chahal, José Bustamante, Matthew Waugh, and Vincent Tabard-Cossa. Kinetics of nanopore fabrication during controlled breakdown of dielectric membranes in solution. *Nanotechnology*, 26(8):084004, feb 2015.

[148] S. Habermehl, R. T. Apodaca, and R. J. Kaplar. On dielectric breakdown in silicon-rich silicon nitride thin films. *Applied Physics Letters*, 94(1):012905, jan 2009.

[149] S. M. Sze. Current transport and maximum dielectric strength of silicon nitride films. *Journal of Applied Physics*, 38(7):2951–2956, jun 1967.

[150] S. Habermehl and C. Carmignani. Correlation of charge transport to local atomic strain in si-rich silicon nitride thin films. *Applied Physics Letters*, 80(2):261–263, jan 2002.

[151] Eric Beamish, Harold Kwok, Vincent Tabard-Cossa, and Michel Godin. Precise control of the size and noise of solid-state nanopores using high electric fields. *Nanotechnology*, 23(40):405301, sep 2012.

[152] Chelsea Leung, Kyle Briggs, Marie-Pier Laberge, Smile Peng, Matthew Waugh, and Vincent Tabard-Cossa. Mechanisms of solid-state nanopore enlargement under electrical stress. *Nanotechnology*, 31(44):44LT01, aug 2020.

[153] Michelle H. Lam, Kyle Briggs, Konstantinos Kastritis, Martin Magill, Gregory R. Madejski, James L. McGrath, Hendrick W. de Haan, and Vincent Tabard-Cossa. Entropic trapping of DNA with a nanofiltered nanopore. *ACS Applied Nano Materials*, 2(8):4773–4781, jun 2019.

[154] Gregory R. Madejski, Kyle Briggs, Jon-Paul DesOrmeaux, Joshua J. Miller, James A. Roussie, Vincent Tabard-Cossa, and James L. McGrath. Monolithic fabrication of NPN/SiN x dual membrane cavity for nanopore-based DNA sensing. *Advanced Materials Interfaces*, 6(14):1900684, may 2019.

[155] Radin Tahvildari, Eric Beamish, Kyle Briggs, Sophie Chagnon-Lessard, Ali Najafi Sohi, Shuo Han, Benjamin Watts, Vincent Tabard-Cossa, and Michel Godin. Manipulating electrical and fluidic access in integrated nanopore-microfluidic arrays using microvalves. *Small*, 13(10):1602601, dec 2016.

[156] Ali Najafi Sohi, Eric Beamish, Vincent Tabard-Cossa, and Michel Godin. DNA capture by nanopore sensors under flow. *Analytical Chemistry*, 92(12):8108–8116, may 2020.

[157] Kyle Briggs, Harold Kwok, and Vincent Tabard-Cossa. Automated fabrication of 2-nm solid-state nanopores for nucleic acid analysis. *Small*, 10(10):2077–2086, mar 2014.

[158] Itaru Yanagi, Koji Fujisaki, Hirotaka Hamamura, and Ken ichi Takeda. Thickness-dependent dielectric breakdown and nanopore creation on sub-10-nm-thick SiN membranes in solution. *Journal of Applied Physics*, 121(4):045301, jan 2017.

[159] Itaru Yanagi, Takeshi Ishida, Koji Fujisaki, and Ken ichi Takeda. Fabrication of 3-nm-thick si3n4 membranes for solid-state nanopores using the poly-si sacrificial layer process. *Scientific Reports*, 5(1):14656, oct 2015.

[160] Cuifeng Ying, Yuechuan Zhang, Yanxiao Feng, Daming Zhou, Deqiang Wang, Yinxiao Xiang, Wenyuan Zhou, Yongsheng Chen, Chunlei Du, and Jianguo Tian. 3d nanopore shape control by current-stimulus dielectric breakdown. *Applied Physics Letters*, 109(6):063105, aug 2016.

[161] Yifan Wang, Qi Chen, Tao Deng, and Zewen Liu. Nanopore fabricated in pyramidal HfO2 film by dielectric breakdown method. *Applied Physics Letters*, 111(14):143103, oct 2017.

[162] Harold Kwok, Matthew Waugh, José Bustamante, Kyle Briggs, and Vincent Tabard-Cossa. Long passage times of short ssDNA molecules through metallized nanopores fabricated by controlled breakdown. *Advanced Functional Materials*, 24(48):7745–7753, oct 2014.

[163] Meni Wanunu and Amit Meller. Chemically modified solid-state nanopores. *Nano Letters*, 7(6):1580–1585, jun 2007.

[164] Ren Ren, Xiaoyi Wang, Shenglin Cai, Yanjun Zhang, Yuri Korchev, Aleksandar P. Ivanov, and Joshua B. Edel. Selective sensing of proteins using aptamer functionalized nanopore extended field-effect transistors. *Small Methods*, page 2000356, jul 2020.

[165] Olivia M. Eggenberger, Cuifeng Ying, and Michael Mayer. Surface coatings for solid-state nanopores. *Nanoscale*, 11(42):19636–19657, 2019.

[166] Y. M. Nuwan D. Y. Bandara, Buddini I. Karawdeniya, James T. Hagan, Robert B. Chevalier, and Jason R. Dwyer. Chemically functionalizing controlled dielectric breakdown silicon nitride nanopores by direct photohydrosilylation. *ACS Applied Materials & Interfaces*, 11(33):30411–30420, jul 2019.

[167] Ahmed Arafat, Karin Schroën, Louis C. P. M. de Smet, Ernst J. R. Sudhölter, and Han Zuilhof. Tailor-made functionalization of silicon nitride surfaces. *Journal of the American Chemical Society*, 126(28):8600–8601, jul 2004.

[168] Ahmed Arafat, Marcel Giesbers, Michel Rosso, Ernst J. R. Sudhölter, Karin Schroën, Richard G. White, Li Yang, Matthew R. Linford, and Han Zuilhof. Covalent biofunctionalization of silicon nitride surfaces. *Langmuir*, 23(11):6233–6244, may 2007.

[169] Cuifeng Ying, Jared Houghtaling, Olivia M. Eggenberger, Anirvan Guha, Peter Nirmalraj, Saurabh Awasthi, Jianguo Tian, and Michael Mayer. Formation of single nanopores with diameters of 20–50 nm in silicon nitride membranes using laser-assisted controlled breakdown. *ACS Nano*, 12(11):11458–11470, oct 2018.

[170] Yunlong Wang, Cuifeng Ying, Wenyuan Zhou, Lennart de Vreede, Zhibo Liu, and Jianguo Tian. Fabrication of multiple nanopores in a SiNx membrane via controlled breakdown. *Scientific Reports*, 8(1):1234, jan 2018.

[171] Adam Zrehen, Tal Gilboa, and Amit Meller. Real-time visualization and sub-diffraction limit localization of nanometer-scale pore formation by dielectric breakdown. *Nanoscale*, 9(42):16437–16445, 2017.

[172] Itaru Yanagi, Hirotaka Hamamura, Rena Akahori, and Ken ichi Takeda. Two-step breakdown of a SiN membrane for nanopore fabrication: Formation of thin portion and penetration. *Scientific Reports*, 8(1):10129, jul 2018.

[173] Itaru Yanagi, Rena Akahori, and Ken ichi Takeda. Stable fabrication of a large nanopore by controlled dielectric breakdown in a high-pH solution for the detection of various-sized molecules. *Scientific Reports*, 9(1):13143, sep 2019.

[174] Aaron T. Kuan, Bo Lu, Ping Xie, Tamas Szalay, and Jene A. Golovchenko. Electrical pulse fabrication of graphene nanopores in electrolyte solution. *Applied Physics Letters*, 106(20):203109, may 2015.

[175] Ming Dong, Zifan Tang, Xiaodong He, and Weihua Guan. Direct observation of redox-induced bubble generation and nanopore formation dynamics in controlled dielectric breakdown. *ACS Applied Electronic Materials*, 2(9):2954–2960, aug 2020.

[176] Hirohito Yamazaki, Rui Hu, Robert Y. Henley, Justin Halman, Kirill A. Afonin, Dapeng Yu, Qing Zhao, and Meni Wanunu. Label-free single-molecule thermoscopy using a laser-heated nanopore. *Nano Letters*, 17(11):7067–7074, oct 2017.

[177] Paolo Cadinu, Giulia Campolo, Sergii Pud, Wayne Yang, Joshua B. Edel, Cees Dekker, and Aleksandar P. Ivanov. Double barrel nanopores as a new tool for controlling single-molecule transport. *Nano Letters*, 18(4):2738–2745, mar 2018.

[178] Xu Liu, Philip Zimny, Yuning Zhang, Ankit Rana, Roland Nagel, Walter Reisner, and William B. Dunbar. Flossing DNA in a dual nanopore device. *Small*, 16(3):1905379, dec 2019.

[179] Yuning Zhang, Xu Liu, Yanan Zhao, Jen-Kan Yu, Walter Reisner, and William B. Dunbar. Single molecule DNA resensing using a two-pore device. *Small*, 14(47):1801890, oct 2018.

[180] Autumn T Carlsen, Kyle Briggs, Adam R Hall, and Vincent Tabard-Cossa. Solid-state nanopore localization by controlled breakdown of selectively thinned membranes. *Nanotechnology*, 28(8):085304, jan 2017.

[181] Bohua Yin, Shaoxi Fang, Daming Zhou, Liyuan Liang, Liang Wang, Zuobin Wang, Deqiang Wang, and Jiahu Yuan. Nanopore fabrication via transient high electric field controlled breakdown and detection of single RNA molecules. *ACS Applied Bio Materials*, 3(9):6368–6375, aug 2020.

[182] Yuning Zhang, Yoichi Miyahara, Nassim Derriche, Wayne Yang, Khadija Yazda, Xavier Capaldi, Zezhou Liu, Peter Grutter, and Walter Reisner. Nanopore formation via tip-controlled local breakdown using an atomic force microscope. *Small Methods*, page 1900147, apr 2019.

[183] Julio A. Rodríguez-Manzo, Matthew Puster, Adrien Nicolaï, Vincent Meunier, and Marija Drndić. DNA translocation in nanometer thick silicon nanopores. *ACS Nano*, 9(6):6555–6564, jun 2015.

[184] S. Garaj, W. Hubbard, A. Reina, J. Kong, D. Branton, and J. A. Golovchenko. Graphene as a subnanometre trans-electrode membrane. *Nature*, 467(7312):190–193, aug 2010.

[185] S. Garaj, S. Liu, J. A. Golovchenko, and D. Branton. Molecule-hugging graphene nanopores. *Proceedings of the National Academy of Sciences*, 110(30):12192–12196, jul 2013.

[186] S. Habermehl and R. T. Apodaca. Dielectric breakdown and poole–frenkel field saturation in silicon oxynitride thin films. *Applied Physics Letters*, 86(7):072103, 2005.

[187] J. Bustamante. Synchronous optical and electrical measurements of single dna molecules translocating through a solid-state nanopore. Master's thesis, University of Ottowa, 2014.

[188] Sergii Pud, Daniel Verschueren, Nikola Vukovic, Calin Plesa, Magnus P. Jonsson, and Cees Dekker. Self-aligned plasmonic nanopores by optically controlled dielectric breakdown. *Nano Letters*, 15(10):7112–7117, sep 2015.

[189] J. Feng, K. Liu, M. Graf, M. Lihter, R. D. Bulushev, D. Dumcenco, D. T. L. Alexander, D. Krasnozhon, T. Vuletic, A. Kis, and A. Radenovic. Electrochemical reaction in single layer MoS2: Nanopores opened atom by atom. *Nano Letters*, 15(5):3431–3438, may 2015.

[190] Michael Graf, Martina Lihter, Mukeshchand Thakur, Vasileia Georgiou, Juraj Topolancik, B. Robert Ilic, Ke Liu, Jiandong Feng, Yann Astier, and Aleksandra Radenovic. Fabrication and practical applications of molybdenum disulfide nanopores. *Nature Protocols*, 14(4):1130–1168, mar 2019.

[191] Xiaoyan Zhang, Pauline M.G. van Deursen, Wangyang Fu, and Grégory F. Schneider. Facile and ultraclean graphene-on-glass nanopores by controlled electrochemical etching. *ACS Sensors*, 5(8):2317–2325, jun 2020.

[192] Stefan W Kowalczyk, Alexander Y Grosberg, Yitzhak Rabin, and Cees Dekker. Modeling the conductance and DNA blockade of solid-state nanopores. *Nanotechnology*, 22(31):315101, jul 2011.

[193] Peng Chen, Jiajun Gu, Eric Brandin, Young-Rok Kim, Qiao Wang, and Daniel Branton. Probing single DNA molecule transport using fabricated nanopores. *Nano Letters*, 4(11):2293–2298, nov 2004.

[194] Alexander Y. Grosberg and Yitzhak Rabin. DNA capture into a nanopore: Interplay of diffusion and electrohydrodynamics. *The Journal of Chemical Physics*, 133(16):165102, oct 2010.

[195] Peng Chen, Toshiyuki Mitsui, Damon B. Farmer, Jene Golovchenko, Roy G. Gordon, and Daniel Branton. Atomic layer deposition to fine-tune the surface properties and diameters of fabricated nanopores. *Nano Letters*, 4(7):1333–1337, jul 2004.

[196] Jasper P. Fried, Jacob L. Swett, Binoy Paulose Nadappuram, Aleksandra Fedosyuk, Pedro Miguel Sousa, Dayrl P. Briggs, Aleksandar P. Ivanov, Joshua B. Edel, Jan A. Mol, and James R. Yates. Understanding electrical conduction and nanopore formation during controlled breakdown. *arXiv*, page 2103.16667, 2021.

[197] Itaru Yanagi and Ken ichi Takeda. Current–voltage characteristics of SiN membranes in solution. *ACS Applied Electronic Materials*, 2(9):2760–2771, jul 2020.

[198] Doo Seok Jeong, Hong Bae Park, and Cheol Seong Hwang. Reasons for obtaining an optical dielectric constant from the poole–frenkel conduction behavior of atomic-layer-deposited HfO[sub 2] films. *Applied Physics Letters*, 86(7):072903, 2005.

[199] J. J. O Dwyer. Current-voltage characteristics of dielectric films. *Journal of Applied Physics*, 37(2):599–601, feb 1966.

[200] Herbert Schroeder. Poole-frenkel-effect as dominating current mechanism in thin oxide films—an illusion?! *Journal of Applied Physics*, 117(21):215103, jun 2015.

[201] J. M. Andrews, B. G. Jackson, and W. J. Polito. High-field dark currents in thin CVD silicon nitride. *Journal of Applied Physics*, 51(1):495–502, jan 1980.

[202] C. M. Svensson. The conduction mechanism in silicon nitride films. *Journal of Applied Physics*, 48(1):329–335, jan 1977.

[203] D. L. Pulfrey, A. H. M. Shousha, and L. Young. Electronic conduction and space charge in amorphous insulating films. *Journal of Applied Physics*, 41(7):2838–2843, jun 1970.

[204] S. Habermehl. Stress relaxation in si-rich silicon nitride thin films. *Journal of Applied Physics*, 83(9):4672–4677, may 1998.

[205] Rohit Karnik, Chuanhua Duan, Kenneth Castelino, Hirofumi Daiguji, and Arun Majumdar. Rectification of ionic current in a nanofluidic diode. *Nano Letters*, 7(3):547–551, mar 2007.

[206] Chang Wei, Allen J. Bard, and Stephen W. Feldberg. Current rectification at quartz nanopipet electrodes. *Analytical Chemistry*, 69(22):4627–4633, nov 1997.

[207] Henry S. White and Andreas Bund. Ion current rectification at nanopores in glass membranes. *Langmuir*, 24(5):2212–2218, mar 2008.

[208] Chenyu Wen, Shuangshuang Zeng, Shiyu Li, Zhen Zhang, and Shi-Li Zhang. On rectification of ionic current in nanopores. *Analytical Chemistry*, 91(22):14597–14604, oct 2019.

[209] Kazumichi Yokota, Makusu Tsutsui, and Masateru Taniguchi. Electrode-embedded nanopores for label-free single-molecule sequencing by electric currents. *RSC Adv.*, 4(31):15886–15899, 2014.

[210] Liang Xue, Paolo Cadinu, Binoy Paulose Nadappuram, Minkyung Kang, Ye Ma, Yuri Korchev, Aleksandar P. Ivanov, and Joshua B. Edel. Gated single-molecule transport in double-barreled nanopores. *ACS Applied Materials & Interfaces*, 10(44):38621–38629, oct 2018.

[211] Pascal Gehring, Jos M. Thijssen, and Herre S. J. van der Zant. Single-molecule quantum-transport phenomena in break junctions. *Nature Reviews Physics*, 1(6):381–396, may 2019.

[212] Mickael L. Perrin, Enrique Burzurí, and Herre S. J. van der Zant. Single-molecule transistors. *Chemical Society Reviews*, 44(4):902–919, 2015.

[213] Youngsang Kim, Wonho Jeong, Kyeongtae Kim, Woochul Lee, and Pramod Reddy. Electrostatic control of thermoelectricity in molecular junctions. *Nature Nanotechnology*, 9(11):881–885, oct 2014.

[214] F. O. Hadeed and C. Durkan. Controlled fabrication of 1–2nm nanogaps by electromigration in gold and gold-palladium nanowires. *Applied Physics Letters*, 91(12):123120, sep 2007.

[215] Wonho Jeong, Kyeongtae Kim, Youngsang Kim, Woochul Lee, and Pramod Reddy. Characterization of nanoscale temperature fields during electromigration of nanowires. *Scientific Reports*, 4(1), may 2014.

[216] Hubert B. Heersche, Günther Lientschnig, Kevin O'Neill, Herre S. J. van der Zant, and Henny W. Zandbergen. In situ imaging of electromigration-induced nanogap formation by transmission electron microscopy. *Applied Physics Letters*, 91(7):072107, aug 2007.

[217] Yuhui He, Makusu Tsutsui, Chun Fan, Masateru Taniguchi, and Tomoji Kawai. Controlling DNA translocation through gate modulation of nanopore wall surface charges. *ACS Nano*, 5(7):5509–5518, jun 2011.

[218] Yuhui He, Makusu Tsutsui, Chun Fan, Masateru Taniguchi, and Tomoji Kawai. Gate manipulation of DNA capture into nanopores. *ACS Nano*, 5(10):8391–8397, sep 2011.

[219] Makusu Tsutsui, Sou Ryuzaki, Kazumichi Yokota, Yuhui He, Takashi Washio, Kaoru Tamada, and Tomoji Kawai. Field effect control of translocation dynamics in surround-gate nanopores. *Communications Materials*, 2(1), mar 2021.

[220] Kee-Hyun Paik, Yang Liu, Vincent Tabard-Cossa, Matthew J. Waugh, David E. Huber, J Provine, Roger T. Howe, Robert W. Dutton, and Ronald W. Davis. Control of DNA capture by nanofluidic transistors. *ACS Nano*, 6(8):6767–6775, jul 2012.

[221] Charalambos Evangeli, Edward McCann, Jacob L. Swett, Sumit Tewari, Xinya Bian, James O. Thomas, G. Andrew D. Briggs, Oleg V. Kolosov, and Jan A. Mol. Experimental evidence of disorder enhanced electron-phonon scattering in graphene devices. *Carbon*, 178:632–639, jun 2021.

[222] Anil Koklu, Assaad El Helou, Peter E. Raad, and Ali Beskok. Characterization of temperature rise in alternating current electrothermal flow using thermoreflectance method. *Analytical Chemistry*, 91(19):12492–12500, sep 2019.

[223] Golak Kunti, Jayabrata Dhar, Anandaroop Bhattacharya, and Suman Chakraborty. Joule heating-induced particle manipulation on a microfluidic chip. *Biomicrofluidics*, 13(1):014113, jan 2019.

[224] Tae Joon Kwak, Imtiaz Hossen, Rashid Bashir, Woo-Jin Chang, and Chung Hoon Lee. Localized dielectric loss heating in dielectrophoresis devices. *Scientific Reports*, 9(1), dec 2019.

[225] Jasper P. Fried, Xinya Bian, Jacob L. Swett, Ivan I. Kravchenko, G. Andrew D. Briggs, and Jan A. Mol. Large amplitude charge noise and random telegraph fluctuations in room-temperature graphene single-electron transistors. *Nanoscale*, 12(2):871–876, 2020.

[226] Henk W. Ch. Postma. Rapid sequencing of individual DNA molecules in graphene nanogaps. *Nano Letters*, 10(2):420–425, feb 2010.

[227] Y. Choi, I. S. Moody, P. C. Sims, S. R. Hunt, B. L. Corso, I. Perez, G. A. Weiss, and P. G. Collins. Single-molecule lysozyme dynamics monitored by an electronic circuit. *Science*, 335(6066):319–324, jan 2012.

[228] Sebastian Sorgenfrei, Chien yang Chiu, Ruben L. Gonzalez, Young-Jun Yu, Philip Kim, Colin Nuckolls, and Kenneth L. Shepard. Label-free single-molecule detection of DNA-hybridization kinetics with a carbon nanotube field-effect transistor. *Nature Nanotechnology*, 6(2):126–132, jan 2011.

[229] Tivoli J. Olsen, Yongki Choi, Patrick C. Sims, O. Tolga Gul, Brad L. Corso, Chengjun Dong, William A. Brown, Philip G. Collins, and Gregory A. Weiss. Electronic measurements of single-molecule processing by DNA polymerase i (klenow fragment). *Journal of the American Chemical Society*, 135(21):7855–7860, may 2013.

[230] Alexander A. Balandin. Low-frequency 1/f noise in graphene devices. *Nature Nanotechnology*, 8(8):549–555, aug 2013.

[231] Xiang-Xiang Song, Hai-Ou Li, Jie You, Tian-Yi Han, Gang Cao, Tao Tu, Ming Xiao, Guang-Can Guo, Hong-Wen Jiang, and Guo-Ping Guo. Suspending effect on low-frequency charge noise in graphene quantum dot. *Scientific Reports*, 5(1), jan 2015.

[232] Paweł Puczkarski, Qingqing Wu, Hatef Sadeghi, Songjun Hou, Amin Karimi, Yuewen Sheng, Jamie H. Warner, Colin J. Lambert, G. Andrew D. Briggs, and Jan A. Mol. Low-frequency noise in graphene tunnel junctions. *ACS Nano*, 12(9):9451–9460, aug 2018.

[233] John G. Simmons. Generalized formula for the electric tunnel effect between similar electrodes separated by a thin insulating film. *Journal of Applied Physics*, 34(6):1793–1803, jun 1963.

[234] Jakub K. Sowa, Jan A. Mol, G. Andrew D. Briggs, and Erik M. Gauger. Beyond marcus theory and the landauer-büttiker approach in molecular junctions: A unified framework. *The Journal of Chemical Physics*, 149(15):154112, oct 2018.

[235] R. A. Marcus. On the theory of oxidation-reduction reactions involving electron transfer. i. *The Journal of Chemical Physics*, 24(5):966–978, may 1956.

[236] Ferry Prins, Amelia Barreiro, Justus W. Ruitenberg, Johannes S. Seldenthuis, Núria Aliaga-Alcalde, Lieven M. K. Vandersypen, and Herre S. J. van der Zant. Room-temperature gating of molecular junctions using few-layer graphene nanogap electrodes. *Nano Letters*, 11(11):4607–4611, nov 2011.

[237] C. S. Lau, J. A. Mol, J. H. Warner, and G. A. D. Briggs. Nanoscale control of graphene electrodes. *Phys. Chem. Chem. Phys.*, 16(38):20398–20401, 2014.

[238] Maria El Abbassi, László Pósa, Péter Makk, Cornelia Nef, Kishan Thodkar, András Halbritter, and Michel Calame. From electroburning to sublimation: substrate and environmental effects in the electrical breakdown process of monolayer graphene. *Nanoscale*, 9(44):17312–17317, 2017.

[239] Amelia Barreiro, Herre S. J. van der Zant, and Lieven M. K. Vandersypen. Quantum dots at room temperature carved out from few-layer graphene. *Nano Letters*, 12(12):6096–6100, nov 2012.

[240] Bart Limburg, James O. Thomas, Gregory Holloway, Hatef Sadeghi, Sara Sangtarash, Ian Cheng-Yi Hou, Jonathan Cremers, Akimitsu Narita, Klaus Müllen, Colin J. Lambert, G. Andrew D. Briggs, Jan A. Mol, and Harry L. Anderson. Anchor groups for graphene-porphyrin single-molecule transistors. *Advanced Functional Materials*, 28(45):1803629, sep 2018.

[241] Yu-Ming Lin and Phaedon Avouris. Strong suppression of electrical noise in bilayer graphene nanodevices. *Nano Letters*, 8(8):2119–2125, aug 2008.

[242] S. W. Jung, T. Fujisawa, Y. Hirayama, and Y. H. Jeong. Background charge fluctuation in a GaAs quantum dot device. *Applied Physics Letters*, 85(5):768–770, aug 2004.

[243] Iddo Heller, Sohail Chatoor, Jaan Mannik, Marcel A. G. Zevenbergen, Jeroen B. Oostinga, Alberto F. Morpurgo, Cees Dekker, and Serge G. Lemay. Charge noise in graphene transistors. *Nano Letters*, 10(5):1563–1567, may 2010.

[244] Jaan Männik, Iddo Heller, Anne M. Janssens, Serge G. Lemay, and Cees Dekker. Charge noise in liquid-gated single-wall carbon nanotube transistors. *Nano Letters*, 8(2):685–688, feb 2008.

[245] Dnaiel Zwillinger and Stephen Kokoska. *CRC Standard Probability and Statistics tables and Formulae*. Chapman and Hall, 2000.

[246] J. Tersoff. Low-frequency noise in nanoscale ballistic transistors. *Nano Letters*, 7(1):194–198, jan 2007.

[247] Hyungwoo Lee, Duckhyung Cho, Shashank Shekhar, Jeongsu Kim, Jaesung Park, Byung Hee Hong, and Seunghun Hong. Nanoscale direct mapping of noise source activities on graphene domains. *ACS Nano*, 10(11):10135–10142, nov 2016.

[248] Sebastian Sorgenfrei, Chien yang Chiu, Matthew Johnston, Colin Nuckolls, and Kenneth L. Shepard. Debye screening in single-molecule carbon nanotube field-effect sensors. *Nano Letters*, 11(9):3739–3743, sep 2011.

[249] Kaitlin M. Pugliese, O. Tolga Gul, Yongki Choi, Tivoli J. Olsen, Patrick C. Sims, Philip G. Collins, and Gregory A. Weiss. Processive incorporation of deoxynucleoside triphosphate analogs by single-molecule DNA polymerase i (klenow fragment) nanocircuits. *Journal of the American Chemical Society*, 137(30):9587–9594, jul 2015.

[250] Robert J. Chen, Yuegang Zhang, Dunwei Wang, and Hongjie Dai. Noncovalent sidewall functionalization of single-walled carbon nanotubes for protein immobilization. *Journal of the American Chemical Society*, 123(16):3838–3839, apr 2001.

[251] Jinglei Ping, Ramya Vishnubhotla, Amey Vrudhula, and A. T. Charlie Johnson. Scalable production of high-sensitivity, label-free DNA biosensors based on back-gated graphene field effect transistors. *ACS Nano*, 10(9):8700–8704, sep 2016.

[252] Yang Cao, Shaohua Dong, Song Liu, Li He, Lin Gan, Xiaoming Yu, Michael L. Steigerwald, Xiaosong Wu, Zhongfan Liu, and Xuefeng Guo. Building high-throughput molecular junctions using indented graphene point contacts. *Angewandte Chemie*, 124(49):12394–12398, nov 2012.

[253] Zihao Liu, Xingxing Li, Hiroshi Masai, Xinyi Huang, Susumu Tsuda, Jun Terao, Jinlong Yang, and Xuefeng Guo. A single-molecule electrical approach for amino acid detection and chirality recognition. *Science Advances*, 7(10):eabe4365, mar 2021.

[254] Ji Won Suk, Alexander Kitt, Carl W. Magnuson, Yufeng Hao, Samir Ahmed, Jinho An, Anna K. Swan, Bennett B. Goldberg, and Rodney S. Ruoff. Transfer of CVD-grown monolayer graphene onto arbitrary substrates. *ACS Nano*, 5(9):6916–6924, sep 2011.

Appendix A

Device Fabrication

Here I will give a detailed description of fabrication procedure used to create the devices described in this thesis. Substrates were prepared by Kevin Lester and Daryl Briggs with wet thermal oxidation used to create the SiO_2 layer and Low Pressure Chemical Vapour Deposition used to fabricate the SiN_x layer.

A.1 Suspended SiN_x Membranes

This is the fabrication procedure used to create suspended SiN_x membranes (with no on chip electrodes) as discussed in Chapters 2 and 3. Fabrication of these devices was performed by Jacob Swett or James Yates. All of the below fabrication steps were performed on the wafer scale.

1. **Spin coat photoresist:** Spin coat MCC Primer 80/20 at 3000 rpm followed by Shipley 18-18 at 3000 rpm. Bake the wafer at 115°C for 60 sec.

2. **Photolithography and development:** Expose to UV light using a mask aligner with a dose of 60 mJ/cm^2. Develop in CD-26 for 60 s followed by DI water rinse.

3. **RIE of SiN_x/SiO_2 Hard Mask:** Etch SiN_x and SiO_2 layers using reactive ion etching with gas flows of C_4F_8 at 45 sccm and O_2 at 2 sccm.

4. **Resist Strip:** Leave wafer in acetone for 15 minutes to remove the resist.

5. **Frontside Protect with Resist:** Spin MCC Primer 80/20 on the wafer at 3000 rpm followed by PMMA 950k A5 at 2000 rpm. Bake at 190° for 10 minutes.

6. **Wafer Etch:** Load wafer into a single sided wafer holder sealed with o-rings so that only the back side of the wafer is exposed to solution. Place wafer in 30% KOH at 80°C for ∼8 hours. Wash wafer in DI wafer and dry with N_2.

A.2 Electrodes on Suspended SiN_x Membranes

This is one of the fabrication procedures used to fabricate electrodes on suspended SiN_x membranes. These steps can be performed either before or after etching of the substrate to create suspended SiN_x membranes (i.e. step 5 in the procedure above). The advantage of performing this step prior to etching the substrate is that it reduces handling of the suspended SiN_x which result in damage to the membrane. However, it means that the electrode configuration of the entire wafer must be written at this stage which can be wasteful given the incremental progress of research. Devices presented in Chapter 5 were fabricated after substrate etching and electrode fabrication was performed by myself. Devices presented in Chapters 3 and 4 were fabricated prior to substrate etching and electrode fabrication was performed by Jacob Swett.

1. **Spin coat photoresist primer:** Spin coat Ti primer onto chip at 3000 rpm and bake at 120°C for 2 minutes.

2. **Spin coat photoresist:** Spin coat ma-N 1420 at 3000 rpm and bake at 100°C for 2 minutes.

3. **Photolithography and development:** Expose to UV light using a mask aligner with a dose of 550 mJ/cm^2. Develop in ma-D 533/S for 80 seconds followed by DI water.

4. **Thermal Evaporation:** Evaporate 5 nm Cr followed by 75 nm Au.

5. **Liftoff:** Leave in warm (50°C) acetone for until liftoff is complete (approximately 1 hour).

6. **Spin coat e-beam resist primer:** Spin coat PMGI SF6 at 4000 rpm and bake at 190°C.

7. **Spin coat e-beam resist:** Spin coat 950k PMMA A8 at 6000 rpm for 60 s. Bake on hotplate at 175°C for 60 s.

8. **Spin coat e-spacer:** Spin coat e-spacer 300Z onto device at 15000 rpm. Bake on hotplate at 80°C for 60 s.

9. **Electron beam lithography:** Expose using electron beam lithography with a dose of 950 μC/cm^2. Note that a higher dose is need for patterning structures on suspended membranes since there is minimal electron backscatter from the substrate.

10. **Develop:** Place chip in DI water for 60 s to remove e-spacer and dry with N_2. Place chip in MIBK:IPA 1:3 for 4 minutes followed by an IPA rinse and dry with N_2. Place chip in MF 319 for 7-15 s (timing is important as development of PGMI is very quick) followed by DI water rinse and dry with N_2.

11. **Thermal evaporation:** Evaporate 5 nm Cr followed by 30 nm Au.

12. **Liftoff:** Place in Microposit 1165 at 50°C until liftoff is complete (approximately 4 hours).

A.3 Graphene Nanodevices

This is the fabrication procedure for devices discussed in Chapter 6. All of the fabrication steps were preformed by myself. Steps 1-4 were performed on the wafer scale. Steps 5-12 were performed on the chip scale.

1. **Spin coat photoresist:** Spin MCC primer onto the wafer at 3000 rpm followed by JSR NFR-016D2 at 3000 rpm. The wafer is then baked at 90°C for 90 seconds.

2. **Photolithography and development:** Expose using a mask aligner with a dose of 120 mJ/cm^2. Base at 90°C for 90 s post exposure. Develop in CD-26 for 60s followed by DI water rinse.

3. **Electron beam evaporation:** Evaporate 5 nm of Cr followed by 95 nm of Au.

4. **Liftoff:** Leave in acetone overnight or until liftoff is complete. Sonicate briefly if necessary to aid liftoff.

5. **Graphene transfer:** Etch the copper from CVD grown graphene (purchased from Graphenea) in 0.2 M ammonium persulfate. Using a glass slide, transfer the graphene to a fresh DI water beaker 3 times and then transfer to the substrate. Leave to dry, place on hotplate at 180°C for 1 hour and then place in warm (50°C) acetone for 1 hour to remove the PMMA [254].

6. **Spin coat e-beam resist:** Spin AR-N 7500 on the chip at 4000 rpm and bake at 85°C for 1 minute.

7. **Electron beam lithography and development:** Expose using electron beam lithography with a dose of 300μC/cm^2. Develop in CD 26 for 1 minute followed by DI water rinse.

8. **Graphene patterning:** Etch graphene using oxygen plasma treatment with a power of 100 W and an oxygen flow rate of 25 sccm for 2 minutes.

9. **Resist removal:** Remove resist covering graphene in mr-REM 660 at 50 C for two hours.

10. **Spin coat passivation layer:** Spin coat PMMA 495 at a speed of 4000 rpm. Bake on a hotplate at 180°C for 10 minues.

11. **Electron beam lithography and development:** Expose using electron beam lithography with a dose of 700 μC/cm^2. Develop in 1:3 MIBK:IPA for 60 s followed by IPA rinse.

12. **Electroburn:** Perform feedback controlled electroburing of graphene nanoconstriction to create graphene gaps and graphene quantum dots.

Appendix B

Fluidic Cell Designs

Below are the technical drawings for the on-chip biasing fludiic cell and the 'H-bar' holder for wirebonding as described in Chapter 4.2.

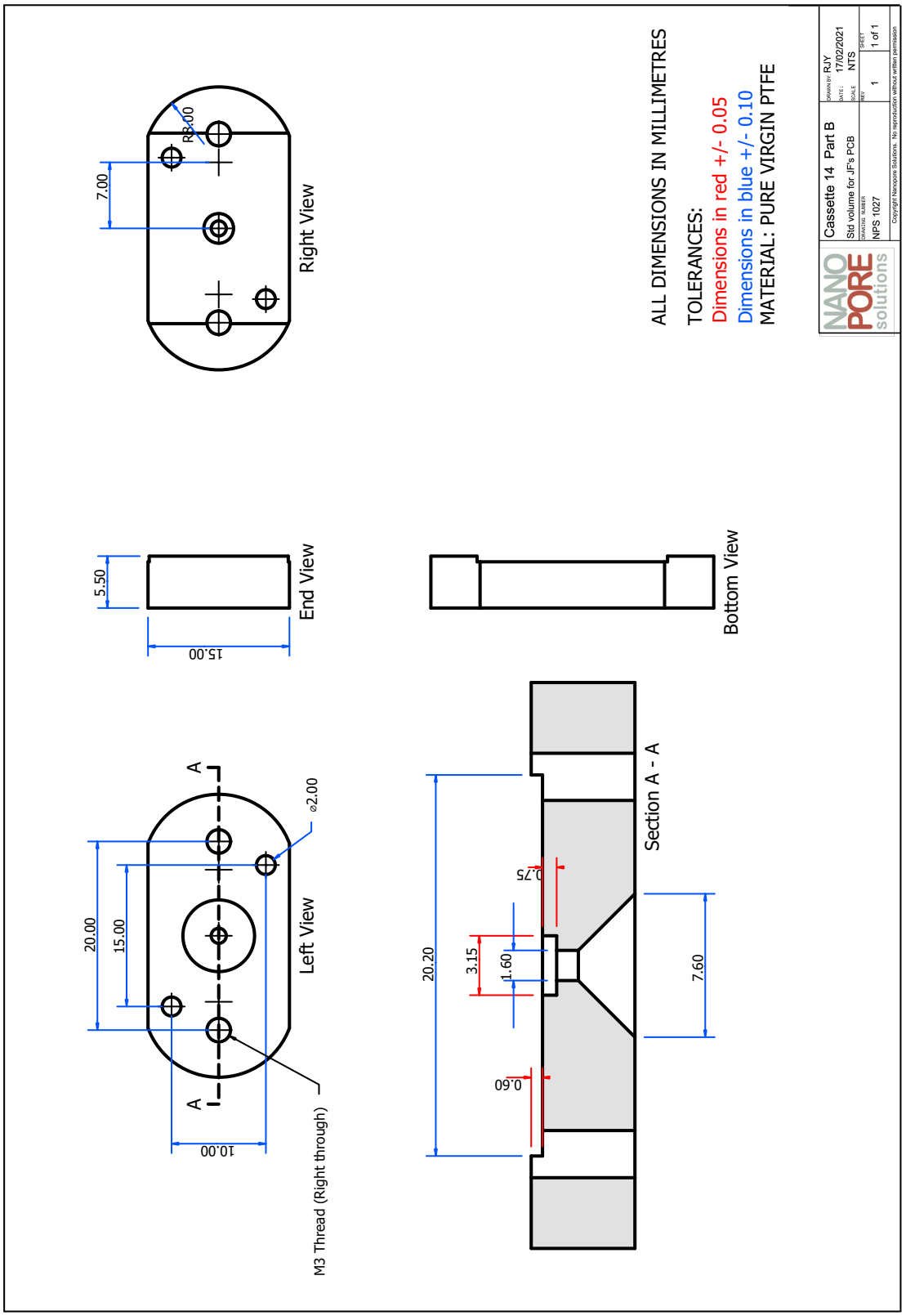


FIGURE B.1: Technical drawing of the bottom half of the on-chip biasing fluidic cell cassette.

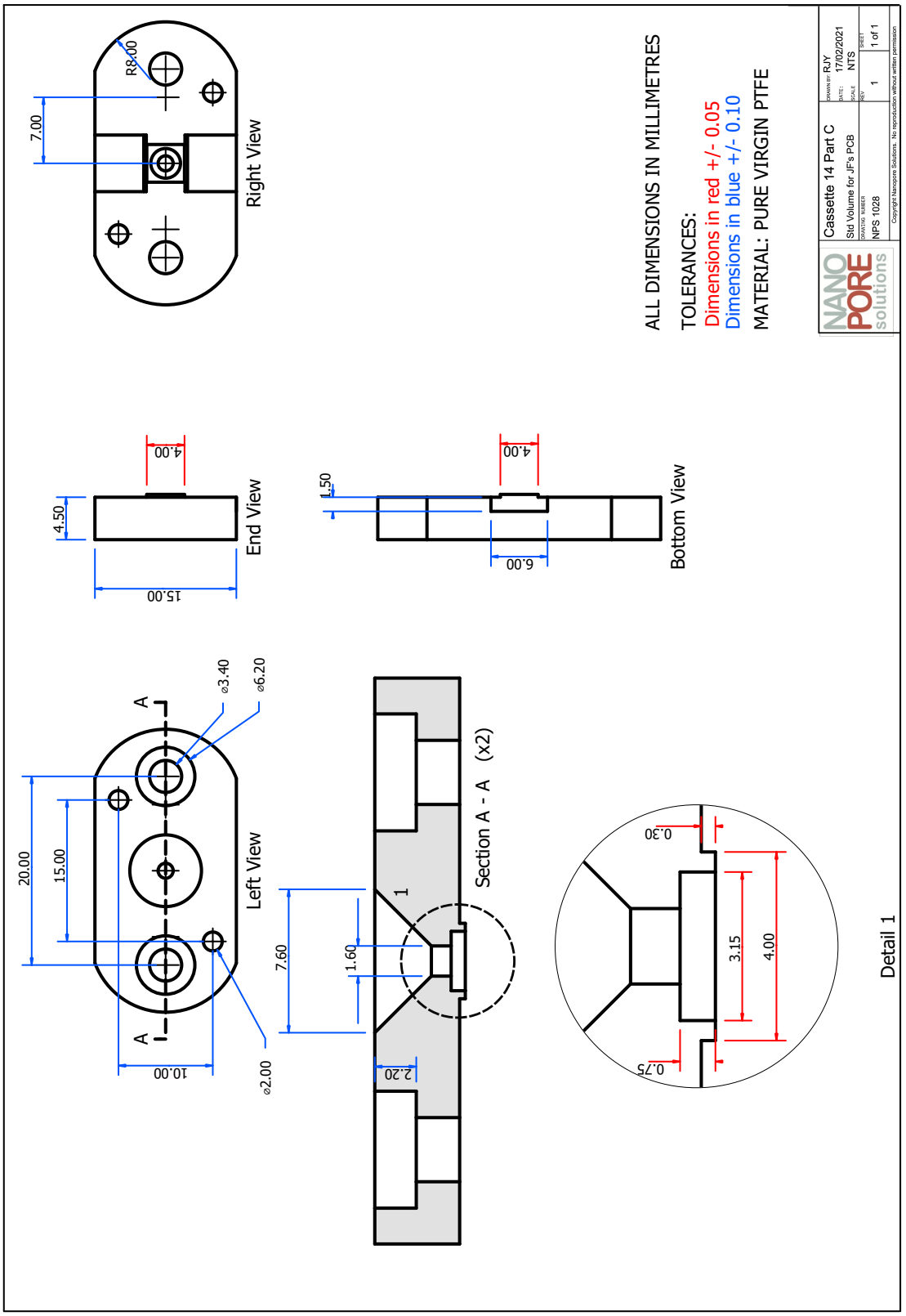


FIGURE B.2: Technical drawing of the top half of the on-chip biasing fluidic cell cassette.

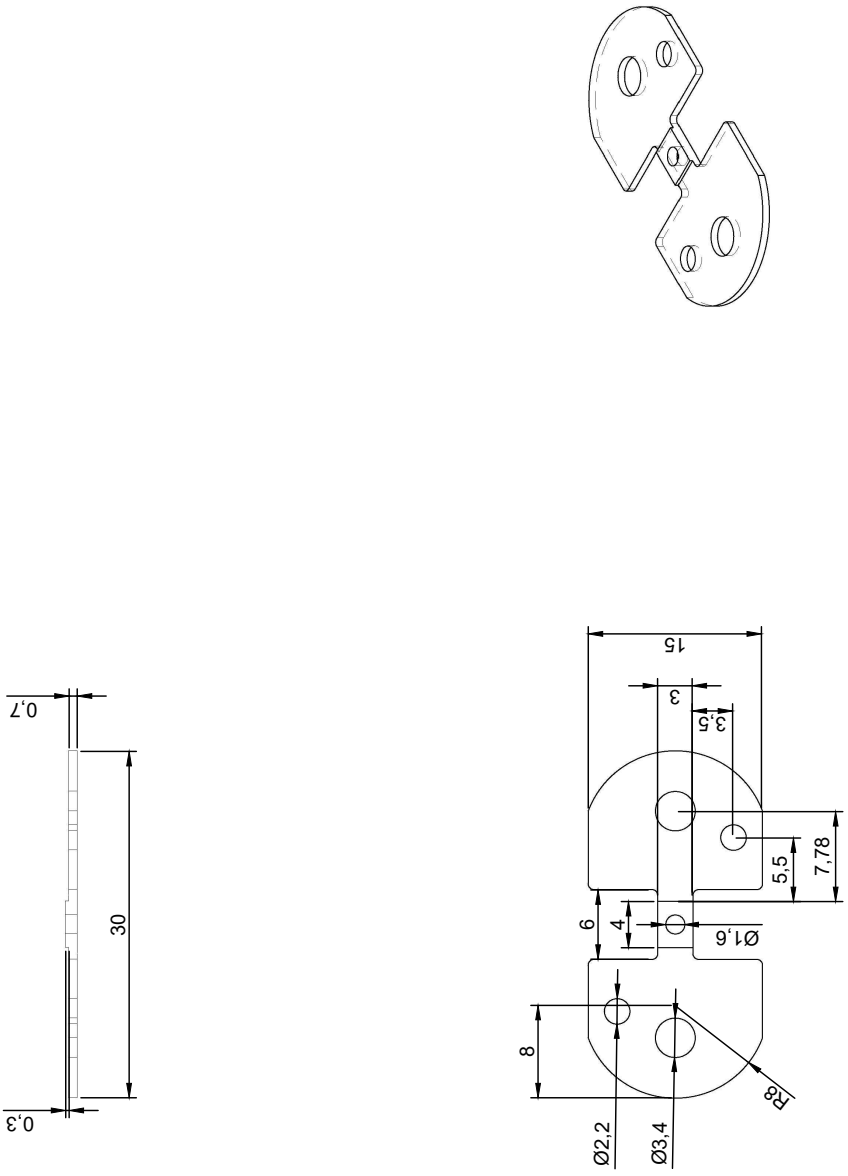


FIGURE B.3: Technical drawing of the 3D printed wire-bonding jig.

Appendix C

Device Discharge

One challenging aspect of working with the metal nanoconstrictions described in Chapter 5 it that electronic discharge can often damage the devices. This can occur before wirebonding the device or during experimentation when connecting measurement cables to the PCB. Figure C.1 shows several examples of discharge in metal nanoconstrictions. Interestingly, in some cases a pore in the SiN_x membrane is also formed in the region of discharge.

Device discharge when connecting measurement cables during experimentation can be overcome by using the fluidic cell described in Sec. 4.2. This fluidic cell incorporates

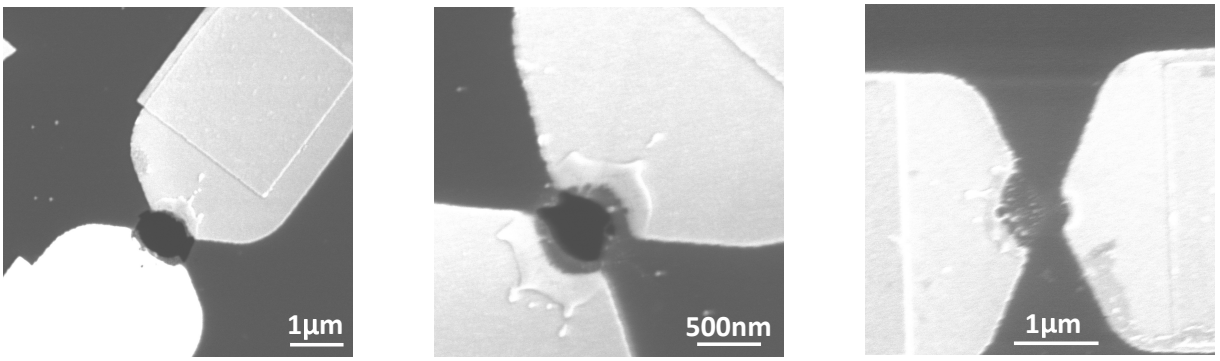


FIGURE C.1: Scanning electron micrographs of electric discharge in metal nanoconstriction devices. In the left and middle micrographs a pore is formed in the SiN_x membrane in the region of discharge.

switches on the PCB meaning that cables do not need to be changed to measure a different device. Moreover, keeping all of the switches grounded when initially connecting the measurement cables ensures that the source and drain electrodes are always kept at the same potential. Avoiding device discharge prior to wirebonding is more problematic. However, anecdotally I have found that wrapping the container housing the devices in aluminium foil helps to avoid static buildup when handing the container thus reducing device discharge.

Appendix D

The Simmons Model

For electron tunnelling through a rectangular barrier at intermediate applied voltages the resulting current density (J) can be calculated via Eq D.1 (i.e. see Eq 26 in [233]):

$$J = \frac{e}{2\pi h s^2}\left\{\left(\phi - \frac{eV}{2}\right)\exp\left[-\frac{4\pi s}{h}(2m)^{1/2}\left(\phi - \frac{eV}{2}\right)\right]\right. \\ \left. - \left(\phi + \frac{eV}{2}\right)\exp\left[-\frac{4\pi s}{h}(2m)^{1/2}\left(\phi + \frac{eV}{2}\right)\right]\right\} \tag{D.1}$$

where e is the charge of an electron, h is Plank's constant, s is the spacing between the electrodes, ϕ is the barrier height, V is the applied voltage, and m is the mass of an electron. The plot of tunnelling current shown in Fig. 6.1(a)(iii) is calculated with s=2 nm, ϕ=1eV, and a tunneling area of 87 nm^2.

Appendix E

Rate Equation Model for Electron Transport

A rate equation model can be used to determine the current through a quantum dot as discussed in Chapter 6. The rate equation model takes the following form:

$$I_{\text{mar}} = \frac{e}{\hbar} \frac{\gamma_S \bar{\gamma_D} - \bar{\gamma_S} \gamma_D}{\gamma_S + \gamma_D + \bar{\gamma_S} + \bar{\gamma_D}} \tag{E.1}$$

where e is the electron charge, $\hbar$ is the reduced Plank's constant, $\gamma_{S/D}$ are the electron transfer rates from the source/drain electrodes to the quantum dot and $\bar{\gamma}_{S/D}$ are the electron transfer rates from the quantum dot to the source/drain electrodes.

The electron transfer rates at an electrode can be calculated by:

$$\gamma = (2 - \Omega) \int f(\epsilon) k(\epsilon) d\epsilon \tag{E.2a}$$

$$\bar{\gamma} = (1 + \Omega) \int (1 - f(\epsilon)) \bar{k}(\epsilon) d\epsilon \tag{E.2b}$$

Ω is a factor to account for the spin degeneracy of a molecular energy level and takes the value of 0 or 1 [**?**]. $f(\epsilon)$ is the Fermi-Dirac distribution of electrons in the electrodes

which can be calculated from $f(\epsilon) = (\exp[(\epsilon - V)/k_{\mathrm{B}}T] + 1)^{-1}$ with V the voltage applied to the electrode. $k(\epsilon)$ is the rate constant for electron transfer from the electrode to the quantum dot while $\bar{k}(\epsilon)$ is the rate constant from the quantum dot to the electrode.

The rate constants can be calculated by Marcus theory [235] (as done for the fits described in Chapter 6).

$$k(\epsilon) = \frac{1}{\pi}\Gamma\sqrt{\frac{\pi}{4\lambda k_B T}}\exp\left(-\frac{(\lambda + \epsilon - \mu)^2}{4\lambda k_B T}\right) \tag{E.3}$$

$$\bar{k}(\epsilon) = \frac{1}{\pi}\Gamma\sqrt{\frac{\pi}{4\lambda k_B T}}\exp\left(-\frac{(\lambda - \epsilon - \mu)^2}{4\lambda k_B T}\right) \tag{E.4}$$

Γ is the electronic coupling between the electrode and the quantum dot, λ is the reorganization energy, k_B is Boltzmann's constant, T is the temperature, ϵ is the electron energy and μ is the chemical potential of quantum dot.

The chemical potential of the quantum dot is calculated from the capacitances to the source (C_S), drain (C_D) and gate (C_G) electrodes [**?**].

$$\mu = c - A(C_S V_S + C_D V_D + C_G V_G) \tag{E.5}$$

Where the c is an offset determined by the ground state and charging energy of the quantum dot and A is a constant determined by the charging energy of the quantum dot.

Fits for the experimental data shown in the main body of this work were calculated using these equations with λ, Γ_S, Γ_D, C_S, C_D, C_G, A and c the fitting parameters. Figure 6.1(b) the current as calcualted via the equations above was done with the parameters λ=0.1 eV, Γ_S=0.001, Γ_D=0.001, C_S=0.1 F, C_D=0.1 F, C_G=1 F, c=0 J, A=1 eV/C.